University of Wisconsin Milwaukee
UWM Digital Commons

Theses and Dissertations

December 2022

Using Anisotropy of Magnetic Susceptibility (AMS) to Identify a Tectonic Lineation in the Pulo Do Lobo Formation in the Southern Iberian Shear Zone Near Aracena, Spain

Devin Levang
University of Wisconsin-Milwaukee

Follow this and additional works at: https://dc.uwm.edu/etd

 Part of the Geology Commons, and the Geophysics and Seismology Commons

Recommended Citation

Levang, Devin, "Using Anisotropy of Magnetic Susceptibility (AMS) to Identify a Tectonic Lineation in the Pulo Do Lobo Formation in the Southern Iberian Shear Zone Near Aracena, Spain" (2022). *Theses and Dissertations*. 3108.
https://dc.uwm.edu/etd/3108

This Thesis is brought to you for free and open access by UWM Digital Commons. It has been accepted for inclusion in Theses and Dissertations by an authorized administrator of UWM Digital Commons. For more information, please contact scholarlycommunicationteam-group@uwm.edu.

USING ANISOTROPY OF MAGNETIC SUSCEPTIBILITY (AMS) TO IDENTIFY A TECTONIC LINEATION IN THE PULO DO LOBO FORMATION IN THE SOUTHERN IBERIAN SHEAR ZONE NEAR ARACENA, SPAIN

by

Devin Levang

A Thesis Submitted in

Partial Fulfillment of the

Requirements for the Degree of

Master of Science

in Geosciences

at

The University of Wisconsin – Milwaukee

December 2022

ABSTRACT

USING ANISOTROPY OF MAGNETIC SUSCEPTIBILITY (AMS) TO IDENTIFY A TECTONIC LINEATION IN THE PULO DO LOBO FORMATION IN THE SOUTHERN IBERIAN SHEAR ZONE NEAR ARACENA, SPAIN

by

Devin Levang

The University of Wisconsin – Milwaukee, 2022
Under the Supervision of Professor Dyanna Czeck

The Southern Iberian Shear Zone (SISZ) is a Variscan-aged suture representing the closure of a small ocean basin during the Carboniferous. The SISZ is bounded on either side by the well-studied, relatively homogeneous Beja-Acebuches Metabasites (BAM) and the complex and heterogeneous accretionary metasedimentary rocks of the Pulo do Lobo (PdL). The SISZ underwent a combination of shortening and lateral shearing known as transpression. Despite a very well-developed tectonic foliation, kinematic interpretation in the PdL is made difficult by a lack of easily identifiable lineations. Anisotropy of magnetic susceptibility (AMS), a geophysical technique measuring the relative anisotropy of magnetic susceptibility axes of all minerals contained within a rock, has been used successfully to identify magnetic fabrics within deformed rocks. Previous research has established the coaxiality of AMS fabric with a rock's tectonic fabric in many cases.

PdL samples showed low values of magnetic susceptibility (Kmean = 119 SI^{-6}) and distinctly paramagnetic hysteresis, indicating the magnetic fabric in the samples is likely formed by the alignment of iron-bearing phyllosilicates, mostly biotite. AMS data for the PdL showed a

strong magnetic foliation matching the orientation of that measured in the field. A number of magnetic lineations were identified along the foliation plane. Roughly half were grouped in a down-dip orientation, consistent with thrust-dominant kinematics. A population of shallow lineation orientations to the geographic SE possibly result from left-lateral shearing experienced within the PdL. Alternatively, variance in lineation orientation could be controlled by variations in the extrusion direction of the pure shear component. Variation in the ratio between the simple and pure shear components across the disparate lithologies of the PdL could also account for the measured oblique lineation orientations. Despite the complexity of their formation, orientation of magnetic lineations calculated using AMS closely matched field lineations, opening possibilities for further use of AMS in the SISZ.

AMS parameters were largely controlled by lithology and did not correlate with strain magnitude. The shape of the AMS ellipsoid was oblate to strongly oblate in all samples, consistent with flattening expected in tectonic transpression. Fabric intensity measured in degree of anisotropy ranged from nearly isotropic to moderately anisotropic, with the most anisotropic samples in the quartzite where the paramagnetic fraction of the fabric reached up to 50%. This value is substantially higher than in the phyllites which contained numerous ferromagnetic components that likely decreased the overall degree of anisotropy. A region within 50 meters from the SZ was coincidental with a drop in mean susceptibility. Geochemical data from previous work that studied the same section suggest the influence of syntectonic hydrothermal fluid flow from the MORB-derived BAM side of the SISZ. This is evidenced by the higher bulk susceptibilities closer to the SISZ resulting from the creation of secondary ferromagnetic minerals and Fe-enriched biotite in the proposed hydrothermally affected zone.

TABLE OF CONTENTS

LIST OF FIGURES

ACKNOWLEDGEMENTS

First and foremost, I would like to thank my advisor Dr. Dyanna Czeck for her total support and guidance throughout my entire time at UWM. Even when I was halfway across the country and struggling with medical issues Dr. Czeck displayed immense patience and understanding. On top of being my advisor, Dyanna has given me numerous opportunities to find extra work and enrich myself both academically and otherwise. Dr. Czeck's NSF grant supported my graduate education and research, and I will be forever grateful for the chance to continue my academic career when everything in my life (and the world) was turned upside-down two years ago. I would also like to thank the UWM Geosciences Department for being so welcoming and knowledgeable, and along with the Wisconsin Geologic Society also providing funding for my research.

Thank you Dr. Manuel Díaz-Azpiroz and Carlos Fernández for collecting samples in Spain when travelling to the field site on my own was out of the question. Thank you especially to Dr. Díaz-Azpiroz and Dr. Julie Bowles for being on my committee. I greatly respect the breadth of knowledge you each bring to the table, and I am so grateful you had the time and inclination to help guide my research in several ways. I want to further thank Dr. Dario Bilardello at the Institute for Rock Magnetism at the University of Minnesota for teaching me how to use the equipment at the lab and earnestly answering all my overly simple questions.

I would like to thank my family for all their encouragement, even when their eyes were glazing over listening to me talk about rocks. Finally, I want to thank my amazing partner, Erum. Thank you so much for taking this leap across the country with me. You've always been my biggest supporter and I cannot wait to see what the future holds for the two of us together.

1) Introduction

Within the field of structural geology, one of the most powerful tools for unraveling the deformational history of a rock is kinematic modelling. All of the rocks studied by geologists, including those actively undergoing deformation, are snapshots of finished products, a look at how the outcrop looks at that moment. It is up to scientists to work backwards and attempt to qualify and quantify the factors at work in a rock's deformation. To that end, kinematics, the study of motion within a rock, is essential in both understanding the mechanics at work as well as identifying a possible deformation path within an outcrop. Kinematic modelling at the highest level is a robust mathematical exercise, using field data along with laboratory measurements to iterate orientation parameters which can then be used describe and quantify strain. An important variable in kinematics is lineation orientation. Tectonic stretching lineations highlight the direction of maximum extension, and therefore minimum contraction, within a rock. Unfortunately, identifying lineations in the field is not always a trivial exercise. Unsuitable composition or deformation either too weak or too complex can obscure lineation, removing an important piece of the kinematic puzzle. In these cases, the magnetic fabric of the rock may help reveal the lineation, and aid in understanding deformational kinematics.

Anisotropy of magnetic susceptibility (AMS) is a useful tool for identifying fabrics in deformed metasedimentary rocks (Borradaile & Henry, 1997; Jackson & Tauxe, 1991; Parés, 2015; Weil & Yonkee, 2009). In many cases, the susceptibility axes derived from AMS measurements can be used as acceptable proxies for the tectonic fabric which is typically used to interpret the orientation of the strain ellipsoid (Parés & Van der Pluijm, 2002). This research applies AMS to Pulo do Lobo (PdL) metasedimentary rocks deformed by the Southern Iberian

Shear Zone (SISZ) in order to determine the strain ellipsoid orientation and constrain kinematic models. The SISZ provides a type example of a transpressional shear zone at a major tectonic boundary and can thus be used to further our understanding of shear zone kinematics and strain partitioning. In contrast to the Beja-Acebuches Metabasites (BAM) on the northeast side of the SISZ which display consistent and well-developed tectonic fabrics, the rocks of the PdL on the southwest side of the SZ present an excellent opportunity to use AMS as a strain analogue. Despite the well-established and previously observed metamorphic foliation, the mineralogy present in the PdL does not generally allow for easy identification of a tectonic lineation.

Tectonic lineations are critical data required to test kinematic models (e.g. Fernández et al., 2013), so approximating their orientations from AMS fabrics is extremely useful. Previous studies indicate that strain and kinematics are likely highly variable across the SISZ. For example, ample structural analyses within the Acebuches Metabasites on the north side of the shear zone indicates that the SISZ motion was dominated by left lateral transpression (Díaz-Azpiroz & Fernández, 2005; Fernández et al., 2013), whereas microstructural kinematic indicators and steeply dipping lineations within the PdL on the south side of the SISZ suggest that kinematics may have been dominated by thrusting (Carman, 2020). More detailed fieldwork suggests that lineation orientations within the PdL are even more complex, suggesting meter scale changes in kinematics (Czeck et al., 2022). Unravelling detailed kinematic partitioning can serve as an example of how rheological boundaries or pathways of fluid-assisted rheological weakening are exploited to accommodate different components of plate convergence during orogenesis.

In addition, it may be possible to use magnitude of susceptibility, degree of anisotropy (e.g. Ferré et al., 2003), or AMS shape parameter (e.g. Parés and van der Pluijm, 2003) as a stand-in for strain magnitude for the purpose of making relative comparisons. However, these extrapolations must be used with caution and do not hold true for all situations as the relationships depend on lithology, magnetic mineralogy, and potentially other factors. If use of one of these relationships is warranted in this case, it will be possible to assess the relationship between strain and many different features of the shear zone including distance from the shear zone, lithology, and fluid pathways.

2) Geologic Background

2.1) <u>Zones within the Iberian Massif</u>

The Iberian Massif (Figure 1) is a collection of pre-Permian continental crust divided into six lithologically and tectonically distinct zones. The Iberian Massif was assembled beginning with magmatic arc crust creation and accretion during the Neoproterozoic along the margin of the supercontinent Gondwana, an event known as the Cadomian orogeny (Quesada, 2006). A subsequent Cambrian-aged rifting event resulted in the opening of the Rheic Ocean and a prolonged period of passive margin deposition during the Ordovician and Devonian Periods. Formation of the massif concluded with the closure of the Rheic Ocean and the assembly of Pangea ending with the Variscan-Alleghenian-Ouachita orogenies during the Carboniferous (Figure 2; Quesada et al., 1994; Azor et al., 2008). The southwest Iberian Variscides were the result of the last of these orogenies, the Variscan; an oblique left-lateral collision of the Central Iberian Zone (CIZ), the Ossa-Morena Zone (OMZ), and the South Portuguese Zone (SPZ) (Pérez-Cáceres et al., 2020).

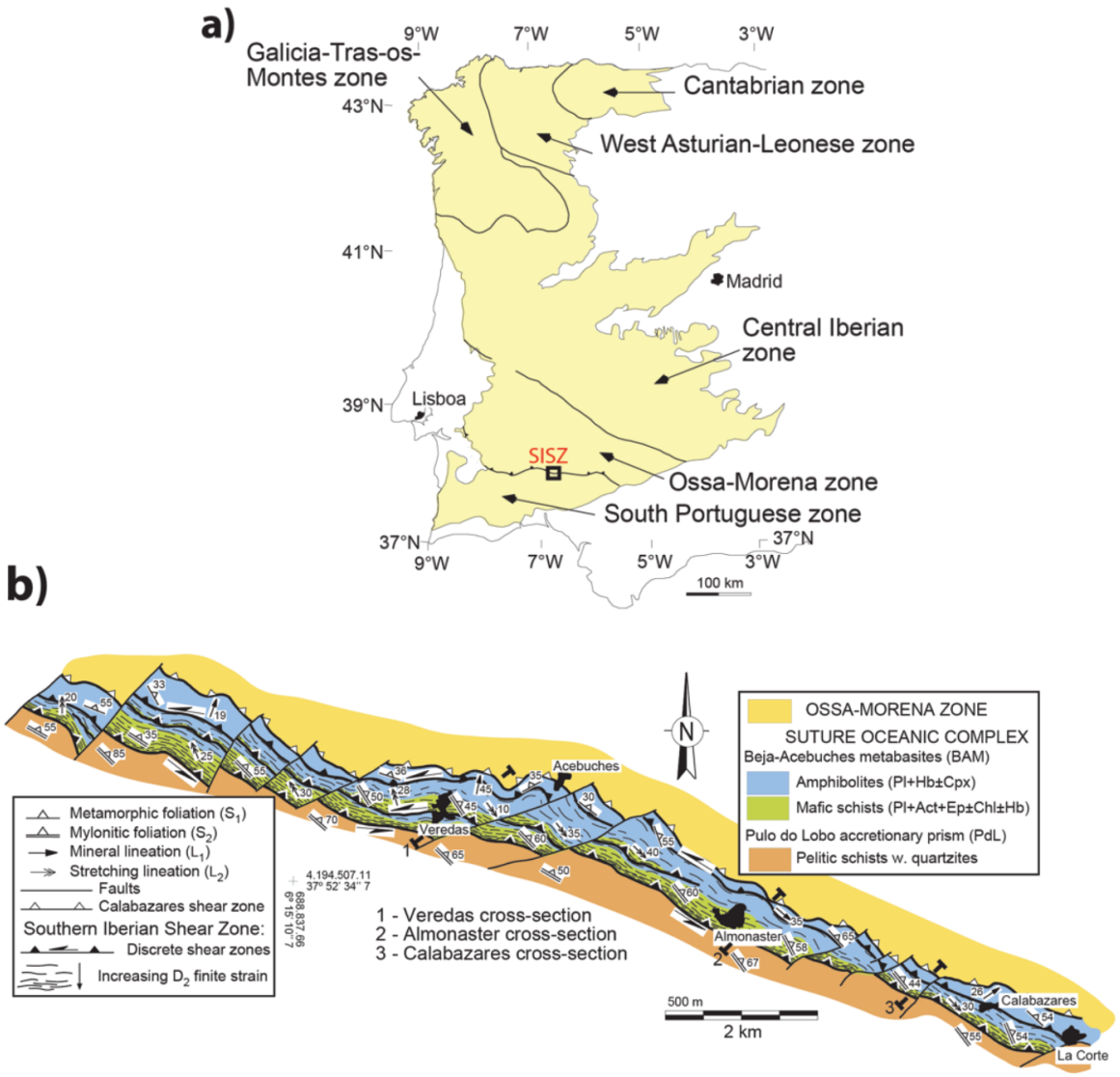

Figure 1: a) Zones within the Iberian Massif. The Southern Iberian Shear Zone (SISZ) formed at an oceanic suture between the Ossa-Morena and South Portuguese Zones; detailed study area indicated with box. b) Study area (boxed region from 1a) is the central portion of the SISZ with Beja-Acebuches Metabasites (BAM) indicated in blue/green and the Pulo do Lobo (PdL) shown in orange (Modified from Fernández et al., 2013)

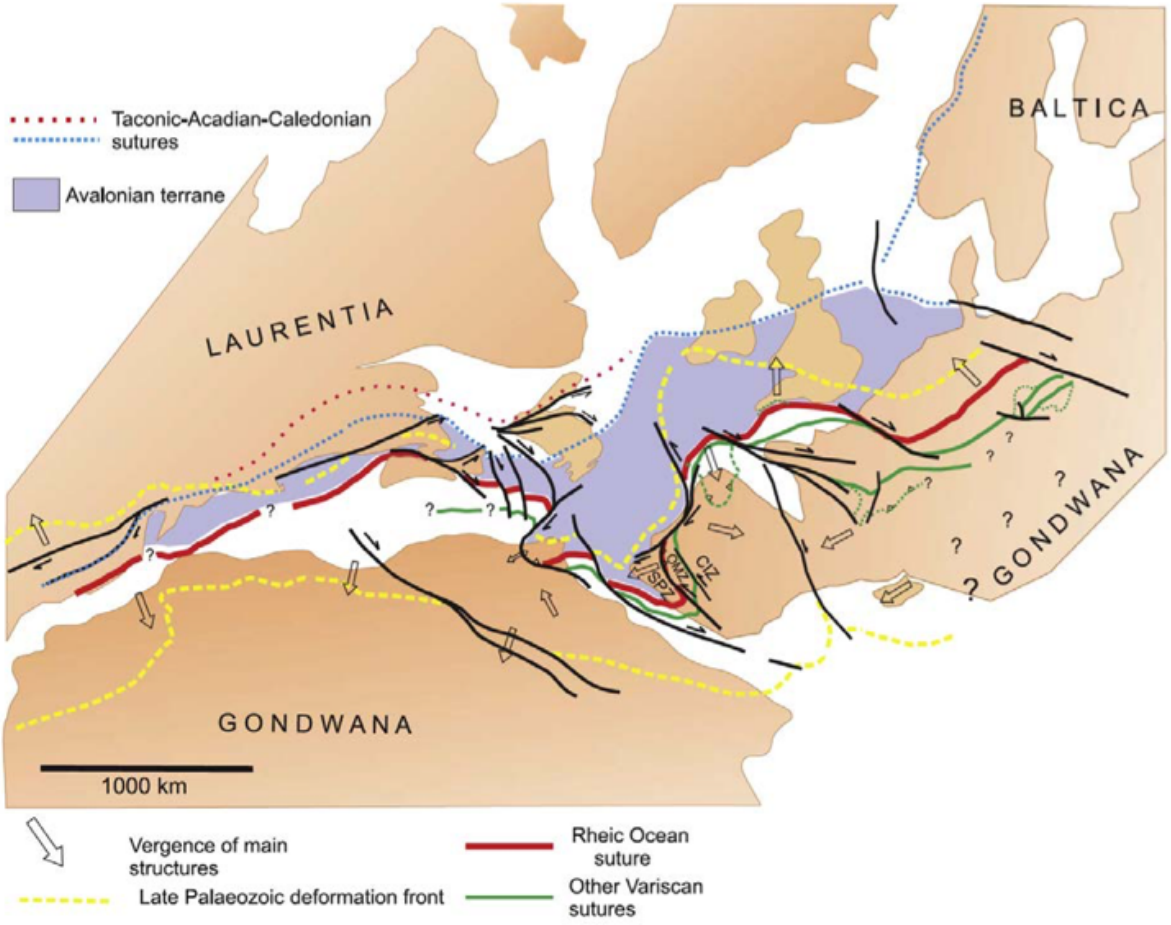

Figure 2: Tectonic reconstruction of Late Carboniferous collision of Laurentia and Gondwana along the Variscan-Alleghenian orogenic belt. The SISZ is located between the Ossa-Morena Zone (OMZ) and South Portuguese Zone (SPZ) within the Iberian Massif. From Azor et al., 2008.

The bulk of the OMZ consists of mostly Ediacaran to Carboniferous low-grade metasedimentary rocks derived from sediment deposited during the passive margin period of the Ordovician and Devonian that represent the continental margin of Armorica (Quesada, 2006). The OMZ also contains early Carboniferous-aged regions of high temperature, low pressure metamorphism deformed during the initial stages of the Variscan orogeny (Crespo-Blanc & Orozco, 1988). Between the OMZ and the neighboring South Portuguese Zone lies the amphibolite grade Beja-Acebuches Metabasites (BAM). The metabasites are a piece of remnant oceanic crust, as indicated by their MORB geochemical signature and represent part of a

dissected ophiolite sequence separating the two zones (Bard & Moine, 1979; Quesada et al., 1994; Castro et al., 1996; Díaz-Azpiroz and Fernández, 2005; Pérez-Cáceres et al., 2020).

To the south of the Beja-Acebuches Metabasites lies the Pulo do Lobo Formation (PdL). The origin of the PdL is a matter of some debate. One interpretation is that the PdL is an accretionary prism, a hypothesis supported by its position alongside the oceanically-derived BAM (e.g., Eden 1991; Silva et al. 1990; Onézime et al. 2003). Others interpret the PdL as the northernmost edge of the South Portuguese Zone (SPZ), most commonly interpreted as an extant piece of continental crust from the Avalonia microcontinent (Oliveira 1990; Braid et al., 2011; Pérez-Cáceres et al. 2015). Recent research has provided evidence of high temperature-low pressure features within the rocks of the PdL, features that indicate contact metamorphism between the BAM and the PdL, and thus support the hypothesis that the PdL is part of the SPZ as opposed to an accretionary prism (Pérez-Cáceres et al., 2020; Díaz-Azpiroz & Fernández, 2021).

The undisputed SPZ is composed of Devonian-aged phyllites and quartzites overlain by a younger succession of volcanically-derived sedimentary deposits interbedded with carbonaceous and siliceous shales and chert (Oliveira, 1990). The volcanic-sedimentary zone of the SPZ also contains the massive volcanic sulfide deposits that make up the bulk of the so-called Iberian Pyrite Belt (Onézime et al., 2003). To the south, the volcanic-sedimentary zone gives way to a Carboniferous flysch sequence composed of shales and turbidites that formed within the sedimentary basin created by subduction during the Variscan Orogeny (Moreno, 1993).

2.2) Suture between the Ossa Morena and South Portuguese Zones

The allochthonous origin of the rocks of the SPZ along with interpretations of the Beja-Acebuches Metabasites as a dismembered portion of an ophiolite sequence led researchers to consider the OMZ-SPZ boundary as a NNE dipping tectonic suture representing the closure of the Rheic Ocean (Crespo-Blanc & Orozco, 1988). Further geochronological work has dated the mafic protolith of the BAM to be Carboniferous in age (~340 Ma) limiting the suture to the closure of a smaller, local ocean basin, rather than the closing of the large Rheic Ocean basin itself (Figure 2; Azor et al, 2008). In either case, the BAM marks the tectonic suture between adjacent OMZ and SPZ terranes (Figure 3; Simancas et al., 2003). During late stages of the Variscan collision, this suture was exploited as a locus for deformation by the Southern Iberian Shear Zone (SISZ) which affects rocks within the BAM and PdL. The final deformation in the region was accommodated by subsequent discrete ENE striking subvertical Variscan-aged sinistral strike-slip faults cross-cut and displace the SISZ (Díaz-Azpiroz & Fernández, 2005).

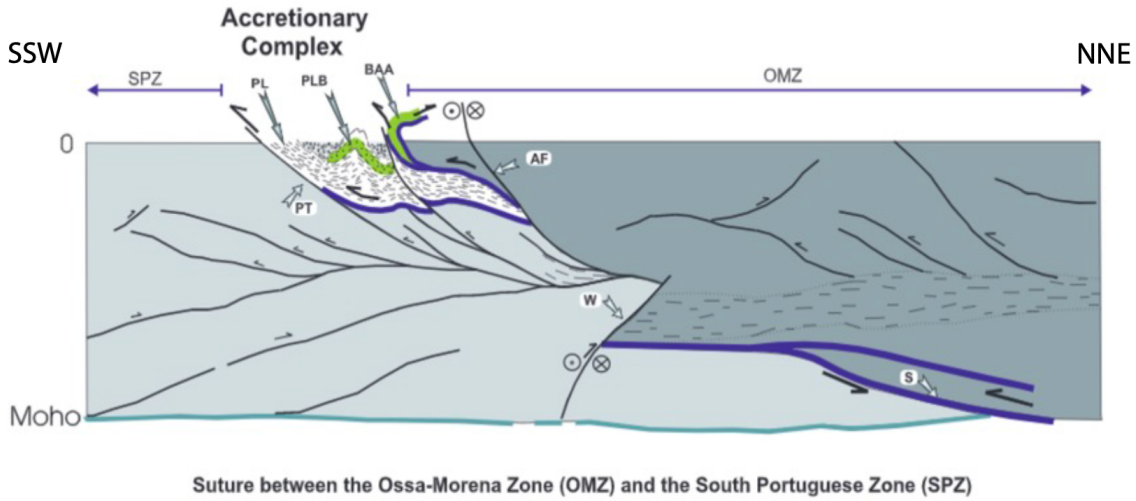

Figure 3: Cross-sectional view of the suture between the OMZ and SPZ (containing the SISZ) derived from a deep seismic reflection profile. The Beja-Acebuches Amphibolites are denoted BAA. The Pulo do Lobo sequence (PL) is divided into the Pulo do Lobo metasedimentary rocks, as well as a collection of basalts (PLB) contained within the

sequence as a whole. The Pulo do Lobo Thrust Fault is denoted PT, and the predominantly left-lateral Aroche Fault AF. The letters W and S highlight the seismically identified boundaries between the crustal blocks of the SPZ and the OMZ (From Simancas et al., 2003). The SISZ was a late-stage feature concentrating deformation along the boundary between the Beja-Acebuches metabasites and the Pulo do Lobo, which likely exploited earlier structures of this complex suture.

2.3) Southern Iberian Shear Zone

The SISZ is approximately 50 kilometers long, and ranges in width. The bounds of the SISZ within the BAM are well defined by structural evidence (Díaz-Azpiroz and Fernández, 2005), but the extent that the PdL is affected by the SISZ is not yet clear (Czeck et al., 2022); best estimates are that the total SISZ width ranges between 100-600 m. The average strike of the SISZ is 115° with an average dip of 50° to the northeast, though seismic data reveals the suture is listric at depth (Figure 3; Siamancas et al., 2003).

Previous structural analysis indicates that the SISZ is a complex transpressional shear zone that accommodates sinistral, thrust and flattening components of deformation, with the local kinematics partitioned differently within the BAM and PdL (Díaz-Azpiroz & Fernández, 2005; Fernández et al., 2013; Czeck et al., 2022). SISZ deformation (denoted as deformational event D_2 and discussed further in the unit descriptions) locally affected both the BAM and PDL following prior Variscan D_1 deformation and subsequent juxtaposition of the units.

2.4) Beja-Acebuches Metabasites

The Beja-Acebuches Metabasites are a collection of banded amphibolites and mafic schists that outcrop along a region over 100 km in length, and as a complete unit can reach a thickness of 600 meters in places (Díaz-Azpiroz & Fernández, 2005). Geochemically, the rocks of the BAM are clearly derived from MORB oceanic crust (Bard, 1969; Quesada et al., 1994; Castro

et al., 1996). At the structural top of the BAM, the amphibolites are coarse-grained (≥2 mm) with wide bands of plagioclase and hornblende. The uppermost amphibolites of the BAM are composed of plagioclase, amphibole (primarily hornblende), clinopyroxene, magnetite, ilmenite, and eventually, some minor quartz. Moving down through the unit, the amphibolites decrease in grain size (1-2 mm) and the bands become tighter and more visually striking. Compositionally the medium-grained amphibolites are similar to the overlying coarse-grained but without the presence of clinopyroxene, creating a distinct lithologic boundary between the two amphibolite groups (Díaz-Azpiroz & Fernández, 2005; Stephenson, 2018). Below the banded amphibolites, the composition of the BAM changes with closer proximity to the shear boundary between the BAM and the PdL. The amphibolites become much finer grained (<1 mm) and begin to display tight folding related to the thrusting of the BAM rocks. Eventually, the folding in the amphibolites becomes so tight that the rocks appear predominantly sheared, rather than folded. Nearest to the shear boundary, the composition changes again as a result of retrograde metamorphism, marked by the addition of epidote and chlorite, producing a layer of mafic chlorite schists (Díaz-Azpiroz & Fernández, 2005).

The BAM underwent two main phases of deformation, both related to Variscan orogenesis. The first deformational event (D_1) was a high temperature, low pressure contractional event that resulted in the creation of subparallel foliation and grain-size banding aligned with the OMZ-SPZ contact. Asymmetric shear sense indicators within the foliation fabric provide additional evidence of thrusting at this stage of deformation (Díaz-Azpiroz & Fernández, 2003). D_1 established an inverse metamorphic gradient in the BAM, with evidence for the

highest metamorphic temperatures visible at the structural top of the unit, the contact with the OMZ (Díaz-Azpiroz & Fernández, 2005).

A distinct localized second deformational stage (D_2), attributed to the SISZ, affects the BAM closest to the PdL contact, beginning roughly 450-500 m from the structural top of the unit (Díaz-Azpiroz & Fernández, 2005; Stephenson, 2018). The bounds of D_2 deformation in the BAM are delineated by the first observance of folded D_1 fabrics which are expressed as open folds up to 400 m away from the PdL boundary. These folds progressively tighten and rotate towards the boundary until they become isoclinal and thus difficult to identify within the banded amphibolites and completely unidentifiable within the chlorite schists. Along with progressive fold tightening, the increased presence of mylonitic foliation, stretching lineation, porphyroclasts with rotational asymmetry, and S-C and S-C' fabrics suggest that strain associated with the SISZ intensifies towards the contact (Díaz-Azpiroz & Fernández, 2005). Structurally, NW-SE trending foliated planes of amphibole and plagioclase as well as a visible lineation from amphibole crystals and crenulation cleavage highlight the dominant left-lateral transpression and variable extrusion direction across the shear zone (Figure 4; Díaz-Azpiroz and Fernández, 2005; Fernández et al., 2013).

D_2 also resulted in retrograde metamorphism among the BAM, further amplifying the inverse metamorphic gradient and superimposing a more abrupt retrograde pattern near the shear zone (Díaz-Azpiroz & Fernández, 2003). These deformational events are visible in the lithology of the BAM; with the highest-grade banded amphibolites near the top of the unit retrograding into mylonitized amphibolites and finally mafic schists towards the base of the unit.

Major element geochemistry determined via X-ray fluorescence on the BAM shows the formation near the SISZ is generally enriched in Ca and Al, and is depleted in Si (Stephenson, 2018). When plotted against distance from the SISZ, the data shows a positive correlation between mineral enrichment and the retrograde metamorphic path undergone by the metabasites. Further, the sporadic and localized nature of potassium enrichment within the formation highlights the effect of hydrothermal fluids on the retrograde metamorphism pathway and suggests channelization of those fluids along brittle fractures within the shear zone that allowed potassium likely derived from the PdL to be locally introduced into the BAM (Stephenson, 2018).

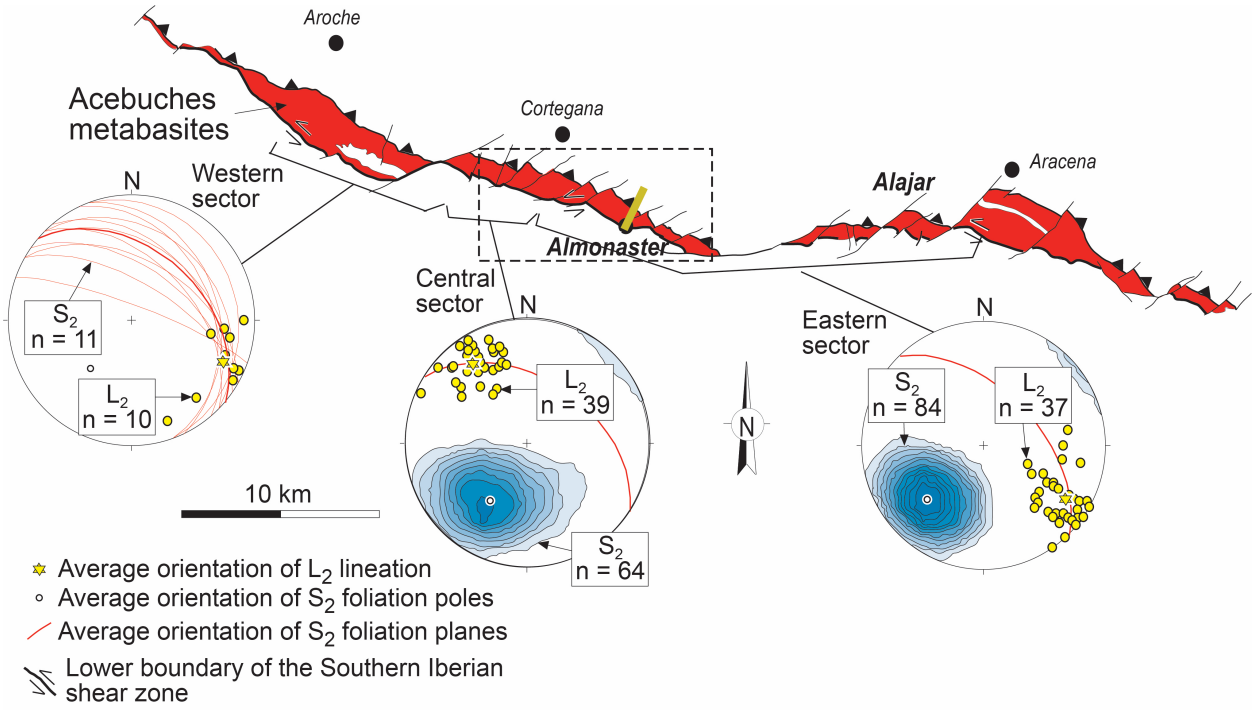

Figure 4: Equal area lower-hemisphere spherical projection of foliation and lineation orientation data from the Beja-Acebuches Metabasites along the SISZ. Note the change in lineation orientation along the shear zone, indicative of variable extrusion directions between segments (Díaz-Azpiroz and Fernández, 2005). The box indicates the central part of the SISZ shown in Fig 1b, and the transect near Almonaster, where samples for this study were collected, is identified. Modified from Fernández et al., 2013.

2.5) Pulo do Lobo Formation

The Pulo do Lobo Formation contains Frasnian-aged (~375 Ma) metapelites including fine-grained schists, phyllites, and slates along with intercalated beds of quartzite (Pérez-Cáceres et al., 2020). Along the Almonaster la Real transect, the field area for this research, rocks near the structural top of the unit, closest to the SISZ are the highest-grade schists and phyllites in the unit. These highly deformed rocks are strongly foliated with NE dipping wavy, highly fissile layers composed predominantly of micas and quartz. Beginning around 30 meters from the SISZ boundary, conspicuous quartzite layers begin to appear within the PdL. These layers are highly competent, and do not display any strong foliation or lineation. Further from the SISZ, the metamorphic grade decreases and the schists become gray, micaceous phyllites. This region contains abundant quartzite layers and is the most structurally complex due to the extreme lithology contrasts and highly localized deformation. Furthest from the SISZ (~170 m), the metamorphic grade of the PdL lessens once again, and the predominant rock type are muddy slates with intercalated quartzite. Deformation this far from the shear zone is minimal, and the rocks display typical slaty cleavage matching the overall regional fabric (Carman, 2020). It should be noted that the PdL varies greatly in lithology moving along the strike of the SISZ, so PdL outcrops outside of the Almonaster transect may appear differently in composition or configuration.

In contrast with the neighboring BAM, strain and metamorphism attributed to the D_2 SISZ in the PdL is only visible up to a maximum distance of roughly 150 meters from the contact with the BAM and is highly inconsistent across different lithologies. The metamorphic gradient related to the SISZ in the PdL also differs from that in the BAM; due to the low grade D_1

metamorphism, there is an overall metamorphic progression toward structural top of the PdL nearest the SISZ. Schists, the highest-grade rocks in the PdL, are found adjacent to the shear zone and metamorphic grade gradually decreases with distance from the SISZ to phyllites approximately 25 m away and slates more than 200 m away (Díaz-Azpiroz & Fernández, 2005). Adjacent to the PdL at its SW boundary lies the Ribeira de Limas Formation (RdL), a collection of similarly metamorphosed rocks that can make delineation of the PdL proper a challenge, leading different groups to place the boundary between the two in different locations (Braid et al., 2011; Dahn et al., 2014; Pérez-Cáceres et al., 2020). Field observations indicate that the RdL has generally less quartzite than the PdL with a more uniform low metamorphic grade equivalent to the adjacent slates in the PdL (Czeck, 2020 unpublished).

Tectonic schistose to phyllonitic foliations in the PdL, formed primarily by aligned micas, are prominent within the metapelites and subparallel to bedding and the orientation of intrafolial folds (Figure 5; Carman, 2020). Higher grade schistose foliation in the PdL tends to be more closely spaced than the lower grade slaty foliation and likely formed at higher strain. The strong rheology contrasts in the PdL also result in the formation of cm-m scale anastomosing shear bands that form borders around “lozenges” of lesser deformed rock composed often, but not always, of quartzite (Figure 6; Carreras et al., 2010; Czeck et al., 2022). Tectonic lineation is scarcely visible, most likely due to lack of acicular minerals. Where visible, lineation orientations vary widely within the foliation plane, with the most prevalent orientation being down-dip (Carman, 2020; Czeck et al., 2022). Asymmetric indicators, including sigma-type strain shadows, S-C fabrics, and asymmetric folds all indicate a top to the southwest thrust direction. Late stage

thrust shear bands with flat-ramp geometries are found throughout the schists and metapelites (Fig. 6).

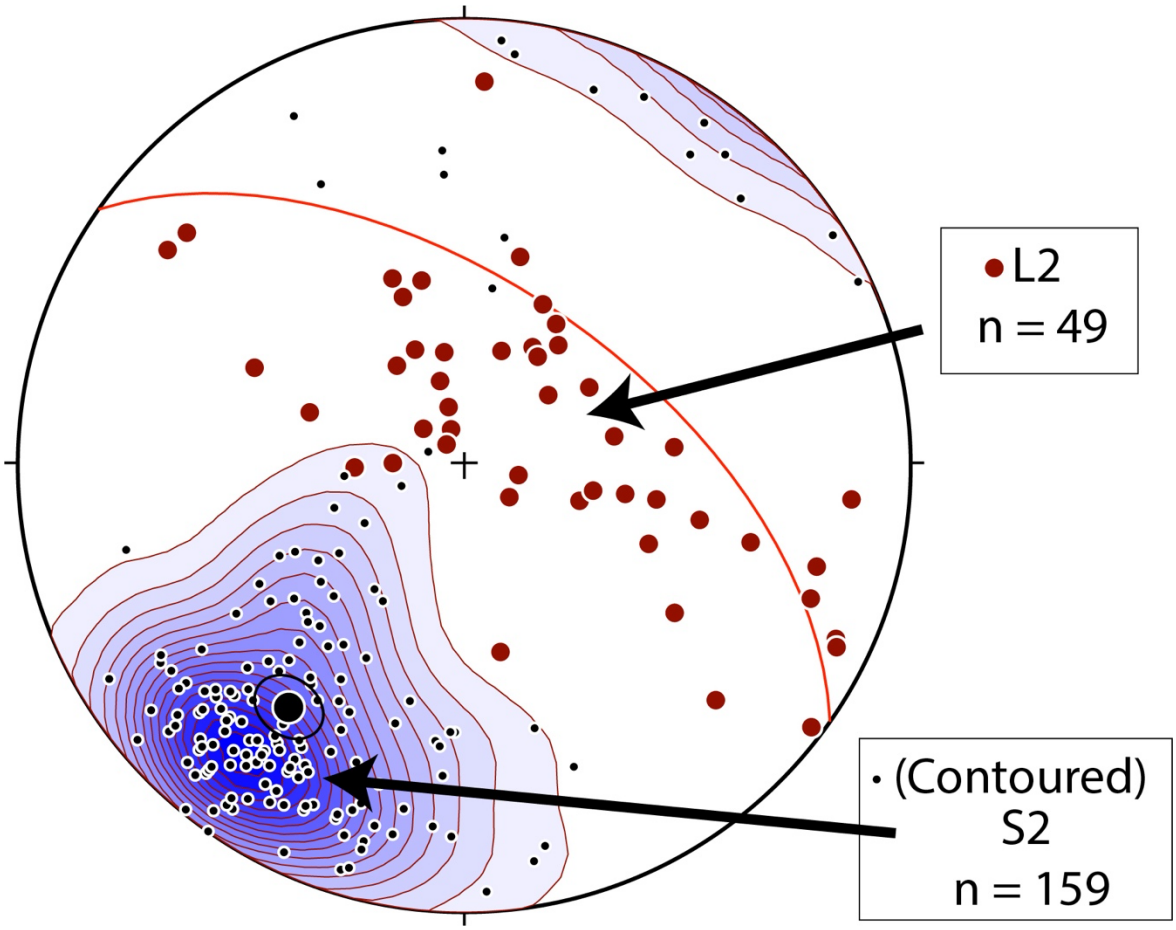

Figure 5: Foliation (S2) and lineation (L2) of the PdL presented on a lower hemisphere, equal area stereonet. Poles to the measured foliation planes are shown as black dots and contoured to show grouping. Average foliation plane is designated by the red great circle. Lineation measurements are shown as red dots (Czeck et al., 2022)

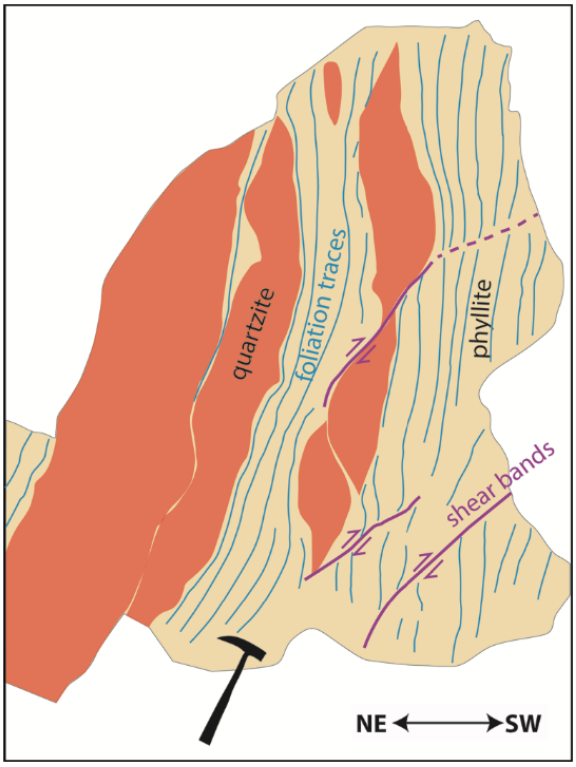
quartzite
foliation traces
phyllite
shear bands
NE
SW

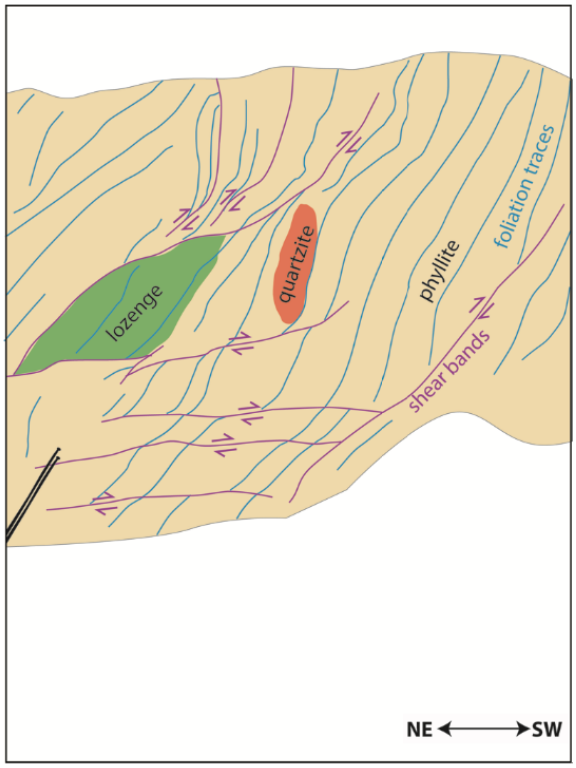
lozenge
quartzite
phyllite
foliation traces
shear bands
NE
SW

Figure 6: Illustrated field photographs showing low strain quartzite layers (orange) or quartz-rich phyllite lozenges (green) surrounded by higher strain pelitic phyllite (tan). Foliation traces for each outcrop are labeled, as well as observed shear bands. Note the highly heterogeneous nature of not only the outcrop lithology, but also fabric orientation. Strain is taken up by the phyllite, and the higher quartz portions are relatively undeformed with asymmetric structures formed around them. Thrust-created shear bands (top to the SW) cross-cut foliation planes and bend around competent lozenges and quartzite layers. In the top image, the quartzite layer displays some degree of boudinage, further emphasizing the competence contrast between the two lithologies (from Czeck et al., 2022).

Major element geochemical data from the PdL in proximity to the SISZ shows a number of interesting interactions (Carman, 2020). Arguably the most telling is the change in plagioclase composition with distance from the SISZ. Plagioclase composition increases substantially in Ca content approaching the SISZ, indicative of high temperature metamorphism. Moving away from the SISZ Na-rich plagioclase is predominant outside a range of a few hundred meters, indicative of much lower temperatures. This fluctuation in composition, combined with an enrichment in K_2O (similar to one observed in the BAM) indicates the influence of hydrothermal fluid migration on metamorphism within the unit, along with the mobilization of elements from some other location into that fluid (Carman, 2020). Isocon plots of the geochemical data show little to no change in major mobile elements such as Si, indicating a lack of volume change during deformation. In tandem with geochemical results from the BAM, the geochemical data highlight the channeling of fluids along the SISZ with migration outward through the units, perhaps along intermittent fractures (Stephenson, 2018).

3) Methods

3.1) Field Methods

Our Spanish colleagues, Dr. Manuel Díaz-Azpiroz and Dr. Carlos Fernández, collected 33 oriented samples of the PdL in the field. Samples were collected along a transect starting at the SISZ at a location in the village of Almonaster la Real along the Road of the Escalada, which runs along Rivera de Almonaster in the Huelva province in Andalusia, Spain. Previous researchers in our group studied rocks along this same transect (Stephenson, 2018 in the BAM; Carman, 2020 in the PdL). Samples were collected along the transect beginning from an outcrop of schists abutting the shear zone itself, and then taken from suitable outcrops moving away from the shear zone, up to a distance of around 175 meters away. Samples were collected from the highest-grade schists in the unit, as well as several from the phyllite region, including some of the quartzite beds. Orientation measurements were made using a geologic compass and marked on the samples. Additional notes were recorded in the field including foliation and lineation measurements, macroscopic lithology observations, and whether the sample was taken from the top or bottom face of the outcrop. The samples were then shipped to the UWM campus to be prepared for AMS analysis.

3.2) Anisotropy of Magnetic Susceptibility (AMS)

Scientists have long studied magnetic materials, but it wasn't until the mid-twentieth century that the idea of remanent magnetism – that rocks retain the magnetic orientation from when they were cooled below a certain temperature – was first identified and described (Néel, 1949). Work began in earnest on the paleomagnetic implications of this discovery, and

scientists quickly realized the magnetic fabrics were more complicated than originally believed. Additional methods of observing magnetic alignment in rocks were discovered, this time using magnetic susceptibility of rocks, or the ratio of magnetization to an applied magnetic field (K=M/H). Research by Nye (1957) revealed that the magnetic susceptibility of rock-forming minerals is not uniform, but rather anisotropic, with each mineral combining to form an overall susceptibility ellipsoid within the bulk rock based primarily on the grain orientation and shape of magnetic minerals within the rock. This new method using magnetic susceptibility could identify magnetic fabrics even in rocks that have little or no permanent remanent magnetism. While AMS was initially used for paleocurrent studies in sediments, John Graham (1966) was one of the first scientists to notice the effect tectonic deformation had on the susceptibility orientation while researching the magnetic fabric of deformed rocks in the Appalachians.

The use of AMS orientation to establish tectonic fabrics in rocks rapidly became a topic of much research in the geosciences community (Jelinek, 1977; Hrouda, 1982) and the practice has been well-utilized in deformed rocks of all types. In igneous rocks, not only has AMS been used to find tectonic fabric in plutons (Aranguren et al., 2003; Burton-Johnson et al., 2019), it has also been used to determine magma flow direction and trace it back to a source, a practice similar to its roots in sedimentology (Hillhouse & Wells, 1991; Glen et al., 1997). In highly deformed rocks like migmatites, AMS can be used to identify petrofabrics that are often obscured by metamorphic recrystallization (Aranguren et al., 1996; Ferré et al., 2003). One of the most effective known uses of AMS is work using it to identify fabrics – tectonic or otherwise - in deformed sedimentary rocks, as magnetic alignment is known to occur even in weakly deformed rocks (Parés et al., 1999; Parés & Van der Pluijm, 2003; Soto et al., 2009; Weil &

Yonkee, 2009; Cifelli et al., 2015). Even in highly heterogeneous, complicated shear zone regions, AMS is an extremely useful tool in identification of tectonic fabric (Kontny et al., 2012; Robustelli Test & Zanetta, 2021).

The primary reason AMS is so useful in structural geology is predicated on the relationship between the orientation and shape of a rock's magnetic susceptibility ellipsoid and the orientation of the strain ellipsoid that formed the magnetic fabric. Both the magnetic fabric and the tectonic fabric are created by the alignment of mineral grains, and therefore the fabrics that arise from that alignment are often coaxial (Borradaile, 1988; Jackson & Tauxe, 1991; Tarling & Hrouda, 1993). A constructed susceptibility tensor derived from AMS measurements provides the orientation and magnitude of three magnetic susceptibility axes denoted K_1, K_2, K_3; or as K_{max}, K_{int}, and K_{min} respectively. Many magnetic mineral assemblages allow a straight-forward correlation between orientations of magnetic anisotropy axes and tectonic fabrics in which K_3 is parallel to the direction of maximum shortening, and therefore is the pole to the magnetic and tectonic foliation plane. K_1 is often parallel to the direction of maximum extension, and thus may represent the orientation of tectonically-derived stretching lineation (Figure 7; Parés & Van der Pluijm, 2002; Burton-Johnson et al., 2019).

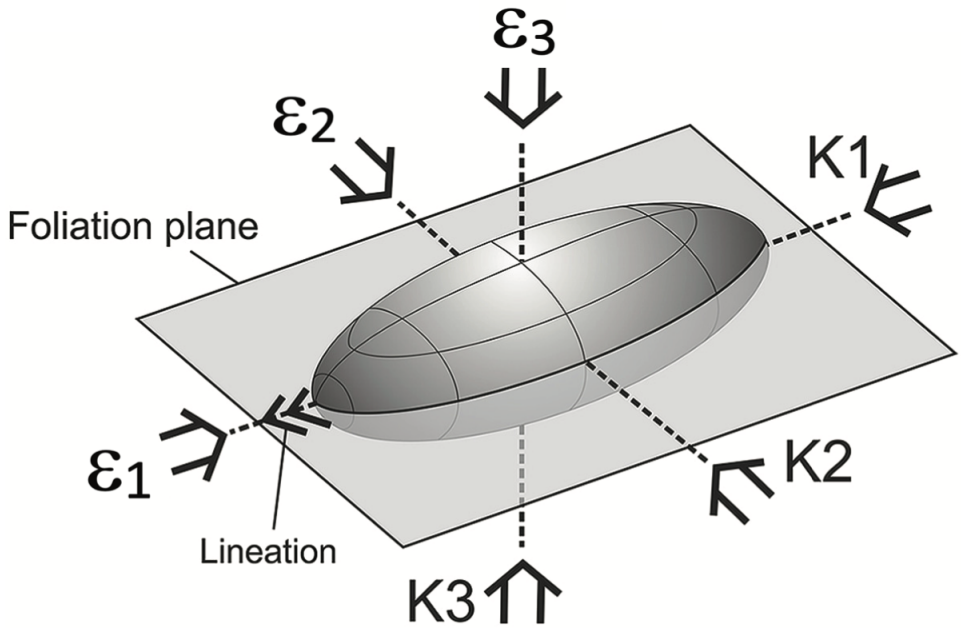

Figure 7: Illustrated relationship between primary axes of the magnetic susceptibility ellipsoid (K_1, K_2, K_3) and strain ellipsoid axes (ε_1, ε_2, ε_3) highlighting the orientation of both as they relate to foliation and lineation fabrics in a rock (modified from Burton-Johnson et al., 2019)

Despite the established general relationship between the magnetic susceptibility and strain ellipsoids, magnetic susceptibility is highly dependent on magnetic mineralogy and method of deformation, so it is imperative that one use caution in interpreting the relationship between the magnetic anisotropy and strain axes, especially when attempting to use magnitude of susceptibility as a proxy for strain magnitude (Jackson & Tauxe, 1991). Additionally, samples with low bulk susceptibility, which can often be the case in mudrocks, may also lack enough of a magnetic signal to create a fabric at all (Borradaile & Henry, 1997). In all cases when using AMS fabrics, it is extremely important to establish precisely which minerals are contributing to the AMS fabric and the deformation mechanisms active in the creation of

the magnetic fabric in order to properly interpret the AMS data as compared to a sample's tectonic fabric.

3.3) AMS Methods

Upon arrival at UWM the samples were cut with a variety of lapidary saws using a method to preserve orientation measurements on the samples. The rocks were first cut into 2 cm wide slabs oriented along right hand strike of the foliation plane. Following that, the slabs were cut along the foliation plane to a height of 2 cm, then finally cut down into finished cubes of 2 centimeters in length per side, with orientation markings based around the foliation plane of the samples, necessary for the orientation of AMS measurements (Figure 8). For samples taken off the bottom face of an outcrop in the field, the orientation measurements were projected through to the top surface of the sample, and then cut according to the same method.

In order to obtain a measurement of the anisotropy of magnetic susceptibility (AMS) of the samples, the oriented cubes were inserted into an AGICO MFK1 Kappabridge susceptibility bridge (Figure 9) where the three-plane rotation method (Figure 10) was utilized to obtain values necessary to construct a susceptibility tensor according to the methods established by Jelinek (1977). Data were collected using AGICO Safyr7 data acquisition software. In total, measurements were made on 93 oriented specimen cubes from 20 total samples.

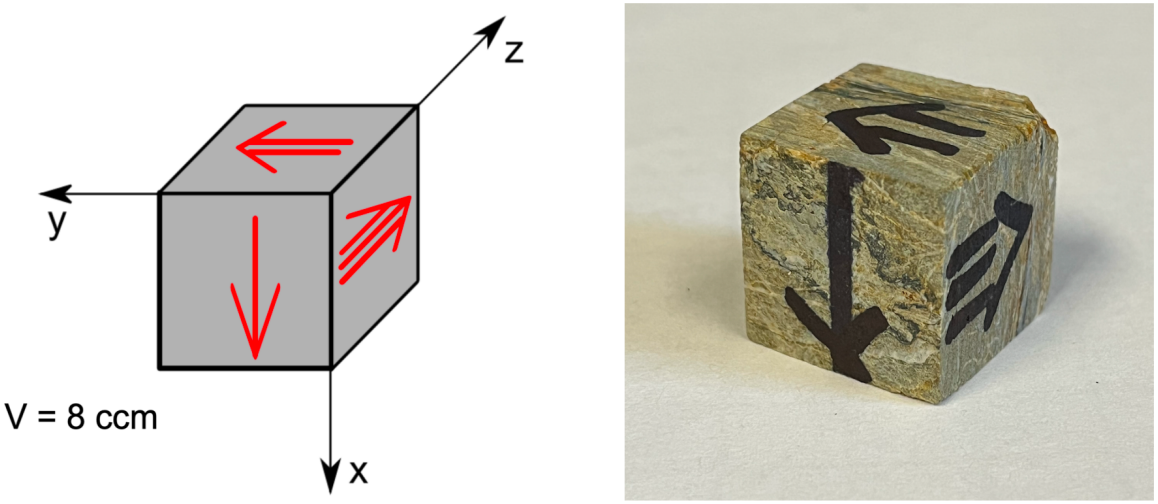

Figure 8: Illustration and sample picture showing orientation of samples prepared for AMS research. The single arrow X direction is the direction of strike, double arrow Y is the dip direction of the plane of orientation, and triple arrow Z is normal to the plane of orientation into the sample. For these samples, the plane of orientation was the measured foliation plane, striking in the x-direction (using right-hand rule), and dipping to the y-direction (modified from Chadima, 2021).

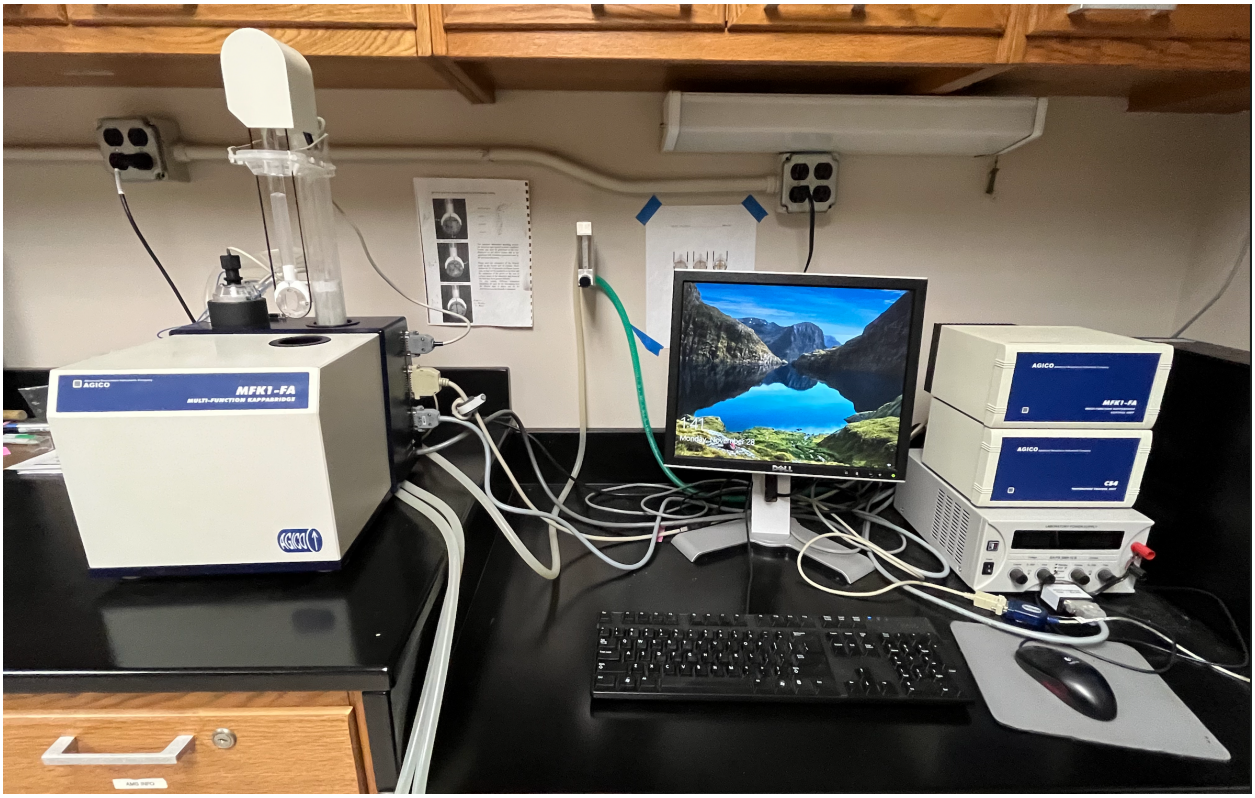

Figure 9: Photograph of the MFK1-FA multifunction Kappabridge in the geomorphology lab at UWM which was used for AMS research.

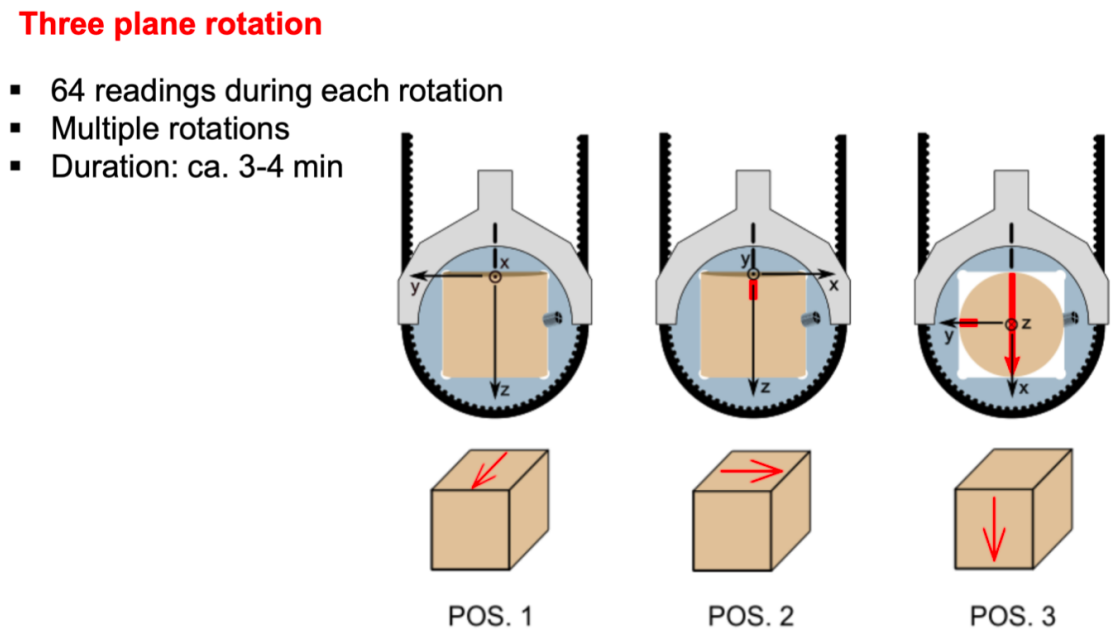

Figure 10: Example of three plane rotation method for measuring AMS using a Kappabridge. Note the orientation symbols on the sample. The single arrow (X axis) is aligned with the strike of the plane of orientation in the sample. It is important to properly orient the sample in the holder for proper interpretation of results (modified from Chadima, 2021).

Parameters of the Kappabridge were set in the AGICO Safyr7 program according to the sampling orientation, with P1 = 3, indicating a single arrow X direction fiduciary mark oriented with right hand rule strike of the foliation plane. P2 was set to 0, since the samples were cut along the dip of the foliation plane. P3 was also set to 3, with the measured right hand rule strike on the sample aligned with the single arrow fiduciary mark. Finally P4 was set to 90, which signifies the orientation plane was measured using right hand strike and dip.

Data was analyzed using the AGICO Anisoft Advanced Treatment of Magnetic Anisotropy Data software which provided susceptibility axis results in both specimen and geographic coordinate systems according to the input orientation measurements and Kappabridge parameters. The least square inversion method described by Jelinek (1981) was

used to acquire second rank magnetic susceptibility tensors for the samples, the eigenvalues and eigenvectors of which define the orientation and magnitude of the principal susceptibility axes (K_1, K_2, K_3). The Anisoft software also provided bulk susceptibility measurements as defined below:

$$K_{mean} = \frac{K_1 + K_2 + K_3}{3}$$

Other quantitative anisotropy parameters such as the shape parameter (T) were also calculated:

$$T = \frac{2\eta_2 - \eta_1 - \eta_3}{\eta_1 - \eta_3} \text{ where } \eta = \ln(K_x).$$

Shape parameter values between -1 and 0 represent prolate ellipsoids while T values between 0 and +1 indicate an oblate fabric. Adjusted degree of anisotropy (Pj), is calculated using the axial ratio P = (K_1/K_3) then adjusted for the shape parameter using the equation:

$$Pj = exp\sqrt{2((\eta_1 - \eta_m)^2 + (\eta_2 - \eta_m)^2 + (\eta_3 - \eta_m)^2)} \text{ where } \eta_m = \frac{\eta_1 + \eta_2 + \eta_3}{3}.$$

3.4) <u>Magnetic Characterization Methods</u>

Additional samples from the Almonaster la Real transect that were collected in a previous field campaign by members of our research group (Carman, 2020). These 21 samples were selected to represent a range of lithologies and strain levels along the transect, from

within 20 meters from the SISZ up to ~190 meters away. The prepared samples were brought to the Institute of Rock Magnetism at the University of Minnesota for magnetic property analysis. The previously powdered samples were divided and weighed, then loaded into plastic capsules sealed with polymide tape. The capsules were then inserted into plastic straws that acted as sample holders for the various machines in the lab.

Bulk magnetic susceptibility of a rock, and the susceptibility axes measured by AMS are determined by the interaction of all its constituent minerals. It is important to differentiate which minerals are contributing to the magnetic fabric because different components can display different AMS patterns. Magnetite dominated AMS patterns tend to be closely linked to the grain shape of the magnetite itself (SPO), while magnetic fabrics created by phyllosilicates or more magnetically resistant (higher coercivity) minerals like hematite are generally more reflective of crystallographic orientation (CPO). In either case, orientation of the magnetic grains is often related to the tectonic forces experienced by the rock (Páres & Van der Pluijm, 2002).

Magnetic hysteresis data (magnetization as a function of an applied magnetic field) was performed on the samples by sweeping a magnetic field from +1T to -1T and back (e.g., Figure 11). Hysteresis is used to determine the dominant magnetic material susceptibility within the sample, whether a material is para-, dia-, or ferromagnetic. All minerals have magnetic susceptibility. Paramagnetic minerals have a positive susceptibility, while diamagnetic minerals have a negative susceptibility (Hunt et al., 1995). Both para- and diamagnetic minerals are magnetic only in the presence of a magnetic field and lose magnetism when removed from the field. In contrast, ferromagnetic minerals have a strong positive magnetic susceptibility and can

maintain magnetism even after the applied field is removed, known as remanent magnetism (Néel, 1949). This remanent magnetism can be measured using the y-intercept of the hysteresis loop (Figure 11). Coercivity of the sample, or the sample's resistance to magnetization, is calculated using the x-intercept of the loop (Roberts et al., 1995). A dia- or paramagnetic sample with minimal remanence and coercivity is therefore a line that crosses through the origin, either positively sloped (paramagnetic) or negative (diamagnetic). The slope of the line is equal to the susceptibility of the material (Jackson & Solheid, 2010). Hysteresis loops and DC demagnetization (DCD) curves were measured for all samples using a Lakeshore 8600 vibrating sample magnetometer (VSM). Hysteresis and demagnetization curve data from the samples was imported into the IRM database for further analysis (Appendix C).

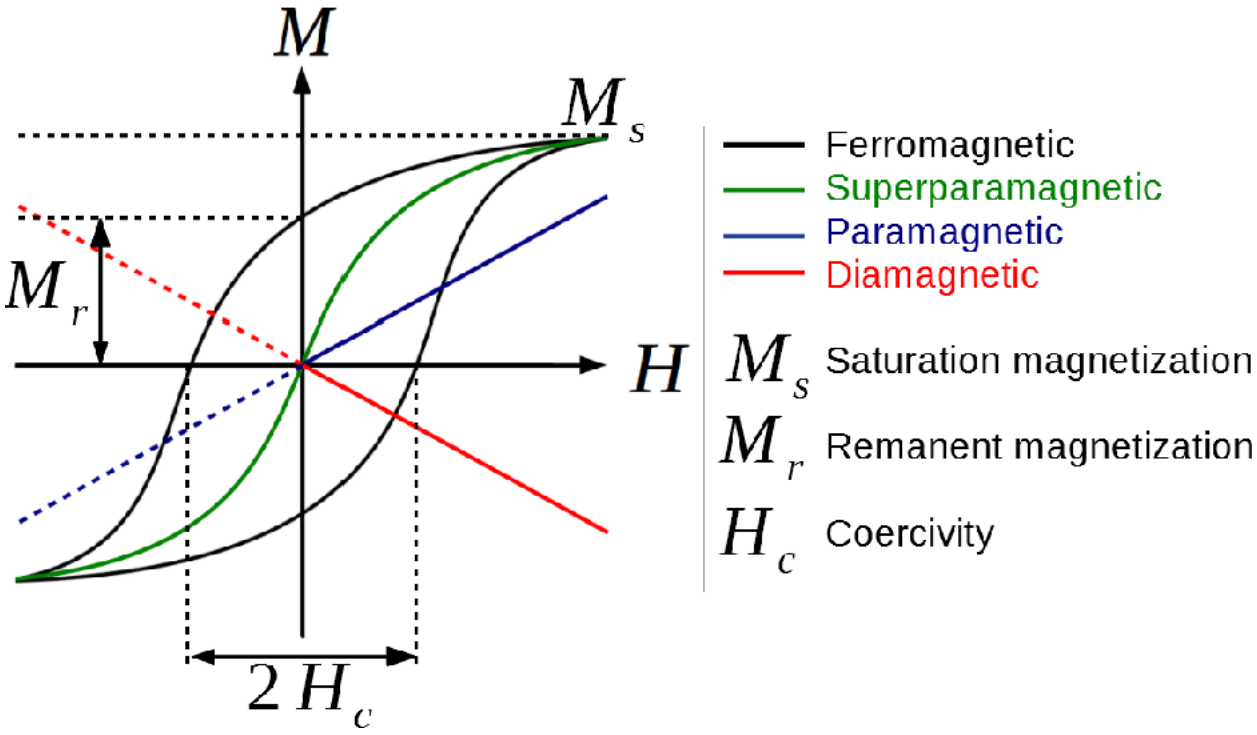

Figure 11: Schematic diagram of a hysteresis loop for a variety of magnetic materials. Remanent magnetism of the material is calculated using the y-intercept on the loop (labelled M_r) while coercivity (H_c) of the material is equal to the x-intercept. Note that paramagnetic materials do not exhibit remanence and instead take on magnetism only in the presence of a magnetic field. The slope of the paramagnetic line is equal to the susceptibility of the material (Venäläinen, 2018).

First order reversal curves (FORC) for a pair of samples were also run using the Lakeshore VSM with the intention of identifying the domain state of any ferromagnetic minerals in the samples (Muxworthy et al., 2005). However, the weak bulk magnetism of the samples resulted in such low resolution the data was rendered inconclusive.

Samples were also run through low-temperature saturated isothermal remanent magnetism (LTSIRM) tests on a Quantum Design cryogenic magnetometer magnetic property measurement system (MPMS-XL). Saturated isothermal remanent magnetism (SIRM) is a measure of the maximum remanent magnetism obtained by the sample. The primary reason for LTSIRM experiments is to further identify possible magnetic contributors. A selection of 13 samples, representing a spread of distance from the SZ as well as a representative sample of different PdL lithologies were measured using this LTSIRM method (Appendix C).

Additional LTSIRM data was obtained using field cooled and zero field cooled experiments on the MPMS, in which samples are cooled from 300K (room temperature) to 20K both with and without the presence of a magnetic field. Samples where the field cooled saturated isothermal remanent magnetism (FC-SIRM) is higher than the zero-field cooled saturation isothermal remanent magnetism (ZFC-SIRM) can highlight the presence of secondary iron-bearing minerals like goethite (Smirnov, 2009). Due to time and equipment constraints, only 4 samples spaced out along the transect were able to be run in this manner (Appendix B).

An additional set of 13 samples, selected again in an attempt to create a representative set of lithologies and distances from the SZ were weighed and prepared for high temperature susceptibility measurements using a Geofyzika KLY-2 Kappabridge. The samples were heated to over 600°C and then cooled back down to room temperature while the bulk susceptibility of the

samples is measured. This process can help identify ferromagnetic minerals initially present in the sample by highlighting the Curie or Neél transitions within the samples (Jackson & Moskowitz 2021; Walz 2002). Even without substantial ferromagnetic components, a large increase in susceptibility visible on cooldown is directly related to the formation of magnetite from other iron-bearing paramagnetic minerals within the sample during heating (Liu et al., 2020).

4) Results

4.1 Field Observations

Our colleagues, Manuel Díaz-Azpiroz and Carlos Fernández collected the PdL samples studied here and reported structural measurements and notes on lithology (Appendix A). The samples were taken along a transect at distances between 0 and 176.3 m away from the inferred position of the SISZ, which coincides with the inferred contact between the BAM and PdL. The contact is not exposed but is known to be within approximately 2 m. Highly foliated schists exist adjacent to the shear zone, and grade to phyllites within a few meters. Beginning at a distance of roughly 30 meters from the shear zone, several conspicuous quartzite layers are interbedded with phyllite. Sigmoidal shapes are displayed in the rocks coincident with the appearance of the quartzite layers, possibly related to the competence contrast between the quartzite and phyllite. Samples were taken of the schists, phyllites, and quartzites.

Structural fabrics in the PdL were measured in the field during collection of the AMS samples (Appendix A). These fabric measurements were taken on the sample or within a few cm away from the sample location. Foliations are consistently oriented, with an average orientation of 303/67NE (Figure 12A). This orientation matches that of foliations throughout the transect. Lineation orientations were much less consistent but show a girdled pattern across the average foliation plane (Fig. 12B), similar to others measured across the transect. Roughly half of the measured lineations are clustered parallel or subparallel to dip direction on the foliation plane.

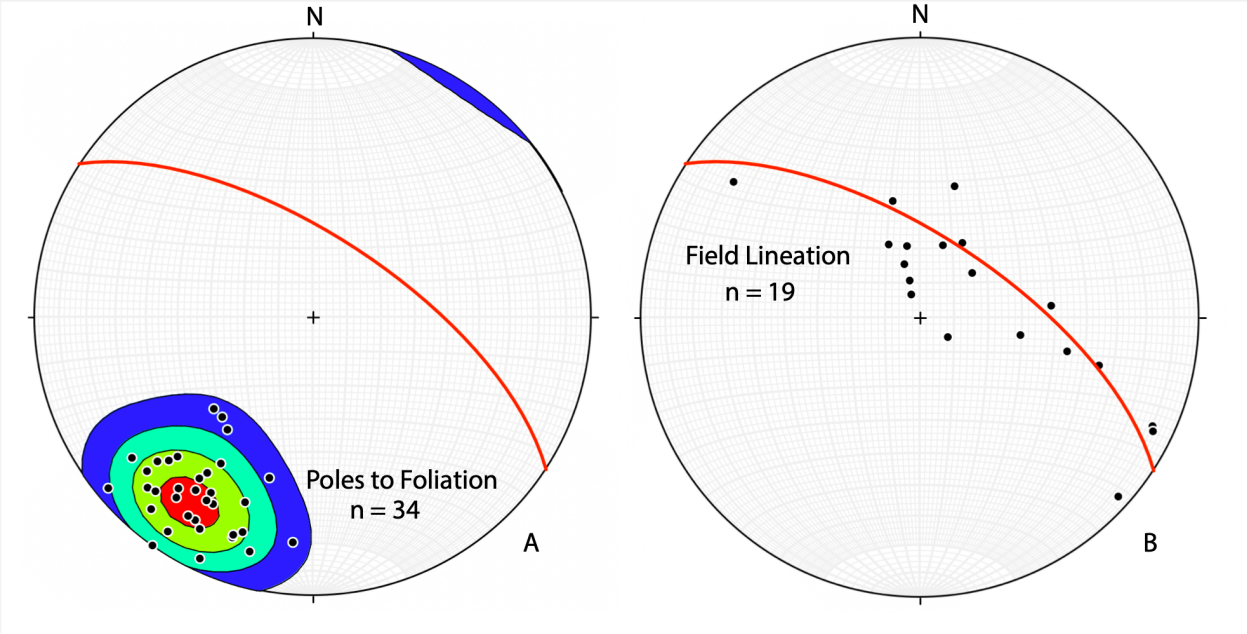

Figure 12: Structural fabric measurements associated with samples used in this study from the Pulo do Lobo along the Almonaster la Real transect. A) Contoured poles to foliation measurements are plotted along with the average foliation plane (shown in red). B) Field lineation measurements plotted along with the average foliation plane highlighting a girdled pattern along the average foliation plane. Down-dip lineation measurements are located toward the center of the foliation plane arc.

Foliation and lineation orientation measurements taken in the quartzite layers are relatively consistent with measurements taken in the phyllite. Despite the consistency, lineation quality is adversely affected by the addition of the quartzite beds, and the most conspicuous lineation measurements were taken in the phyllites closest to the shear zone (Díaz-Azpiroz, 2021 unpublished).

4.2 Magnetic Properties

All samples taken from the Almonaster transect that were tested at the IRM showed similar broad magnetic property characteristics (Appendix C). The magnetism of the samples was quite low, indicating an abundance of low magnetism paramagnetic minerals in the samples. Hysteresis loops confirmed the paramagnetic nature of the samples (Figure 13),

showing very weak magnetism, low magnetic susceptibility, and a distinct lack of remanent magnetism, illustrated by the closed, compressed loop with very low y-axis values.

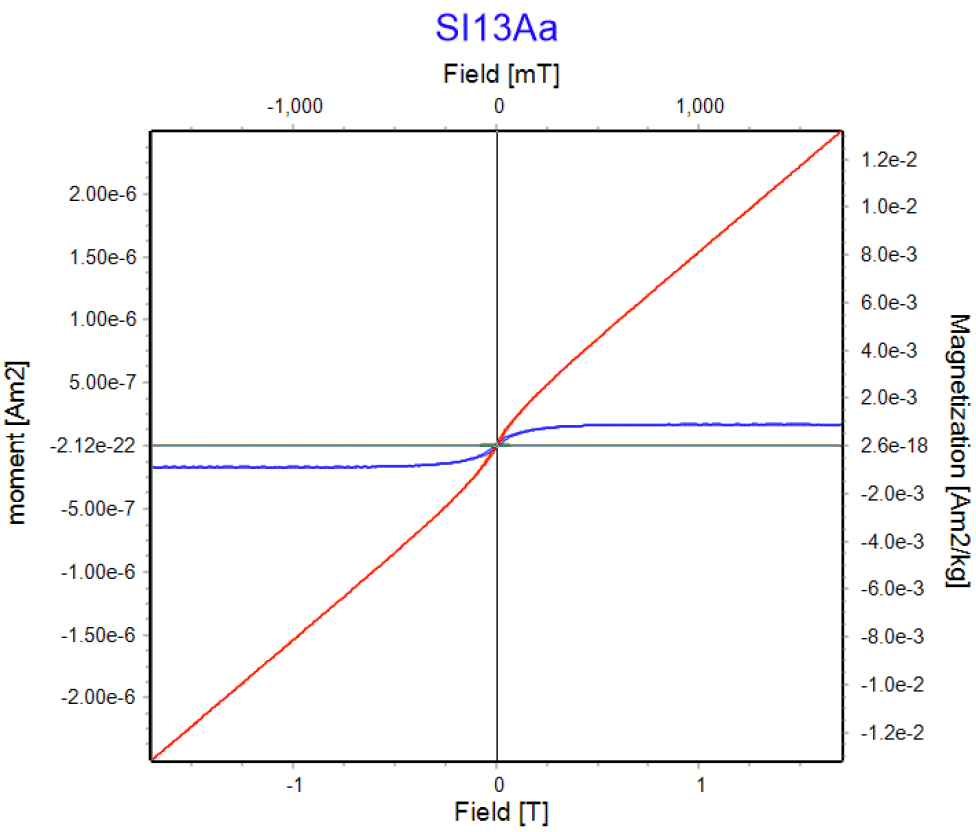

Figure 13: Typical hysteresis loop (in blue) for one of the Almonaster transect samples from the PdL. Note the lack of remanent magnetism (closed loop) and the low magnetic moment (y-axis value) indicating the samples are only weakly magnetic and are dominated by paramagnetic minerals.

DC demagnetization curves (Figure 14A) for the samples show the presence of at least three probable ferromagnetic contributors when unmixed using the MAX Unmix program (Figure 14B; Maxbauer et al., 2016). The proportionally highest component displays magnetic coercivity values similar to hematite, with other components at coercivity levels similar to goethite and detrital titanomagnetite. All samples taken from the PdL had some combination of

these ferromagnetic minerals present, though the extremely weak hysteresis illustrates their limited contribution.

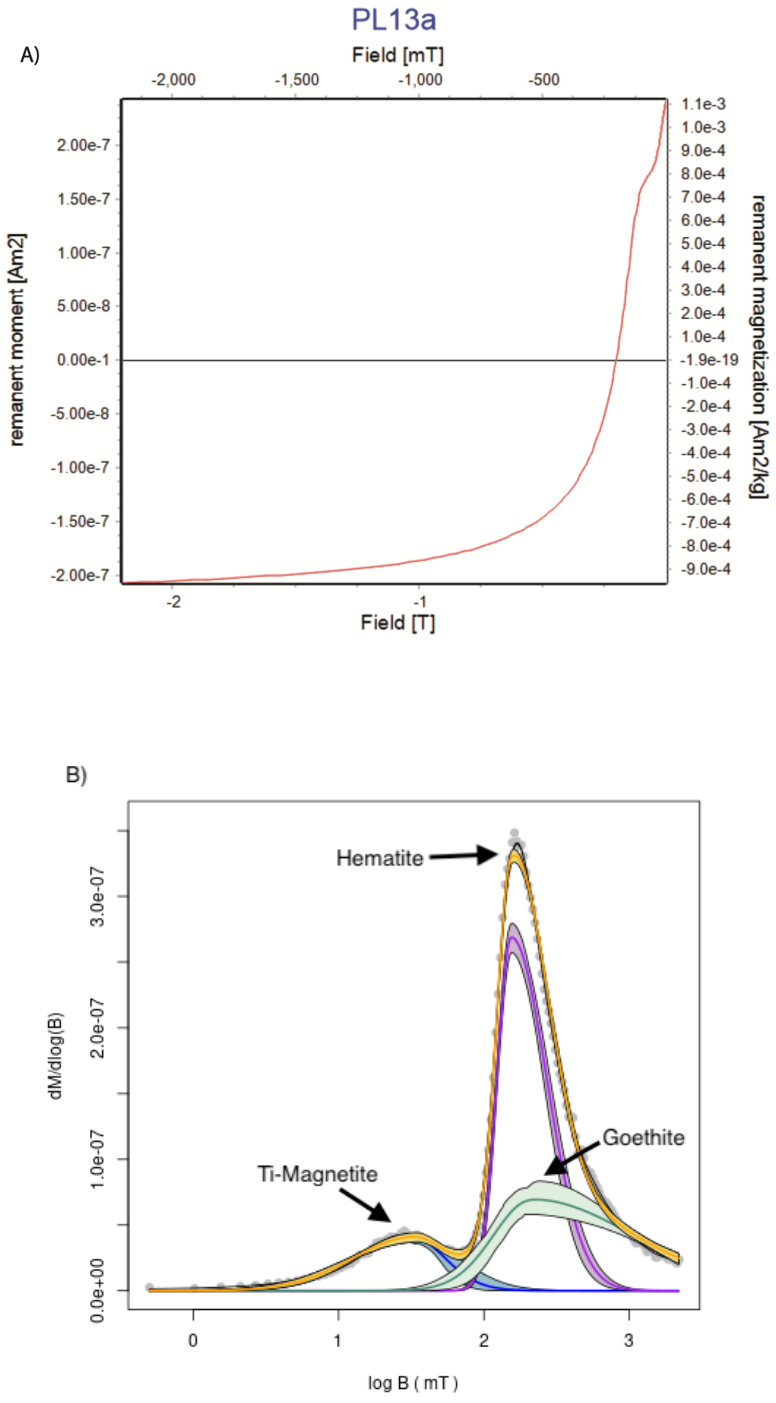

Figure 14: A) DC Demagnetization curve raw data (top) and B) unmixed using the MAX Unmix program (bottom). Unmixing the curve led to the identification of at least three ferromagnetic contributors, with the highest proportional component consistent with the high coercivity mineral hematite.

Testing samples' susceptibility as a function of temperature (Figure 15) shows a Curie temperature transition around 550° on heating, consistent with low-Ti titanomagnetite. Additionally on heating, the overall magnetic susceptibility drops from its initial value as the molecules vibrate more strongly and have greater difficulty aligning. This is consistent with the general behavior of paramagnetic minerals. Upon cooling, the susceptibility greatly increases due to the creation of ferromagnetic minerals that occurs during the heating of the sample.

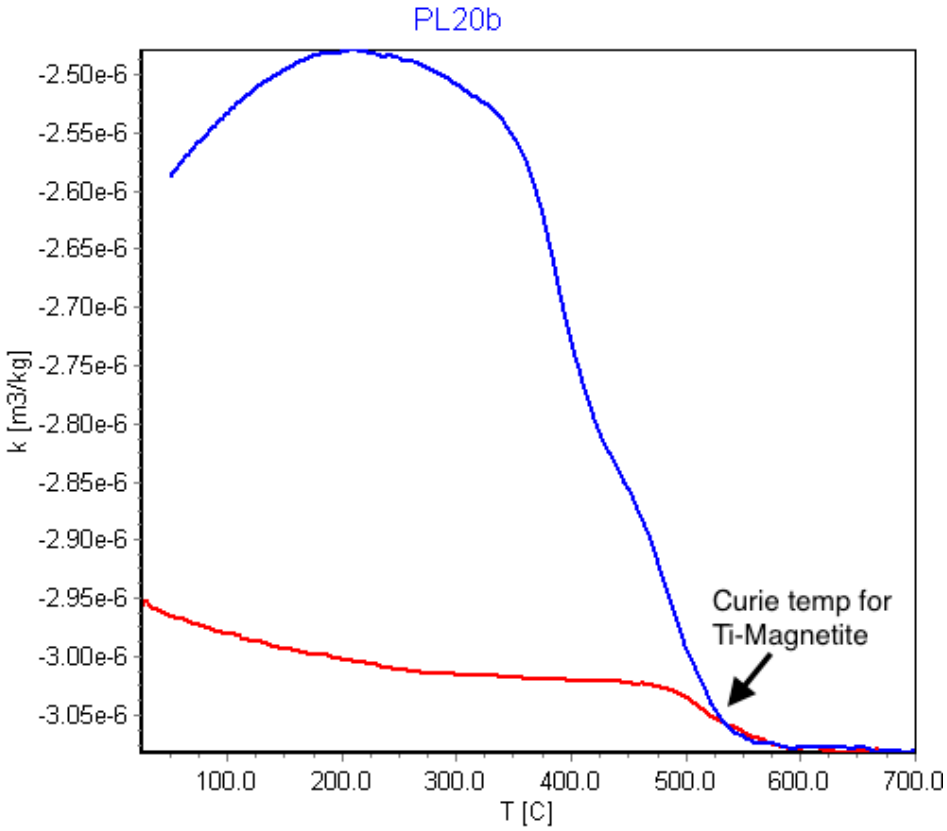

Figure 15: Susceptibility as a function of temperature plot typical of the Almonaster transect samples. Note the decrease in susceptibility upon heating (red line), consistent with the presence of paramagnetic minerals, as well as the Curie temp transition around 550°C. Upon cooling (blue line) the susceptibility increases substantially with the creation of ferromagnetic minerals due to heating.

Additional magnetic property testing was conducted on the Almonaster transect samples, including field-cooled and zero field-cooled saturated isothermal remanent magnetism (SIRM) measurements (Figure 16). The data acquired seems to confirm the presence of goethite as a secondary mineral, as determined by the much higher values of field-cooled remanent magnetism.

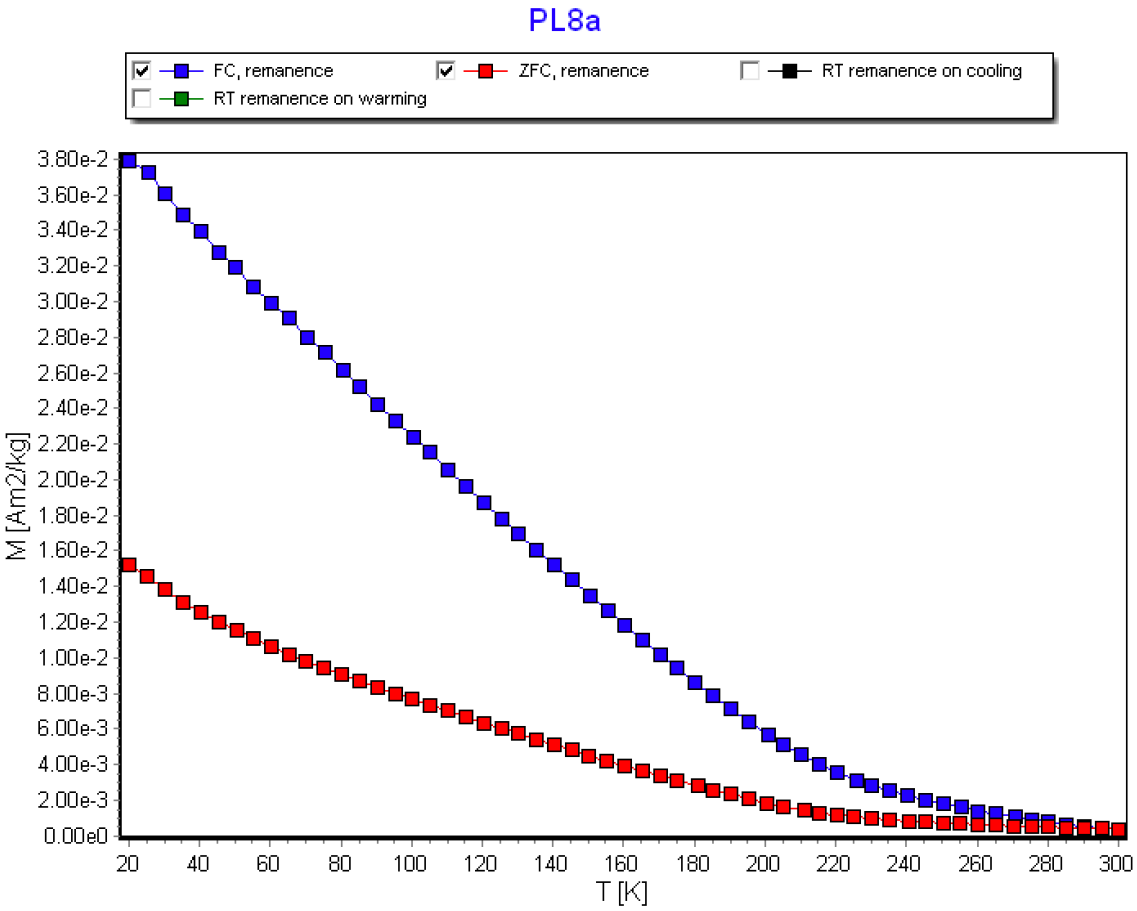

Figure 16: Field-cooled and zero-field cooled saturated isothermal remanent magnetism (SIRM) curves for sample from the Almonaster transect. The greater remanence in the FC curve is indicative of goethite in the samples.

Despite the presence of some ferromagnetic contributors (titanomagnetite, hematite, goethite), the paramagnetic hysteresis and the very low susceptibility values (average Kmean = 119 SI^{-6}; Figure 17) indicate that the samples are overwhelmingly paramagnetic in nature. This

assertion is supported by point counting performed on the samples from the same transect (Figure 18), which show the samples to be composed almost exclusively of quartz and micaceous minerals, with negligible amounts of opaque ferromagnetic minerals (Kopinski, 2022). Common mineral arrangements in the PdL as described by Carman (2020) are quartz, muscovite, biotite, with some trace feldspars and chlorite close to the SZ while further away muscovite becomes much more prevalent than biotite, while quartz content also drops off somewhat. Theoretically as well, the assertion is supported by previous studies that demonstrate that low susceptibility sedimentary or deformed metasedimentary rocks have their magnetic signals carried almost exclusively by the iron-bearing silicates contained within them (Figure 19, Parés, 2015)

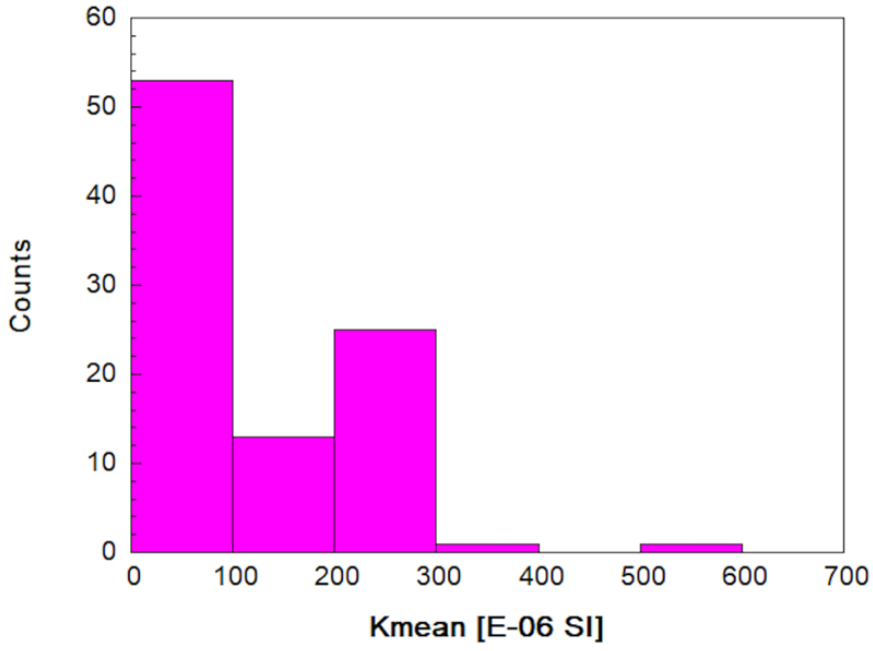

Figure 17: Mean susceptibility data for the PdL samples used for AMS research. Most of the samples had very low susceptibility, indicative of predominantly paramagnetic composition consistent with lithology.

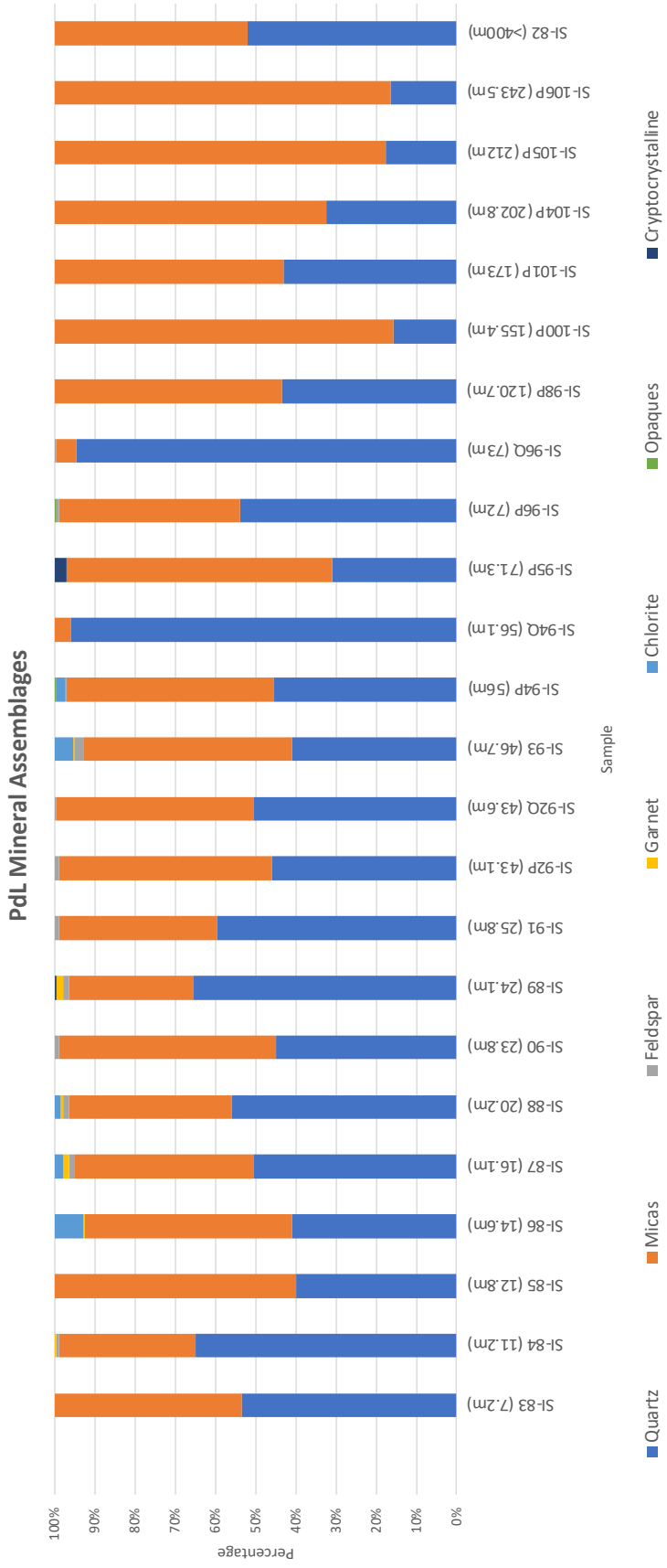
PdL Mineral Assemblages
Percentage
100%
90%
80%
70%
60%
50%
40%
30%
20%
10%
0%
Sample
SI-83 (7.2m)
SI-84 (11.2m)
SI-85 (12.8m)
SI-86 (14.6m)
SI-87 (16.1m)
SI-88 (20.2m)
SI-90 (23.8m)
SI-89 (24.1m)
SI-91 (25.8m)
SI-92P (43.1m)
SI-92Q (43.6m)
SI-93 (46.7m)
SI-94P (56m)
SI-94Q (56.1m)
SI-95P (71.3m)
SI-96P (72m)
SI-96Q (73m)
SI-98P (120.7m)
SI-100P (155.4m)
SI-101P (173m)
SI-104P (202.8m)
SI-105P (212m)
SI-106P (243.5m)
SI-82 (>400m)
Quartz
Micas
Feldspar
Garnet
Chlorite
Opaques
Cryptocrystalline

Figure 18: Mineral assemblages of samples along the Almonaster transect of the PdL. Numbers obtained via point counting of samples under a petrographic microscope. Samples denoted with a Q are taken from the quartzite beds within the PdL (Kopinski, 2022).

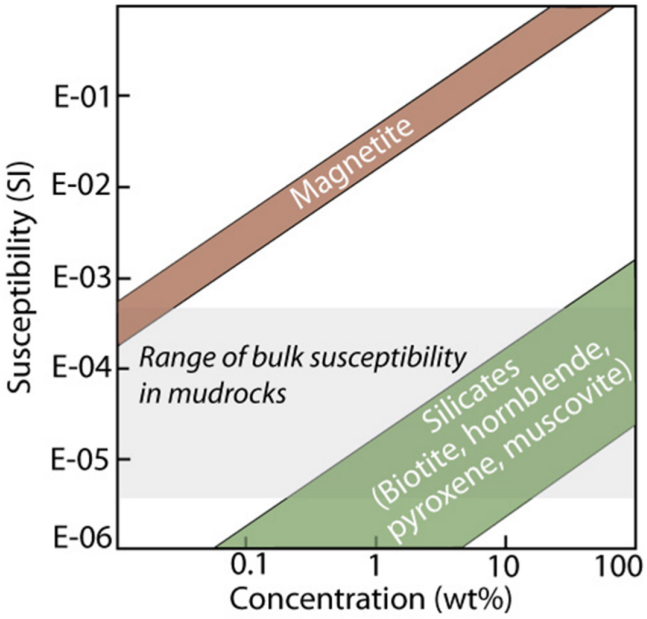

Figure 19: Figure taken from Parés (2015) illustrating the influence of iron-bearing silicates on the overall magnetic susceptibility of common mudrocks. Low susceptibility paramagnetic minerals carry the bulk of the magnetic signal in samples like those from the PdL.

4.3 Anisotropy of Magnetic Susceptibility

(All AMS measurements can be found in Appendix B)

Susceptibility axes for the PdL samples produced a consistent pattern in specimen coordinates (Figure 20), with the axis of minimum susceptibility tightly clustered normal to the measured plane, and the maximum and intermediate axes girdled horizontally around the same plane. This pattern is immediately recognizable as the result of a strongly oblate ellipsoid, a pattern predicted by the dominant magnetic mineralogy (biotite and other phyllosilicates, with contributions from hematite and other ferromagnetic minerals) within the PdL samples. The

Jelinek plot for the samples (Figure 21), displaying the shape factor and fabric intensity of the samples confirms the oblate pattern seen in the specimen coordinate data.

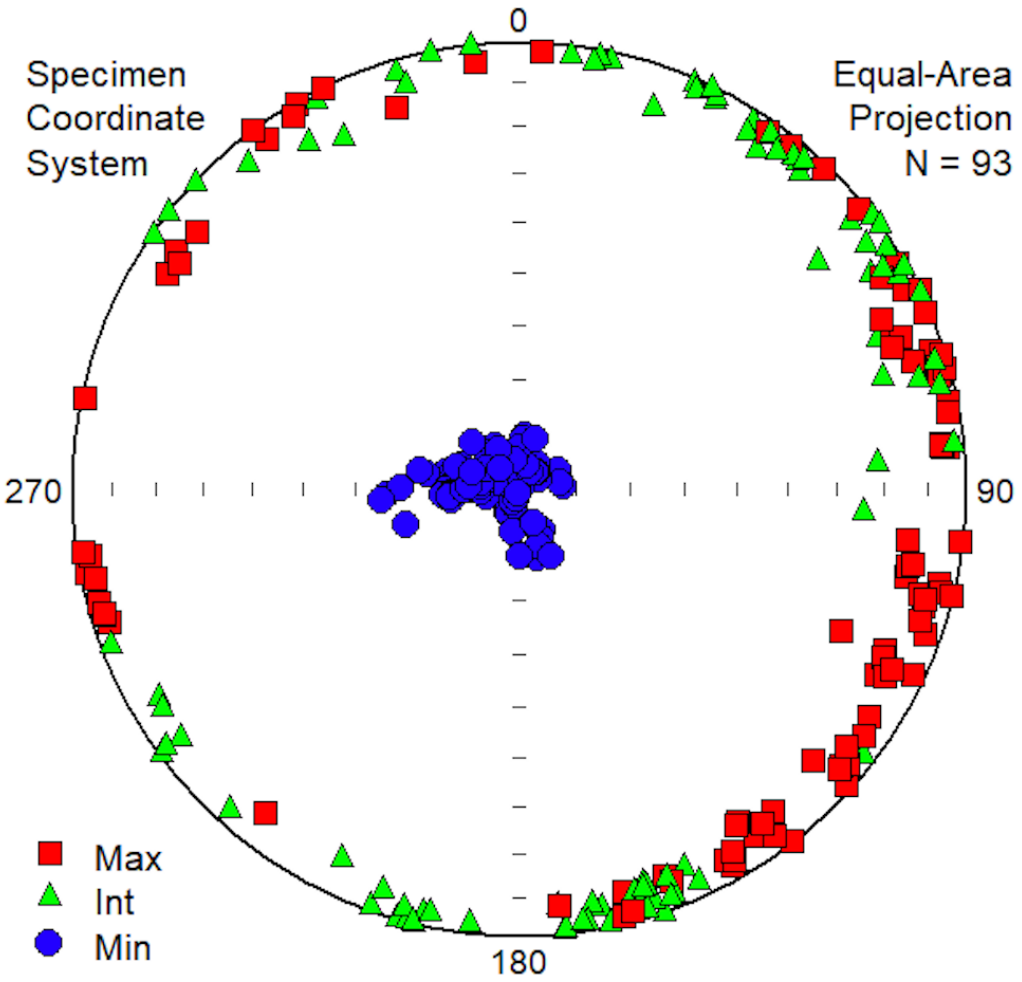

Figure 20: AMS axes orientation data for PdL samples using the specimen coordinate system. Note the clustering of the axis of minimum susceptibility normal to the plane of measurement, and the girdling of the maximum and intermediate axes around the primitive, indicative of a strongly oblate ellipsoid.

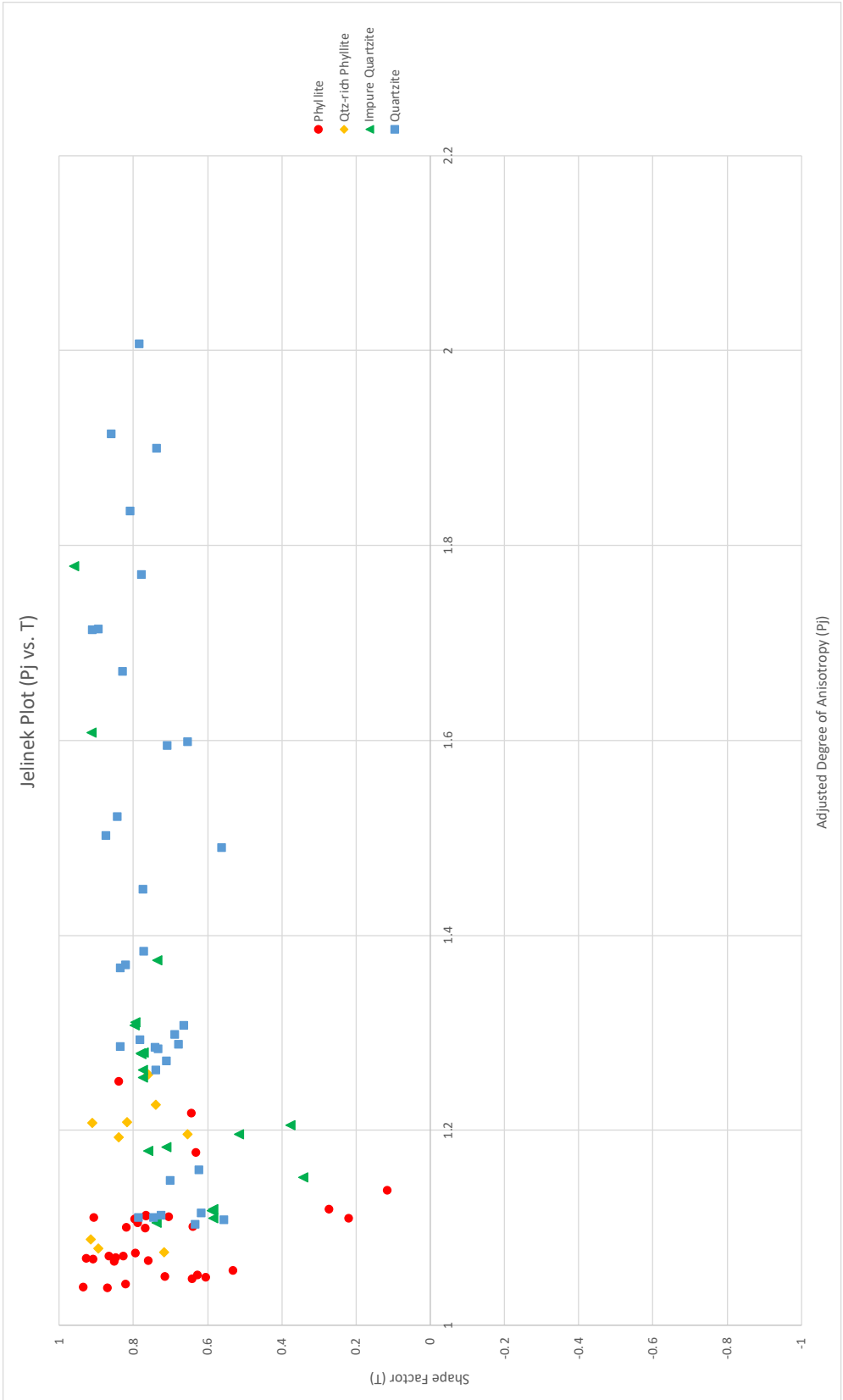

Figure 21: Jelinek plot of AMS axes for the PdL samples. Values of shape parameter (T) between 0 and 1 indicate an oblate ellipsoid, while T values between 0 and -1 result from a prolate shape.

Overall, the PdL samples in geographic coordinates displayed an AMS pattern consistent with field measurements on the samples and throughout the transect (Figures 5, 6, & 12). The minimum axes of anisotropy (K3) were clustered tightly around the pole to the foliation plane measured in the field. The axes of maximum and intermediate anisotropy (K1 and K2, respectively), were girdled along the foliation plane. K1, analogous to the lineations in the samples and along the transect, were spread along the foliation plane from a down-dip direction to lower inclination orientations to the geographic SE.

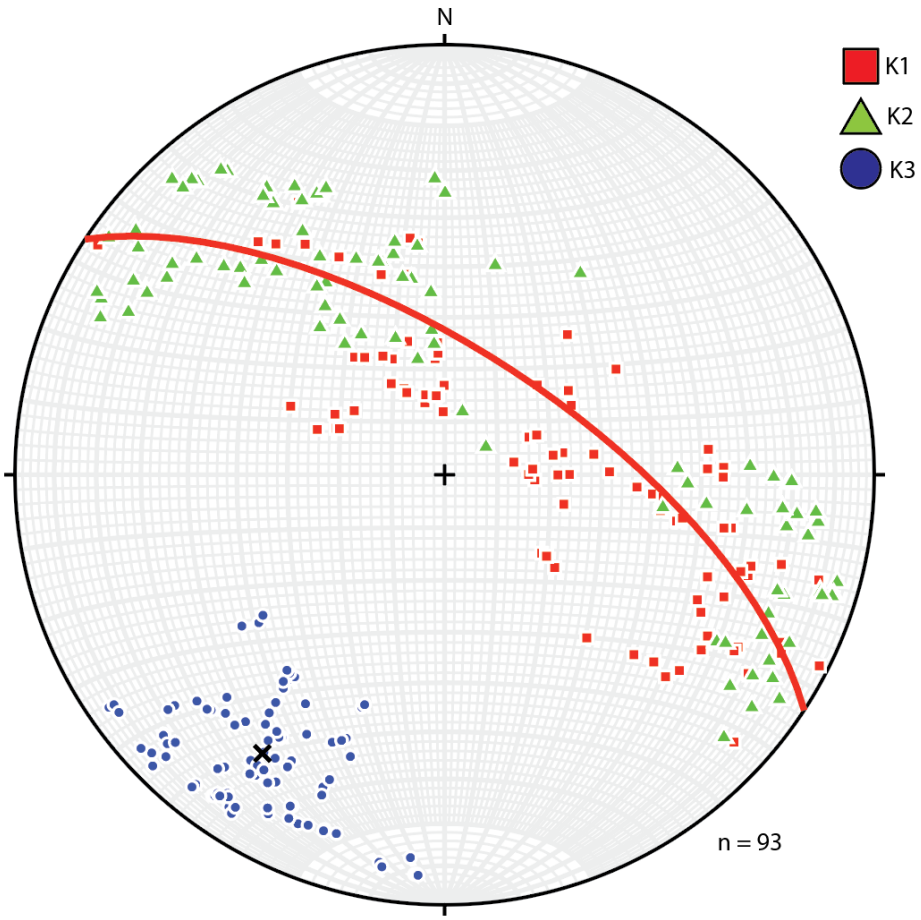

Figure 22: Overall AMS axes orientations (in geographic coordinates) on a lower hemisphere equal area plot for samples from the PdL. K_1 (or K_{max}) is illustrated in red, while K_3 (K_{min}) is in blue. Average foliation plane for the set of samples is displayed using the red great circle, average foliation pole with the black x.

5) Discussion

5.1 Source of Magnetic Susceptibility

In order to properly interpret AMS fabrics, it is important to evaluate which minerals contribute to the magnetic signal and understand how they relate to tectonometamorphic fabrics. The DC demagnetization curves (figure 14) for the samples show only a small proportion of low-coercivity, high susceptibility minerals like detrital titanomagnetite. The DCD curves also show the presence of some high coercivity components, most commonly hematite and goethite, but the low bulk susceptibility for the samples (average K_m = 119 SI^{-6}) highlights the limited impact of any ferromagnetic portion. Given the very low susceptibility and weak hysteresis of the samples it is reasonable to conclude that the grains responsible for the magnetic fabric in the PdL samples are primarily paramagnetic minerals like biotite.

Previous work found that the primary minerals that formed the tectonometamorphic fabrics are biotite and muscovite mica, which form the prominent foliation in all samples and the lineation where evident (Carman, 2020; Kopinski, 2022). Given the metamorphic genesis of biotite in the PdL and the likelihood that the AMS fabric is dominated by this paramagnetic mineral, the interpretation of AMS fabrics as a proxy for tectonic fabrics is reasonable.

5.2 Interpretation of AMS Ellipsoid

Within the PdL samples measured for AMS, the magnetic fabric observed produced a magnetic foliation closely matching the foliation measured in the field, with the K_3 axes clustered around the pole to the plane. Previous AMS research on a similar accretionary tectonic environment (Hajná et al., 2010) showed that with enough deformation, the magnetic

fabric of a rock will closely mirror the tectonic foliation created by thrusting and shortening. Though the PdL and the SISZ as a whole have undergone lateral shearing, more complex than the previous study, the relationship is also observed here. Given the tectonic foliation in the PdL samples is formed from the alignment of biotite crystals in the rocks, and the AMS of paramagnetic minerals is usually determined by the tectonically driven crystallographic orientation of the grains (Borradaile & Henry, 1997; Parés, 2004; Borradaile & Jackson, 2010), it is reasonable to conclude that the magnetic foliation described by AMS measurements and the tectonic foliation of the PdL samples coincide.

The magnetic lineation, identified as the K_1 axis, appears to have formed by deformation also, as evidenced by the comparable lineation orientations identified for each sample in the field (Figure 23). The orientation of magnetic lineations for most of the samples compared very favorably with the visible lineations. The coaxiality between the two sets of measurements along with the strong relationship between magnetic and tectonic foliation indicates that at least some portion of the magnetic fabric of the PdL was tectonically created, as opposed to being wholly dependent on mineralogy or depositional compaction. It is therefore safe to conclude that in terms of orientation, the magnetic and tectonic fabrics are mostly coaxial, formed by the alignment of biotite grains that developed the foliation and lineation during regional deformation. This relationship is not unusual, and it has been identified in many studies of deformed metasedimentary rocks (Parés & Van der Pluijm, 2014; Soto et al., 2009; Weil & Yonkee, 2009).

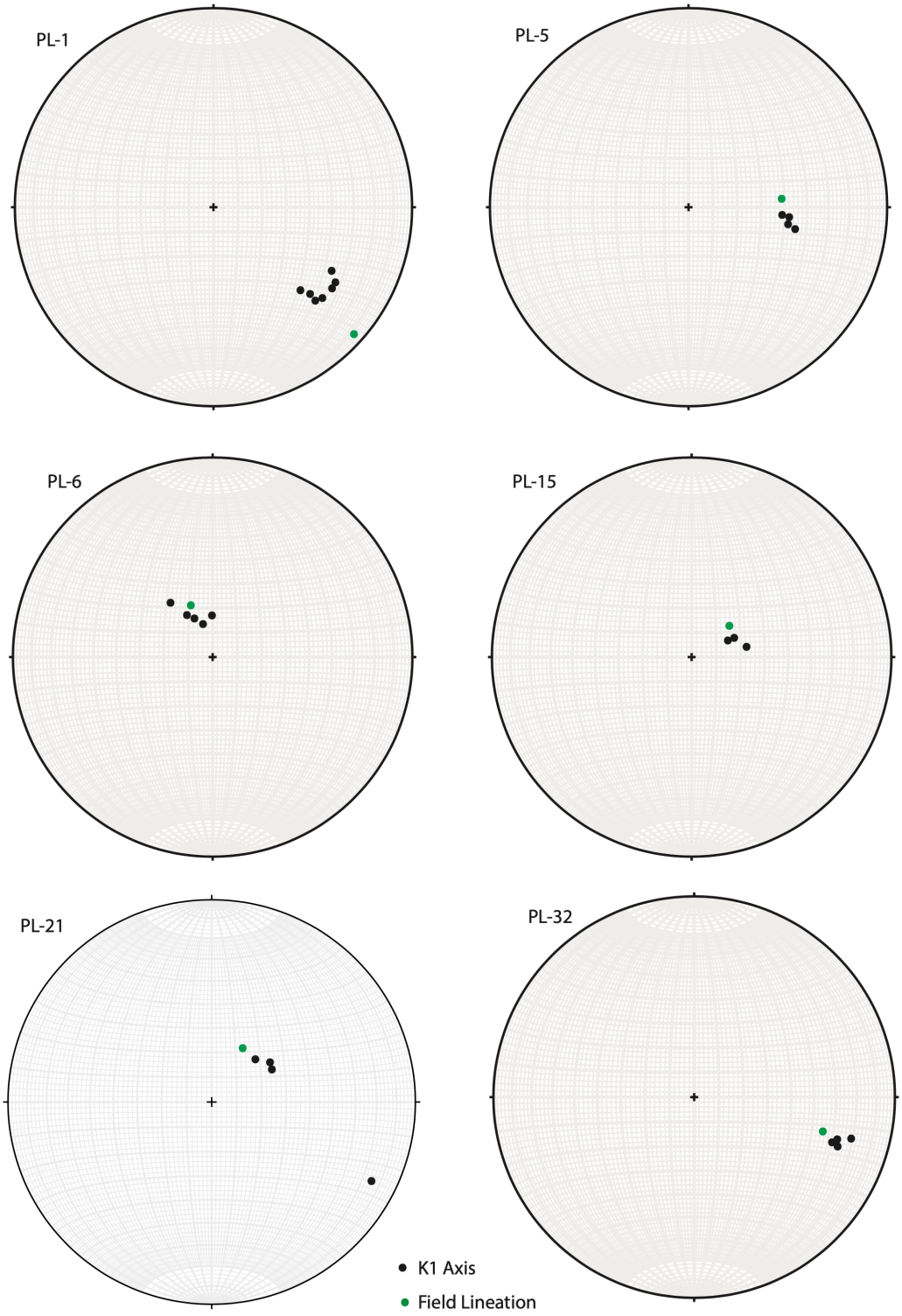

Figure 23: AMS results for selected PdL samples displayed on a lower hemisphere stereographic projection. Axis of maximum susceptibility (K_1) measured for each specimen (multiple specimens per sample) shown with black points, lineation measured in the field colored in green.

Mean susceptibility of the PdL samples was very low as a whole, but patterns do emerge with closer examination, especially when divided into lithologic groups of schist/phyllite (with little or no quartzite), quartz-rich phyllite, impure quartzite, and quartzite. Susceptibility is highest in the phyllite and schist samples, with lower values in the quartz-rich phyllite and the lowest susceptibility in the quartzite beds themselves. Generally speaking, mean susceptibility drops off with the appearance of the quartzite beds after around 20 meters distance from the SISZ (Figure 24), a pattern which makes sense given the diamagnetic properties of quartz grains negatively affecting the overall susceptibility of the samples (Tarling & Hrouda, 1993).

The drop in susceptibility is even more pronounced at distances greater than around 50 meters from the shear zone, a region identified in previous work (Carman, 2020) by a distinct change in geochemistry, with Mg and Mn levels dropping significantly outside of the region most proximal to the SISZ. This geochemical change is believed to be related to syntectonic fluid flow from the BAM. The coincidence between the limit of the proposed hydrothermally-altered zone and the drop in susceptibility may also highlight a decrease in strain outside the boundaries of that zone. More evidence for this is the recrystallized biotite in the designated high strain region closest to the SISZ, which may have been enriched in Fe transported from the BAM as it reformed (Carman, 2020). Another explanation is that increased strain closer to the SISZ facilitated the formation of more secondary ferromagnetic minerals like goethite, which would also raise the overall susceptibility of the rocks within that high strain zone.

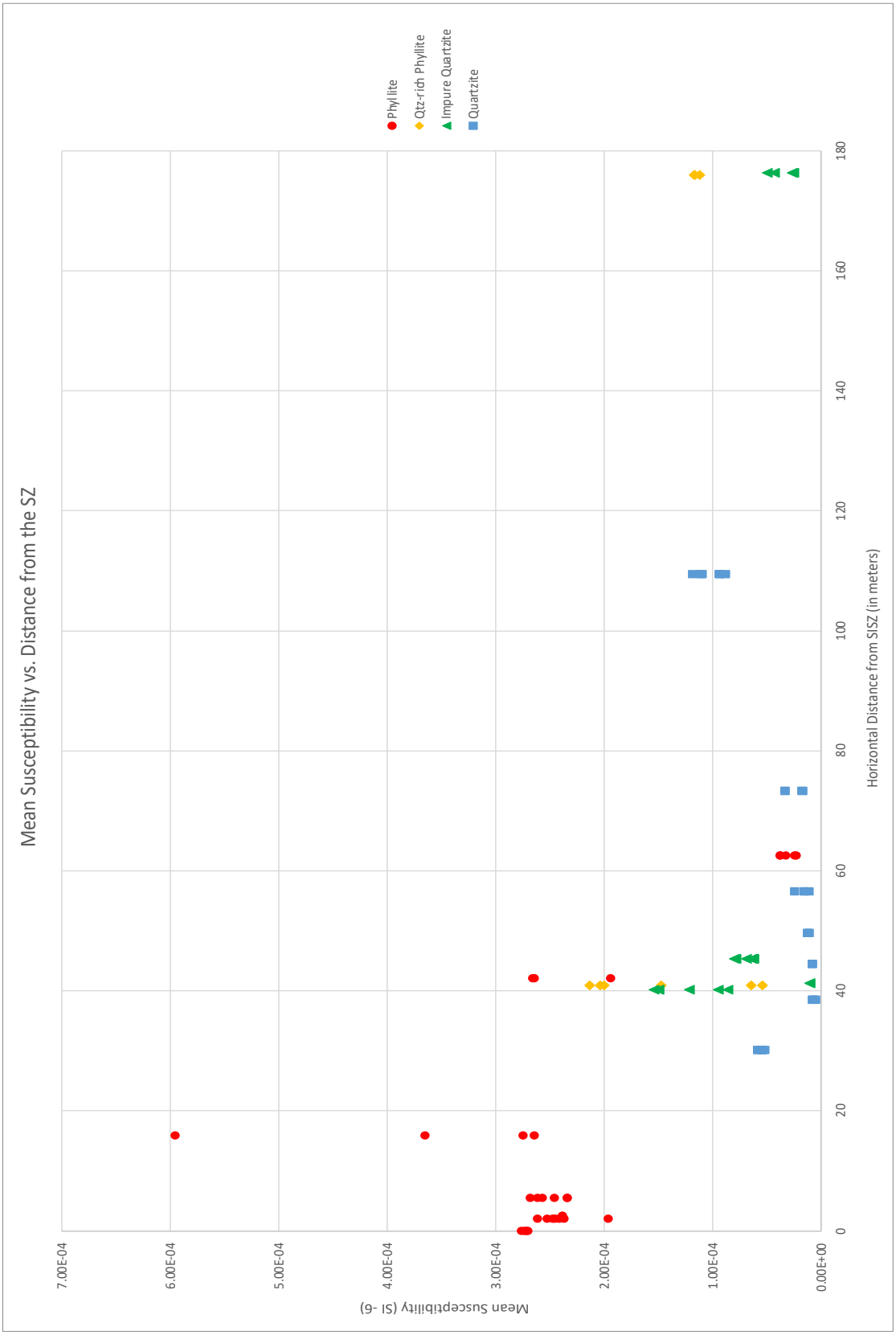

Figure 24: Plot of mean susceptibility of PdL samples (SI^{-6}) against distance from the SISZ (in meters)

Using distance from the shear zone as a normalizing variable helps to identify patterns in shape parameter and degree of anisotropy of the samples (Figures 25 & 26). In terms of shape parameter, the less oblate shape of phyllite sample PL5 directly adjacent to the appearance of quartzite within the formation is easily seen as an outlier. The reason for this is unknown, but the estimated paramagnetic portion of the susceptibility for PL5 was significantly lower than in the other samples from the PdL, which could indicate the less oblate fabric is a result of the greater influence of ferromagnetic minerals within the phyllite. Degree of anisotropy also shows no definitive relationship with distance but is instead strongly controlled by lithology of the samples. The lack of conclusive patterns as a function of distance from the SISZ highlight the complex nature of kinematic partitioning within the PdL and the lack of a clear distinction between D_2 SISZ deformation and the pre-existing D_1 fabric along the Almonaster transect.

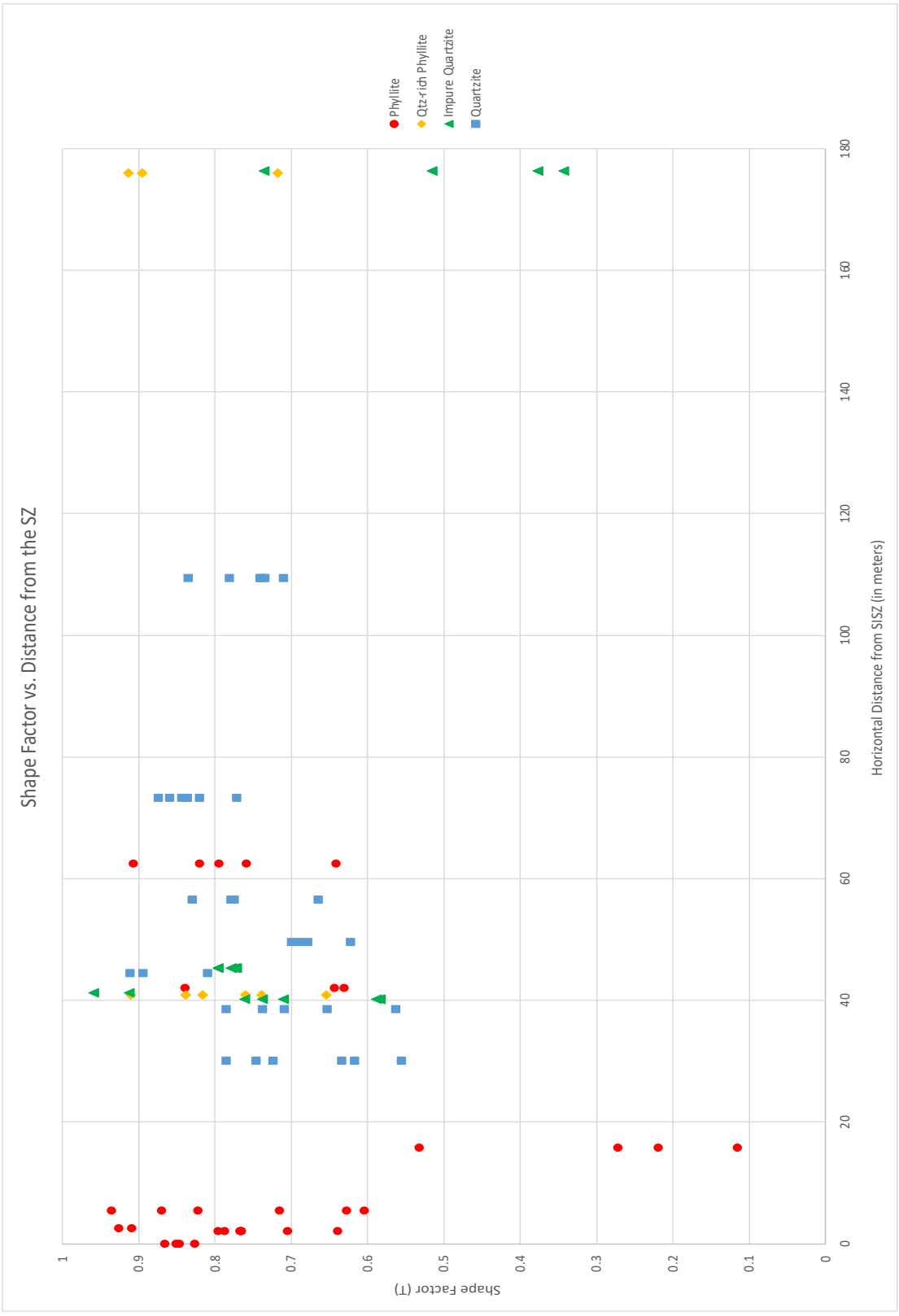

Figure 25: Plot of AMS ellipsoid shape parameter (T) against distance from SISZ (in meters), values between 0 and 1 indicate an oblately shaped ellipsoid

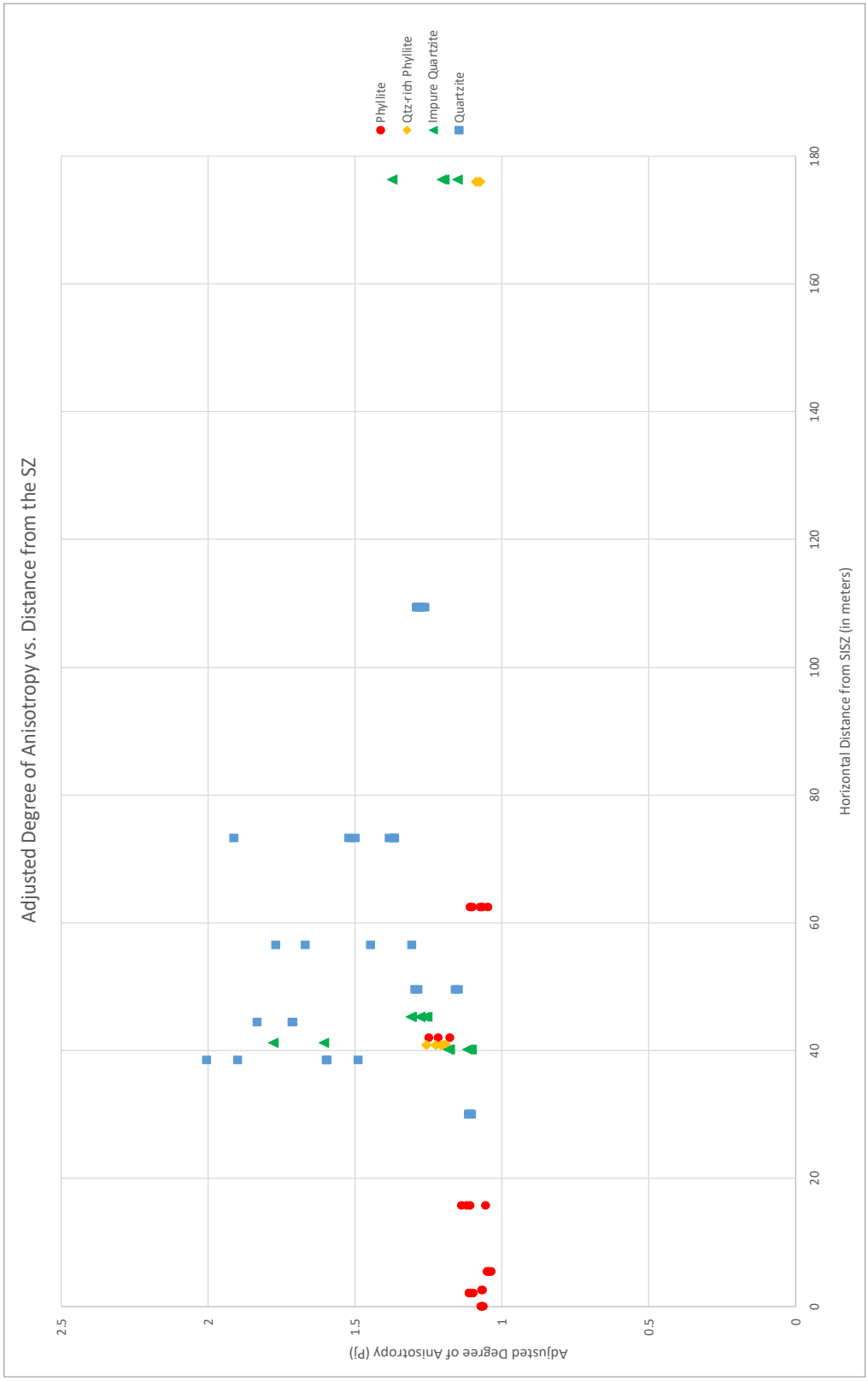

Figure 26: Plot of adjusted degree of anisotropy (Pj), or fabric intensity, versus the distance from the SISZ (in meters). Greater values of Pj are indicative of greater fabric intensity

Examining the shape factor (Figure 27) and degree of anisotropy (Figure 28) compared to mean susceptibility of the samples reveals some conspicuous clustering. Though most samples were oblate to very oblate, some outliers appear in the schist and phyllite, especially the aforementioned phyllite sample PL5, which has the least oblate fabric by far. The higher susceptibility for the PL5 samples provides further evidence for the influence the ferromagnetic fraction has on the shape of the AMS ellipsoid.

Degree of anisotropy for the samples follows similar clustering based primarily on lithology (Figure 28). Interestingly, the samples with the highest measured degree of anisotropy were the quartzite beds, despite the diamagnetic quartz contributing nothing to the magnetic fabric. The range of Pj values for the PdL quartzite beds is relatively high compared to similar AMS studies in micaceous quartzite (Mamtani & Vishnu, 2012), but the variation of factors (kinematics, strain magnitude, lithology) between field areas may be enough to account for the difference. The least anisotropic samples were taken from both the schist/phyllite as well as the quartz-rich phyllite samples. Given the samples with the highest degree of anisotropy are the lowest susceptibility (the “purest” quartzite), it is possible that the more complex fabric (wavy foliation, S/C fabrics) created by the greater amount of biotite in the schist and phyllite has a reducing effect on the degree of anisotropy for the samples, while simultaneously increasing the overall susceptibility. The purest quartzite samples also have the highest proportional paramagnetic influence, estimated at up to 50% in some samples. It seems likely the outsized importance of the paramagnetic fraction in the quartzite combined with the relative decrease in detrital and secondary ferromagnetic minerals also plays a role in the greater degree of anisotropy and lower susceptibility of those samples.

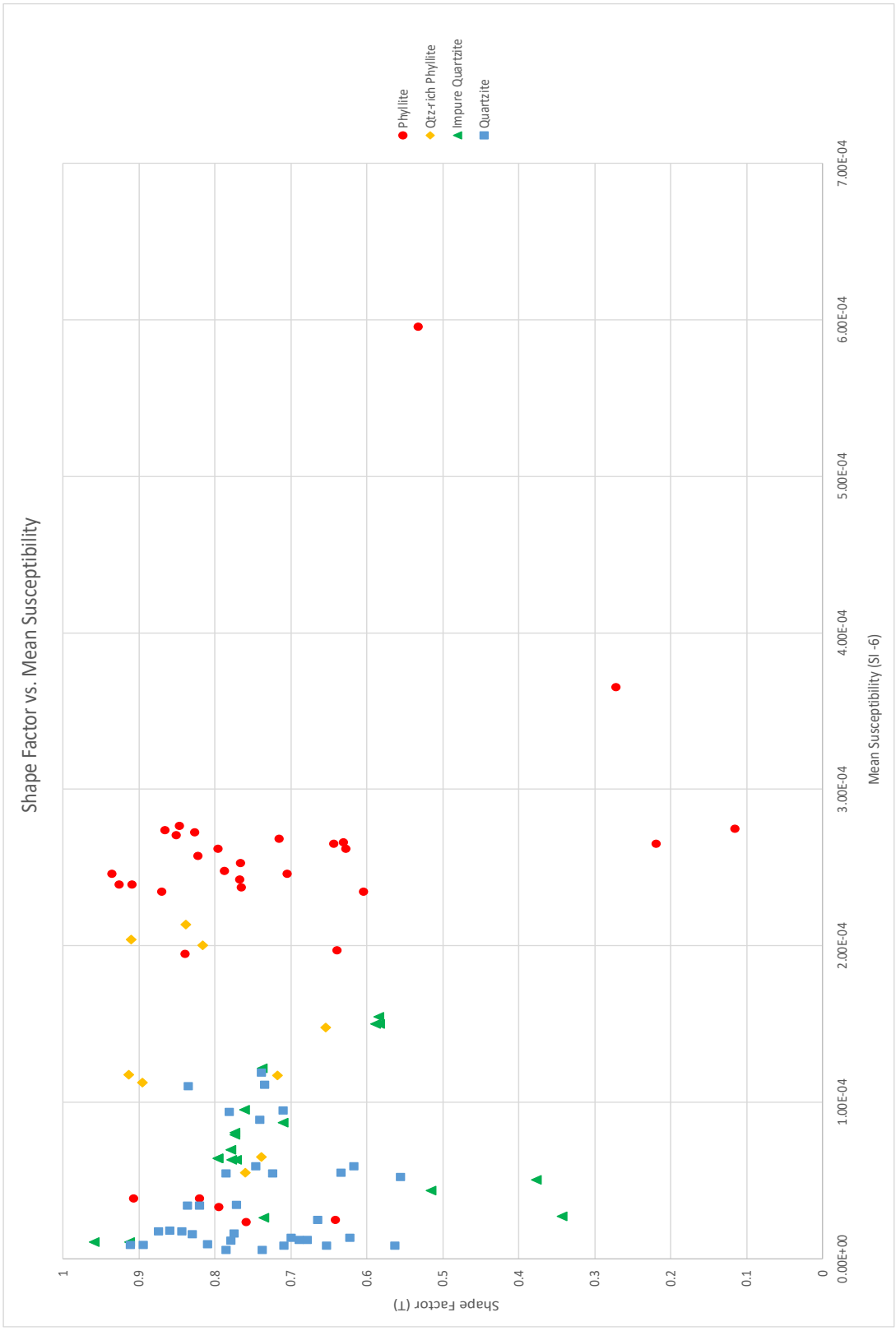

Figure 27: Plot of shape factor (T) of the AMS ellipsoid against mean susceptibility (10^{-6} SI) of the PdL samples. Shape factor values between 0 and 1 represent an oblate ellipsoid (more oblate shape closer to 1).

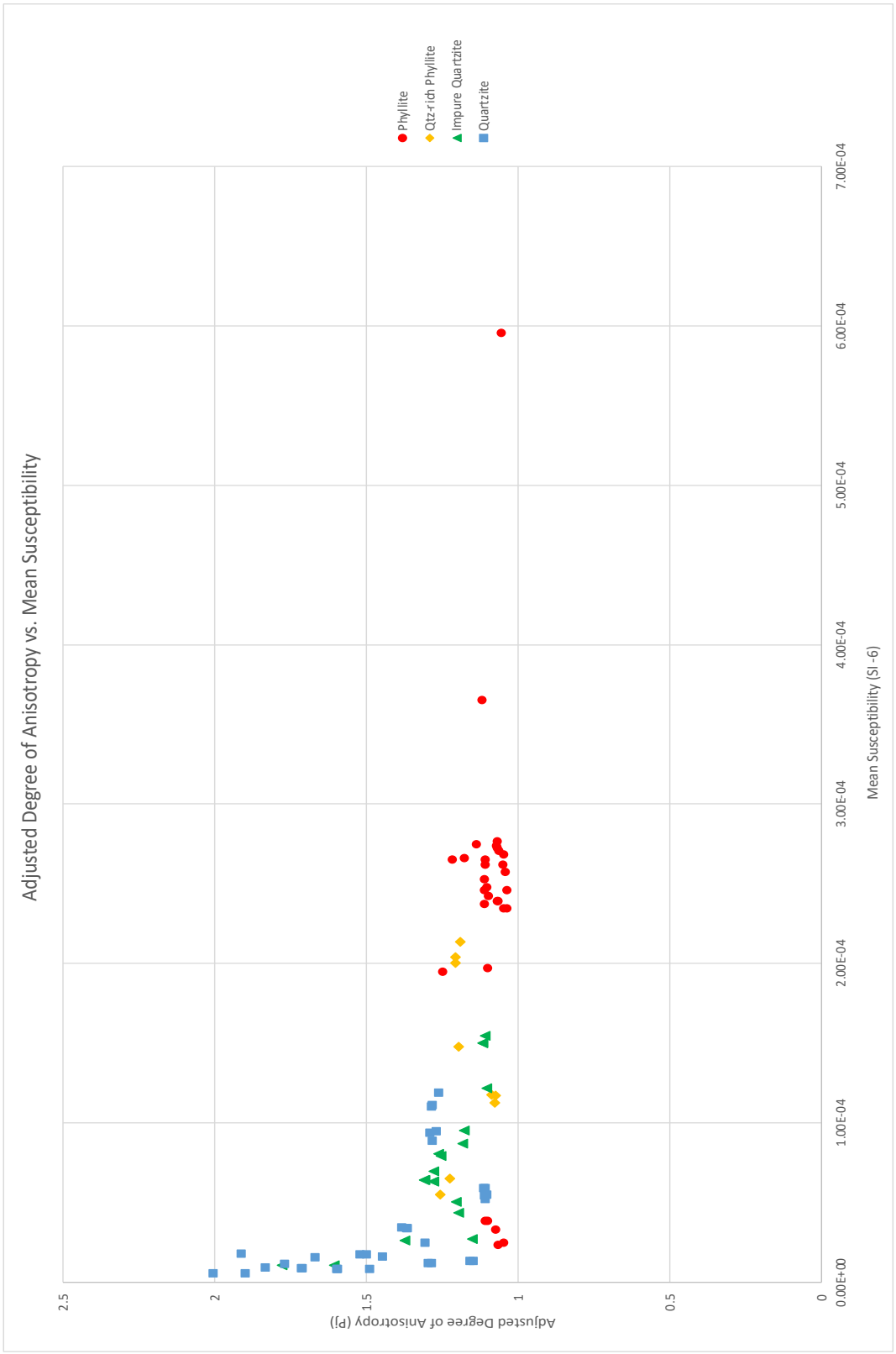

Figure 28: Adjusted degree of anisotropy (Pj) plotted against mean susceptibility (SI^{-6}) for the PdL samples. Higher values of Pj indicate a greater level of anisotropy.

The tendency of the AMS parameter measurements to behave according to lithology combined with the scattered nature of the results as a function of distance lead to the conclusion that despite the orientation of the magnetic lineation being analogous to the tectonic lineation, there is no measured parameter that can conclusively act as a suitable proxy for strain magnitude (Figure 29), though there is almost certainly a relationship between K_{mean} and strain when examined as a function of distance from the SISZ. Despite this, the magnetic lineation is still valuable information, as it allows for a more easily observed lineation for the purpose of strain orientation calculations such as those needed for kinematic modelling (e.g. Fernández et al. 2013) or further analysis of quartz grain CPO/SPO in the quartzite samples (Renjith et al., 2016).

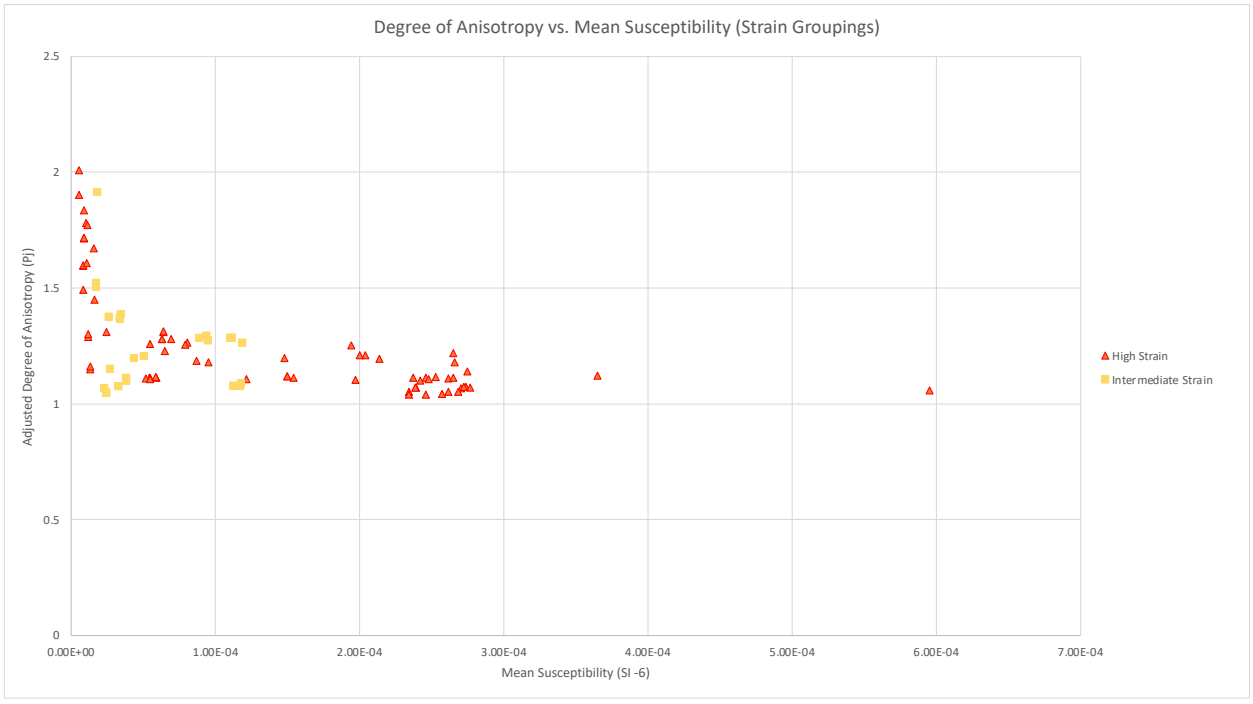

Figure 29: Plot of adjusted degree of anisotropy against mean susceptibility using strain groupings established using microstructural work from Carman (2020)

5.3 Interpretation of Regional Strain Patterns

Using the orientation of the measured magnetic lineation in the PdL, interpretations can be made about the SISZ deformation within the PdL. The SISZ deformation evident on the Beja-Acebuches metabasites (BAM) is likely due to triclinic transpression. Ductile transpression is a combination of pure and simple shear components (Tikoff & Fossen, 1993; Fossen & Tikoff, 1993). Early models of transpression included shear zones with monoclinic symmetries, vertical boundaries, horizontal simple shear (either left or right lateral), and pure shear with vertical extrusion (Tikoff & Fossen, 1993; Fossen & Tikoff, 1993). Subsequent transpression models became more complex. Models began to account for inclined boundaries (Jones et al., 2004), migrating boundary shear zones (Jiang, 2007), oblique simple shear orientations (Lin et al., 1998), variable extrusion directions (e.g., Fernández et al., 2013), and the combined effect of transpression and transtension (Xypolias et al., 2018). Detailed structural observations combined with kinematic modeling can be used to determine the orientations of the shear zone boundaries, simple shear component, and the extrusion direction related to the pure shear component (Fernández et al., 2013; Sarkarinejad et al., 2013).

Detailed structural and kinematic modeling studies on the SISZ deformation within the BAM indicate that the structures are consistent with a triclinic transpression model with shear zone boundaries that strike 115 and dip 50° NE with subhorizontal left-lateral simple shearing and variable, but steep extrusion directions (Díaz-Azpiroz and Fernández, 2005; Fernández et al., 2013). Within the Almonaster transect of the BAM, the extrusion direction (ν) is likely 130-170° (see Fig. 30 and Fernández et al., 2013 for definition of ν and calculation for the BAM).

Kinematics of the SISZ within the PdL is likely different based on structural observations. The SISZ boundaries remain relatively constant, but the lithologies in the PdL and resulting kinematic partitioning render direct comparison difficult. Despite that, the AMS results do show a distinctively oblate fabric, in most cases highly oblate. In cases of simple thrust-dominated deformation, as the PdL is commonly described, the fabric would tend more to the plane strain line (shape parameter T = 0) as opposed to either prolate or oblate. The strongly oblate fabric provides evidence for strong flattening in the PdL, adding a coaxial pure shear component to the deformation that is consistent with existing transpression models (Tikoff & Fossen, 1993).

Despite the similar flattening component between the BAM and the PdL, the simple shearing direction is distinctly different within the PdL. Microstructural work by Carman (2020) highlighted many asymmetric features within the PdL including S-C fabrics, asymmetric folds, and sigmoidal grains that clearly established top to the SW thrust-dominated deformation. Crystallographic vorticity axes (CVA) calculated for quartz grains in samples from the Almonaster transect also highlight the predominance of a thrust component in PdL deformation, though with significant variation in samples exhibiting left-lateral or oblique shear (Kopinski, 2022). It also seems likely that some of the variation in the measured K_1 orientations is related to the strongly oblate fabric, and the pure shear dominated extrusion that goes along with it.

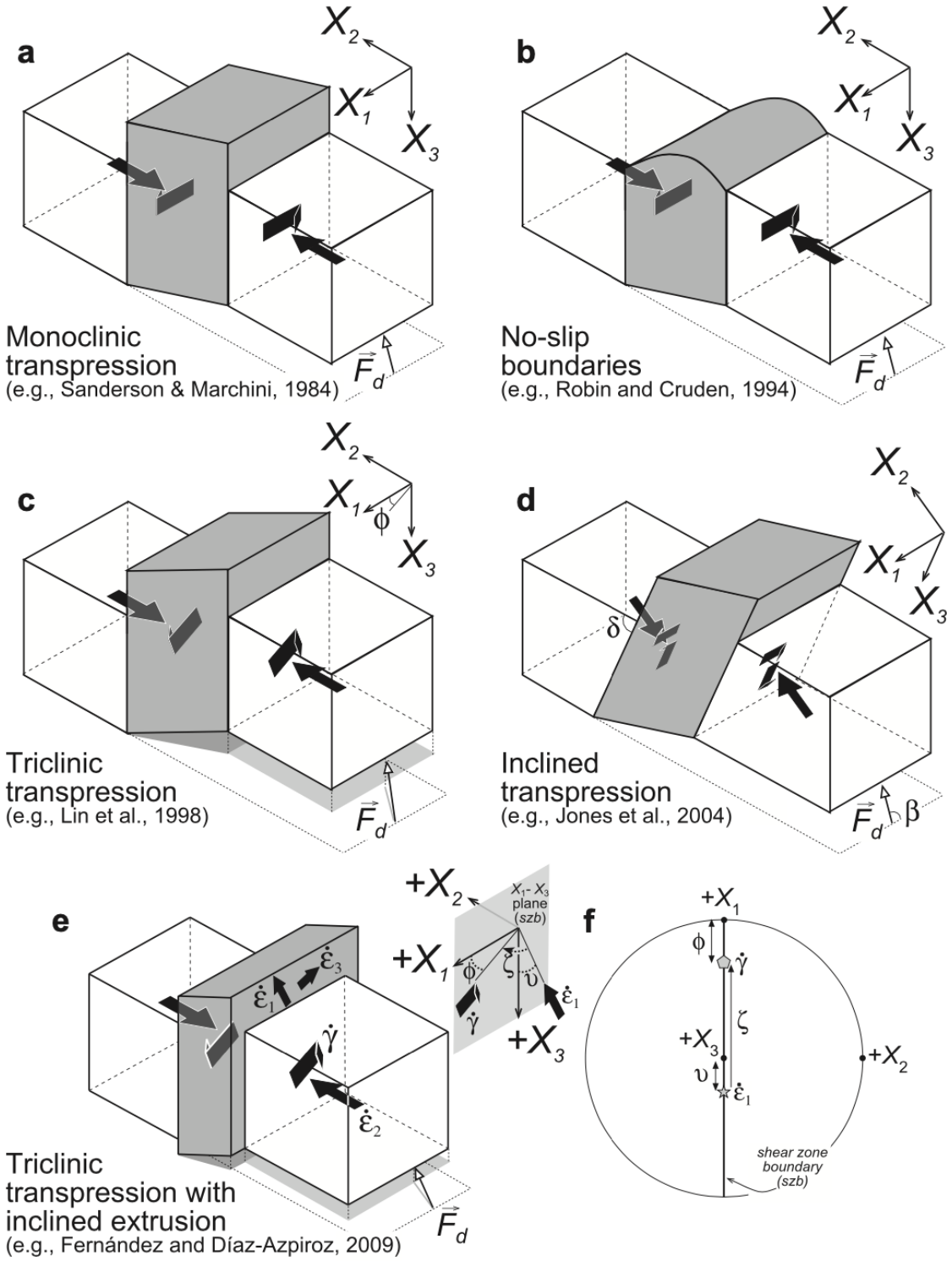

Figure 30: Existing transpression models with a reference frame in which X_1 is parallel to the strike of the shear zone boundary, X_2 is normal to the SZ, and X_3 is vertical. Φ is the angle between the strike of the SZ and the simple shear component, δ is the dip angle of the SZ, β is the angle between the convergence vector (Fd) and the strike of the SZ, υ is the angle between extrusion direction and dip, and ξ is the acute angle between simple shear and extrusion direction. (From Fernández et al., 2013)

The lineations determined by field observations (Figure 12; Appendix A) and the K_1 axes of the AMS ellipsoid (Figure 22; Appendix B) show a range of values from down-dip to subhorizontal orientations. While detailed structural modeling is beyond the scope of this work, a first order approximation of kinematic regime can be made by combining observations of the vertical shear plane in the field (Carman, 2020; Kopinski, 2022) with the lineation orientations.

While there is significant variation in the lineation orientations, the prevalence of down-dip lineations is most easily explained by a thrust-dominated simple shear component which is consistent with the kinematic indicators in the field and some of the CVA analysis results (Kopinski, 2022). The shallowly plunging lineations are possibly explained by a left-lateral simple shear component, indicating that within the PdL there is significant variation in kinematic regime.

The strongly oblate AMS fabric also provides another variable in lineation orientation. The strong flattening in the PdL represents a substantial pure shear component, along with an accompanying variability in extrusion direction. In the less anisotropic samples, the similar magnitude of the K_1 and K_2 axes could also cause their orientation to be somewhat interchangeable, further complicating correlational explanation. In any case, more detailed kinematic modeling is necessary to determine the orientation of the pure shear extrusion direction and the pattern of variation between thrust and left-lateral (and likely oblique) simple shear component, and any lineation orientation likely resulting from the combination of all these factors.

Also interesting to note is the comparison between the BAM side of the SISZ (Figure 4; Díaz-Azpiroz & Fernández, 2005) with the PdL side of the SISZ. The L_2 lineations measured in the BAM along the eastern sector of the SISZ (where the Almonaster transect is located) differ from the lineations in the PdL. While the BAM is dominated by only the lineations that shallowly plunge to the SE, the PdL has these lineations but also a majority that are steeply plunging (down-dip on foliation). This suggests that while the BAM mostly experienced a left-lateral simple shear component, the PdL experienced a thrusting simple shear component, but with some domains of left-lateral or oblique simple shear. This difference can be explained by the thrusting action of the BAM atop the PdL that was partitioned into the PdL.

Although it is important to note that lineation orientation is not entirely controlled by the simple shear component, this change between thrust and simple shear dominated deformation in the PdL is also evident by examining the change in rake of the K_1 lineation within the K_1-K_2 plane moving away from the shear zone (Figure 31). Closer to the SISZ, rake of the K_1 axis, analogous to the plunge of the tectonic lineation, is generally higher, indicating that closer to the shear zone, where deformation is highest, the deformation was dominated by thrusting, while the regional left-lateral simple shear becomes more dominant further away from the SZ, albeit with significant fluctuations. It is important to note however, as previously mentioned, that the lineation orientations are likely the result of some combination of all kinematic factors, the combined influence of various amounts of thrust and left lateral simple shear along with the variable extrusion that accompanies the pure shear flattening component.

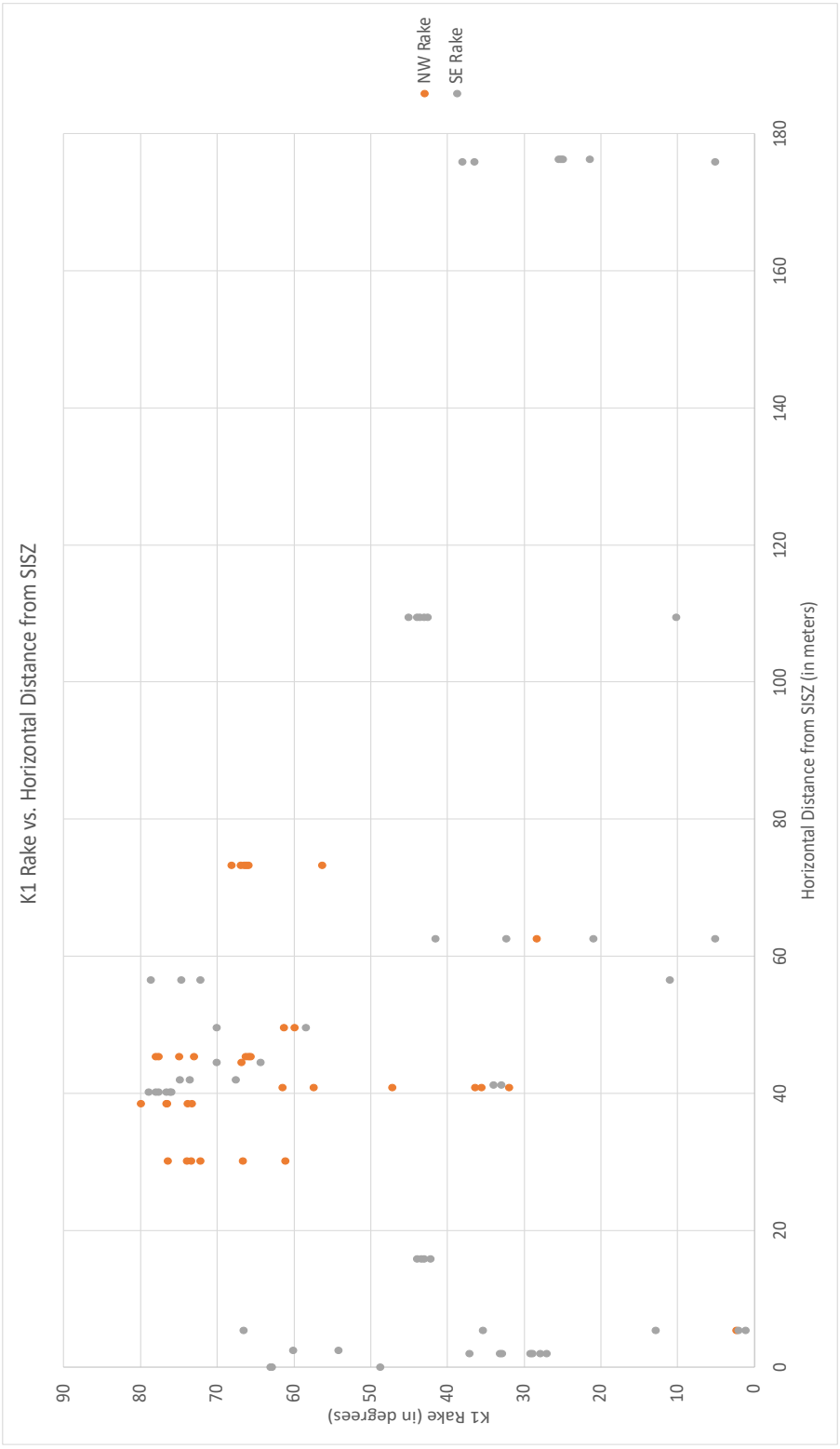

Figure 31: Rake values for the axis of maximum anisotropy (K_1) plotted against distance from the SZ (in meters). Higher values of rake indicate thrust-dominated, down-dip lineations while less inclined measurements are indicative of lateral shear. Both orientations could also result from variable extrusion related to the strong pure shear component evidenced by the oblate AMS fabric.

6) Future Work

Additional work surrounding the magnetic fabric of the PdL includes further refining the magnetic characterization of the PdL samples. Specifically, due to the disconnect between samples collected previously and used for magnetic characterization and samples used for AMS which were collected at a later date, there are several more factors to explore including a closer examination between quartz and mica content and fabric intensity or orientation. To this end, point counting or magnetic characterization (hysteresis, magnetic property exploration, susceptibility measurements) could be performed on the samples that were actually used for AMS research, in order to describe and explain the observed magnetic fabric more accurately.

Additionally, further comparison to the crystallographic preferred orientation (CPO) data could also further inform the observed AMS fabric, especially with regards to how the magnetic lineation aligns along the foliation plane, and the extent to which that alignment is a result of tectonic deformation, mineral orientation, complex interactions between quartz and mica grains within the rocks or some combination of factors (Renjith et al., 2016). The quartz CPO fabric identified by Kopinski (2022) provides a vorticity axis which constrains the orientation of the simple shear component of deformation, combined with the AMS data, a more detailed analysis of the observed lineation orientation can be performed to help further describe deformation partitioning across the PdL.

Along the same lines, additional avenues of magnetic fabric identification, including anisotropy of remanent magnetism studies (AIRM, AARM), could be used to obtain a clearer picture of the magnetic fabric within the PdL. This additional data could strengthen the results obtained from the AMS by highlighting the coaxiality of the different magnetic carriers to the

observed AMS fabric or by isolating the fabric produced by the higher coercivity ferromagnetic components identified in the phyllites closest to the SISZ (Mattson et al., 2021; Parés & Van der Pluijm, 2014; Robustelli Test & Zanella, 2021).

Spatially within the SISZ region, more work can be done using AMS to identify lineation measurements which can be used to describe observed strain along other transects and to fill gaps and increase resolution along the Almonaster transect. Much work has been done on the other side of the SISZ within the BAM, and multiple sectors have been described and interpreted for strain analysis (Díaz-Azpiroz & Fernández, 2005). Even without an obvious AMS parameter to use as a proxy for strain magnitude, valuable information can be obtained from the orientation of the magnetic lineation. Lineation measurements are integral in strain modelling and help to better identify factors related to the transpression experienced by the PdL like variable extrusion or fault block rotation on the SW side of the SISZ. Collecting and comparing magnetic lineation data along the strike of the SISZ could also help identify regional strain partition patterns. This information is invaluable in more clearly understanding the kinematics of the SISZ as whole (Fernández et al., 2013).

7) Conclusions

Until recently, detailed research on the SISZ has primarily been located within the Beja-Acebuches Metabasites side of the shear zone, due to the more consistent deformational and lithologic characteristics. The Pulo do Lobo side has always presented a much greater challenge to researchers due to the variability in lithology and strongly partitioned deformation. Obtaining fabric measurements in the field can be an arduous process, and the interaction between the phyllitic rocks and quartzite beds, along with the results of hydrothermal fluid flow from the BAM present challenges in describing and attempting to quantify deformation around the SISZ. To that end, using magnetic fabrics, which often reflect the more subtle effects of deformation, is a great aid in identifying and describing those effects within the PdL.

Magnetic characterization of the PdL samples highlight the predominantly paramagnetic nature of the samples, especially dominated by the phyllosilicates in the quartz-rich samples, and to a lesser extent in the more lithologically complex and higher strain schists and phyllites. Additional work could be done on further isolating the magnetic carriers, and what part they play in the formation of the AMS fabric identified.

While more data would certainly be useful in delineating the effects of mineral orientation, rather than tectonic deformation on the magnetic fabric, the simple fact that the K_1 magnetic lineation so closely matched stretching lineation measurements obtained in the field allows for the assumption of parallelism between the magnetic and tectonic lineation. This assumption is supported by many previous studies using AMS to describe tectonic deformation (Borradaile & Henry, 1997; Cifelli et al., 2015; Parés & Van der Pluijm, 2003; Robustelli Test & Zanella, 2021; Weil & Yonkee, 2009).

AMS axis orientation measurements collected from the PdL samples showed a definitive and interpretable pattern. The orientations of the axes of minimum anisotropy (K_3) were tightly clustered around the pole to the foliation plane of the samples, the plane along which the oriented cubes were cut for AMS measurement. Axes of greatest anisotropy (K_1) were girdled along the foliation plane, from a cluster of high inclination, down-dip orientations to low inclination, geographically SE oriented measurements. These two endpoints represent stretching lineations that are interpreted to be dominated by thrusting or left-lateral simple shear, respectively.

The shape of the AMS ellipsoid was distinctly oblate, a result which highlights the pure shear component of deformation in the PdL. In a simplified, thrust-dominated kinematic model, the ellipsoid shape would tend to fall on the plane strain line or close to it. The strongly oblate fabric is indicative of the additional influence of coaxial deformation paired with simple shear deformation and is consistent with transpression models and kinematics in similar settings.

Samples had varying degrees of anisotropy with the strongest fabrics present in the quartzite samples, which also had the highest proportion of magnetic susceptibility derived from the paramagnetic component. Phyllite samples closer to the SISZ had weaker levels of anisotropy and higher bulk susceptibilities, highlighting the effect the presence of more detrital and secondary ferromagnetic minerals has on weakening the fabric formed by the alignment of micas. Unfortunately, no clear distinction in degree of anisotropy was observed when samples were grouped by strain, restricting the comparison between anisotropy and strain magnitude.

Using horizontal distance from the SISZ as a variable mostly served to confirm patterns recognized in the lithologic groupings, though a distinct drop in mean susceptibility was

observed at a distance of around 50 meters. This distance is an important area in the PdL, as geochemical data reveals a substantial drop in Mg at that location due to mobilization of elements by hydrothermal fluids. The higher levels of Mg near the SISZ are most likely due to hydrothermal fluid which moved Mg and other elements into the PdL from the MORB-derived BAM. This syntectonic fluid interaction may have allowed for Fe-enrichment of recrystallized biotite and the creation of secondary ferromagnetic minerals like goethite close to the SISZ, reflected in the higher bulk susceptibilities of samples within this hydrothermal zone.

Despite the limitations of the data, the magnetic lineations identified in the PdL samples are still useful for the purposes of describing the kinematics of deformation along the Almonaster transect. Magnetic lineation data showed that deformation in samples closer to the SISZ tended to be more thrust-dominated, with more lateral simple shearing at greater distances from the SISZ. Further complicating things is the flattening component identified in this research which, when combined with the ratio of thrust, sinistral, and oblique simple shear makes assigning cause to a specific orientation difficult. The presence of possible oblique or left-lateral lineations at such great distances from the SISZ also complicates discussion about the limits of D_2 deformation experienced within the PdL, as it appears to have affected rocks along the Almonaster transect much further away and in a more consistent way than previously believed.

Moving forward, more data is necessary to continue to draw conclusions about the PdL side of the SISZ. Among existing samples, more work could be done to classify and differentiate magnetic contributors in order to further analyze the causes of the observed magnetic fabric. Among the PdL, more AMS work could be used to help identify patterns in lineation orientation

moving along the shear zone. A larger dataset would help increase detail and allow for closer consideration of the factors involved in kinematic partitioning in SISZ.

8) References

Anastasio, D. J., Pazzaglia, F. J., Parés, J. M., Kodama, K. P., Berti, C., Fisher, J. A., ... & Carnes, L. K. (2021). Application of anisotropy of magnetic susceptibility (AMS) fabrics to determine the kinematics of active tectonics: examples from the Betic Cordillera, Spain, and the Northern Apennines, Italy. Solid Earth, 12(5), 1125-1142.

Aranguren, A., Cuevas, J. and Tubía, J.M., 1996. Composite magnetic fabrics from SC mylonites. Journal of Structural Geology, 18(7), 863-869.

Aranguren, A., Cuevas, J., Tubia, J.M., Román-Berdiel, T., Casas-Sainz, A. and Casas-Ponsati, A., 2003. Granite laccolith emplacement in the Iberian arc: AMS and gravity study of the La Tojiza pluton (NW Spain). Journal of the Geological Society, 160(3), pp.435-445.

Ayarza, P., Martínez Catalán, J.R., Martínez García, A., Alcalde, J., Andrés, J., Simancas, J.F., Palomeras, I., Martí, D., DeFelipe, I., Juhlin, C. and Carbonell, R., 2021. Evolution of the Iberian Massif as deduced from its crustal thickness and geometry of a mid-crustal (Conrad) discontinuity. Solid Earth, 12(7), pp.1515-1547.

Azor, A., Rubatto, D., Simancas, J.F., González Lodeiro, F., Martínez Poyatos, D., Martín Parra, L.M. and Matas, J., 2008. Rheic Ocean ophiolitic remnants in southern Iberia questioned by SHRIMP U-Pb zircon ages on the Beja-Acebuches amphibolites. Tectonics, 27(5).

Borradaile, G. J. 1988. Magnetic susceptibility, petrofabrics and strain. Tectonophysics, 156(1-2), 1-20.

Borradaile, G. J., & Henry, B. 1997. Tectonic applications of magnetic susceptibility and its anisotropy. Earth-Science Reviews, 42(1-2), 49-93.

Borradaile, G.J. and Jackson, M., 2010. Structural geology, petrofabrics and magnetic fabrics (AMS, AARM, AIRM). Journal of Structural Geology, 32(10), pp.1519-1551.

Braid, J.A., Murphy, J.B., Quesada, C. and Mortensen, J., 2011. Tectonic escape of a crustal fragment during the closure of the Rheic Ocean: U–Pb detrital zircon data from the Late Palaeozoic Pulo do Lobo and South Portuguese zones, southern Iberia. Journal of the Geological Society, 168(2), 383-392.

Burton-Johnson, A., Macpherson, C. G., Muraszko, J. R., Harrison, R. J., & Jordan, T. A. 2019. Tectonic strain recorded by magnetic fabrics (AMS) in plutons, including Mt Kinabalu, Borneo: A tool to explore past tectonic regimes and syn-magmatic deformation. Journal of Structural Geology, 119, 50-60.

Carman, N., 2020. Analyzing strain localization, kinematic partitioning and fluid flow in the Pulo do Lobo metasedimentary rocks along the Southern Iberian shear zone, Andalucia, Spain. MS Thesis. University of Wisconsin-Milwaukee, 133 pages.

Carreras, J., Czeck, D. M., Druguet, E., & Hudleston, P. J. 2010. Structure and development of an anastomosing network of ductile shear zones. Journal of Structural Geology, 32(5), 656-666.

Catalán, J.M., Arenas, R., García, F.D., Cuadra, P.G., Gómez-Barreiro, J., Abati, J., Castiñeiras, P., Fernández-Suárez, J., Martínez, S.S., Andonaegui, P. and Clavijo, E.G., 2007. Space and time in the tectonic evolution of the northwestern Iberian Massif: Implications for the Variscan belt. In 4-D framework of continental crust. Geological Society of America Memoir Boulder, Colorado, 200, 403-423.

Cifelli, F., Ballato, P., Alimohammadian, H., Sabouri, J., & Mattei, M. 2015. Tectonic magnetic lineation and oroclinal bending of the Alborz range: Implications on the Iran-Southern Caspian geodynamics. Tectonics, 34(1), 116-132.

Crespo-Blanc, A. and Orozco, M. 1988. The Southern Iberian Shear Zone: a major boundary in the Hercynian folded belt, Tectonophysics, 148, 221–227.

Czeck, D., Kopinski, K., Levang, D., Díaz-Azpiroz, M., Fernández, C., & Michels, Z. 2022. Multiscale strain partitioning in the Pulo do Lobo metasedimentary rocks affected by the Southern Iberian Shear Zone, Southwestern Spain: Geological Society of America Abstracts with Programs, v. 54, no. 5, https://doi.org/10.1130/abs/2022AM-383453.

Dahn, D.R., Braid, J.A., Murphy, J.B., Quesada, C., Dupuis, N. and McFarlane, C.R., 2014. Geochemistry of the Peramora Mélange and Pulo do Lobo schist: geochemical investigation and tectonic interpretation of mafic mélange in the Pangean suture zone, Southern Iberia. International Journal of Earth Sciences, 103(5), 1415-1431.

Dallmeyer, R.D. and Garcia, E.M. eds., 2012. Pre-mesozoic geology of Iberia.

Díaz-Azpiroz, M., & Fernández, C. 2003. Characterization of tectono-metamorphic events using crystal size distribution (CSD) diagrams. A case study from the Acebuches metabasites (SW Spain). Journal of Structural Geology, 25(6), 935-947.

Díaz-Azpiroz, M., Castro, A., Fernández, C., López, S., Caliani, J.F. and Moreno-Ventas, I., 2004. The contact between the Ossa Morena and the South Portuguese zones. Characteristics and significance of the Aracena metamorphic belt, in its central sector between Aroche and Aracena (Huelva). Journal of Iberian Geology, 30, 23-51.

Díaz-Azpiroz, M., Fernández, C., 2005. Kinematic analysis of the southern Iberian shear zone and tectonic evolution of the Acebuches metabasites (SW Variscan Iberian Massif). Tectonics 24, 1–19. doi: 10.1029/2004TC001682.

Díaz-Azpiroz, M. and Fernández, C., 2021. The Southern Iberian Shear Zone (SW Spain): Inclined transpression related to Variscan oblique convergence in a HT/LP metamorphic belt. In Structural Geology and Tectonics Field Guidebook—Volume 1. 137-166. Springer, Cham.

Fernández, C., Czeck, D.M. and Díaz-Azpiroz, M., 2013. Testing the model of oblique transpression with oblique extrusion in two natural cases: Steps and consequences. Journal of Structural Geology, 54, 85-102.

Ferré, E.C., Teyssier, C., Jackson, M., Thill, J.W. and Rainey, E.S., 2003. Magnetic susceptibility anisotropy: a new petrofabric tool in migmatites. Journal of Geophysical Research: Solid Earth, 108(B2).

Fossen, H. and Tikoff, B., 1993. The deformation matrix for simultaneous simple shearing, pure shearing and volume change, and its application to transpression-transtension tectonics. Journal of Structural Geology, 15(3-5), pp.413-422.

Fossen, H. and Tikoff, B., 1998. Extended models of transpression and transtension, and application to tectonic settings. Geological Society, London, Special Publications, 135(1), pp.15-33.

Glen, J.M., Renne, P.R., Milner, S.C. and Coe, R.S., 1997. Magma flow inferred from anisotropy of magnetic susceptibility in the coastal Parana-Etendeka igneous province: Evidence for rifting before flood volcanism. Geology, 25(12), pp.1131-1134.

Graham, J. W. 1966. Significance of magnetic Anisotropy in Appalachian Sedimentary rocks, in The Earth Beneath the Continents. Geophysical Monograph Series 10, eds S. Steinhart and T. J. Smith (Washington, DC: American Geophysical Union), 627–648.

Hajná, J., Žák, J., Kachlík, V. and Chadima, M., 2010. Subduction-driven shortening and differential exhumation in a Cadomian accretionary wedge: the Teplá–Barrandian unit, Bohemian Massif. Precambrian Research, 176(1-4), pp.27-45.

Hillhouse, J.W. and Wells, R.E., 1991. Magnetic fabric, flow directions, and source area of the lower Miocene Peach Springs Tuff in Arizona, California, and Nevada. Journal of Geophysical Research: Solid Earth, 96(B7), pp.12443-12460.

Hrouda, F. 1982. Magnetic anisotropy of rocks and its application in geology and geophysics. Geophysical surveys, 5(1), 37-82.

Hunt, C. P., Moskowitz, B. M., & Banerjee, S. K. 1995. Magnetic properties of rocks and minerals. Rock physics and phase relations: A handbook of physical constants, 3, 189-204.

Jackson, M. & Tauxe, L. 1991. Anisotropy of magnetic susceptibility and remanence: developments in the characterization of tectonic, sedimentary, and igneous fabric. Rev. Geophys, 29, 371-376.

Jackson, M. and Solheid, P., 2010. On the quantitative analysis and evaluation of magnetic hysteresis data. Geochemistry, Geophysics, Geosystems, 11(4).

Jackson, M. J., & Moskowitz, B. 2021. On the distribution of Verwey transition temperatures in natural magnetites. Geophysical Journal International, 224(2), 1314-1325.

Jelínek, V. 1977. The statistical theory of measuring anisotropy of magnetic susceptibility of rocks and its application (Vol. 29, pp. 1-87). Brno, Czech Republic: Geofyzika.

Jiang, D., 2007. Sustainable transpression: an examination of strain and kinematics in deforming zones with migrating boundaries. Journal of structural Geology, 29(12), pp.1984-2005.

Jones, R.R., Holdsworth, R.E., Clegg, P., McCaffrey, K. and Tavarnelli, E., 2004. Inclined transpression. Journal of Structural Geology, 26(8), pp.1531-1548.

Kontny, A., Engelmann, R., Grimmer, J. C., Greiling, R. O., Hirt, A., 2012. Magnetic fabric development in a highly anisotropic magnetite-bearing ductile shear zone (Seve Nappe Complex, Scandinavian Caledonides). International Journal for Earth Science (Geol Rundsch) 101, 671-692. DOI 10.1007/s00531-011-0713-8

Kopinski, K. 2022. Unraveling factors that control strain partitioning in metasedimentary rocks along the Southern Iberian Shear Zone. MS Thesis. University of Wisconsin-Milwaukee

Lin, S., Jiang, D. and Williams, P.F., 1998. Transpression (or transtension) zones of triclinic symmetry: natural example and theoretical modelling. Geological Society, London, Special Publications, 135(1), pp.41-57.

Liu, C., Wang, W., & Deng, C. 2020. A new weathering indicator from high-temperature magnetic susceptibility measurements in an Argon atmosphere. Geophysical Journal International, 221(3), 2010-2025.

Mamtani, M.A. and Vishnu, C.S., 2012. Does AMS data from micaceous quartzite provide information about shape of the strain ellipsoid? International Journal of Earth Sciences, 101(3), pp.693-703.

Mattsson, T., Petri, B., Almqvist, B., McCarthy, W., Burchardt, S., Palma, J.O., Hammer, Ø. and Galland, O. 2021. Decrypting magnetic fabrics (AMS, AARM, AIRM) through the analysis of mineral shape fabrics and distribution anisotropy. Journal of Geophysical Research: Solid Earth, 126(6).

Maxbauer, D. P., Feinberg, J. M., & Fox, D. L. 2016. MAX UnMix: A web application for unmixing magnetic coercivity distributions. Computers & Geosciences, 95, 140-145.

Moreno, C. 1993. Postvolcanic Paleozoic of the Iberian pyrite belt; an example of basin morphologic control on sediment distribution in a turbidite basin. Journal of Sedimentary Research, 63(6), 1118-1128.

Muxworthy, A.R., King, J.G. and Heslop, D., 2005. Assessing the ability of first-order reversal curve (FORC) diagrams to unravel complex magnetic signals. Journal of Geophysical Research: Solid Earth, 110(B1).

Néel, L. 1949. Théorie du traînage magnétique des ferromagnétiques en grains fins avec applications aux terres cuites. Ann. géophys., 5, 99-136.

Nevitt, J.M., Pollard, D.D. and Warren, J.M., 2014. Evaluation of transtension and transpression within contractional fault steps: Comparing kinematic and mechanical models to field data. Journal of Structural Geology, 60, pp.55-69.

Nye, J. F. 1957. The Physical Properties of Crystals. Oxford: Clarendon Press.

Oliveira, J.T., 1990. Stratigraphy and synsedimentary tectonism. In Pre-mesozoic geology of Iberia. 334-347. Springer, Berlin, Heidelberg.

Onézime, J., Charvet, J., Faure, M., Bourdier, J. L., & Chauvet, A. 2003. A new geodynamic interpretation for the South Portuguese Zone (SW Iberia) and the Iberian Pyrite Belt genesis. Tectonics, 22(4).

Parés, J.M. and Van Der Pluijm, B.A., 2002. Evaluating magnetic lineations (AMS) in deformed rocks. Tectonophysics, 350(4), pp.283-298.

Parés, J. M., & Van Der Pluijm, B. A. 2003. Magnetic fabrics and strain in pencil structures of the Knobs Formation, Valley and Ridge Province, US Appalachians. Journal of structural geology, 25(9), 1349-1358.

Parés, J.M., 2004. How deformed are weakly deformed mudrocks? Insights from magnetic anisotropy. Geological Society, London, Special Publications, 238(1), pp.191-203.

Parés, J. M., & van der Pluijm, B. A. 2014. Low-temperature AMS and the quantification of subfabrics in deformed rocks. Tectonophysics, 629, 55-62.

Pereira, M.F., Chichorro, M., Silva, J.B., Ordóñez-Casado, B., Lee, J.K. and Williams, I.S., 2012. Early carboniferous wrenching, exhumation of high-grade metamorphic rocks and basin instability in SW Iberia: Constraints derived from structural geology and U–Pb and 40Ar–39Ar geochronology. Tectonophysics, 558, 28-44.

Pérez-Cáceres, I., Simancas, J.F., Martínez Poyatos, D., Azor, A. and González Lodeiro, F., 2016. Oblique collision and deformation partitioning in the SW Iberian Variscides. Solid Earth, 7(3), 857-872.

Pérez-Cáceres, I., Martínez Poyatos, D.J., Vidal, O., Beyssac, O., Nieto, F., Simancas, J.F., Azor, A. and Bourdelle, F., 2020. Deciphering the metamorphic evolution of the Pulo do Lobo metasedimentary domain (SW Iberian Variscides). Solid Earth, 11(2), 469-488.

Quesada, C., Fonseca, P., Munhá, J., Oliveira, J.T., Ribeiro, A., 1994. The Beja-Acebuches Ophiolite (Southern Iberia Variscan Fold Belt): geological characterization and geodynamic significance. Boletín Geológico Minero 105, 3–49.

Quesada, C., 2006. The Ossa-Morena Zone of the Iberian Massif: a tectonostratigraphic approach to its evolution. Zeitschrift der Deutschen Gesellschaft für Geowissenschaften, 585-595.

Renjith, A.R., Mamtani, M.A. and Urai, J.L., 2016. Fabric analysis of quartzites with negative magnetic susceptibility–Does AMS provide information of SPO or CPO of quartz?. Journal of Structural Geology, 82, pp.48-59.

Roberts, A. P., Cui, Y., & Verosub, K. L. 1995. Wasp-waisted hysteresis loops: Mineral magnetic characteristics and discrimination of components in mixed magnetic systems. Journal of Geophysical Research: Solid Earth, 100(B9), 17909-17924.

Robustelli Test, C. and Zanella, E., 2021. Rock magnetic signature of heterogeneities across an intraplate basal contact: An example from the Northern Apennines. Geochemistry, Geophysics, Geosystems, 22(12).

Sarkarinejad, K., Partabian, A. and Faghih, A., 2013. Variations in the kinematics of deformation along the Zagros inclined transpression zone, Iran: implications for defining a curved inclined transpression zone. Journal of Structural Geology, 48, pp.126-136.

Simancas, J.F., Carbonell, R., González Lodeiro, F., Pérez Estaún, A., Juhlin, C., Ayarza, P., Kashubin, A., Azor, A., Martínez Poyatos, D., Almodovar, G.R. and Pascual, E., 2003. Crustal structure of the transpressional Variscan orogen of SW Iberia: SW Iberia deep seismic reflection profile (IBERSEIS). Tectonics, 22(6).

Smirnov, A. V. 2009. Grain size dependence of low-temperature remanent magnetization in natural and synthetic magnetite: Experimental study. Earth, planets and space, 61(1), 119-124.

Soto, R., Larrasoaña, J. C., Arlegui, L. E., Beamud, E., Oliva-Urcia, B., & Simón, J. L. 2009. Reliability of magnetic fabric of weakly deformed mudrocks as a palaeostress indicator in compressive settings. Journal of Structural Geology, 31(5), 512-522.

Stephenson, S. I., 2018. Characterizing the geochemical changes across a strain gradient in the Beja-Acebuches metabasites due to retrograde metamorphism and fluid flow along the Southern Iberian Shear Zone. MS Thesis. University of Wisconsin-Milwaukee, 112 pages.

Tarling, D. and Hrouda, F. eds., 1993. Magnetic anisotropy of rocks. Springer Science & Business Media.

Tikoff, B. and Fossen, H., 1993. Simultaneous pure and simple shear: the unifying deformation matrix. Tectonophysics, 217(3-4), pp.267-283.

Venäläinen, A., 2018. Modification of bare and functionalized Au (111) surfaces and ferromagnetism of Au and Pd nanoclusters.

Walz, F., 2002. The Verwey transition-a topical review. Journal of Physics: Condensed Matter, 14(12), p.R285.

Weil, A.B. and Yonkee, A., 2009. Anisotropy of magnetic susceptibility in weakly deformed red beds from the Wyoming salient, Sevier thrust belt: Relations to layer-parallel shortening and orogenic curvature. Lithosphere, 1(4), pp.235-256.

Xypolias, P., Gerogiannis, N., Chatzaras, V., Papapavlou, K., Kruckenberg, S.C., Aravadinou, E. and Michels, Z., 2018. Using incremental elongation and shearing to unravel the kinematics of a complex transpressional zone. Journal of Structural Geology, 115, pp.64-81.

Zhang, B., Zhang, J. and Zhong, D., 2010. Structure, kinematics and ages of transpression during strain-partitioning in the Chongshan shear zone, western Yunnan, China. Journal of Structural Geology, 32(4), pp.445-463.

9) Appendices

APPENDIX A: Pulo do Lobo Field Measurement Data

Sample	D (m)	Foliation			Lineation		L Qual. (1-3)
		Strike	Dip	Dip Quad.	Plunge dir.	Plunge	
PL21-0	0.0	142	71	NE	E	low	2
PL21-1	2.0	134	74	NE	132	5	2
PL21-2	2.5	120	62	NE	115	9	2
PL21-3	3.5	128	67	NE	103	45	3
PL21-4	5.4	124	57	NE			
PL21-5A	15.8	132	73	NE	100	60	2
PL21-5B	15.8	134	59	NE	85	51	3
PL21-6	30.1	130	79	NE	337	67	2
PL21-7	31.9	124	82	NE			
PL21-8	32.8	135	62	NE			
PL21-9	33.3	137	70	NE	18	68	2
PL21-10	37.1	105	76	NE	344	74	2
PL21-11	38.5	118	75	NE			
PL21-12	40.2	137	65	NE			
PL21-13	40.8	125	60	NE	347	55	2
PL21-14	41.2	118	65	NE			
PL21-15	42.0	110	73	NE	50	70	2
PL21-16	44.5	110	72	NE	350	69	2
PL21-17	45.3	108	70	NE			
PL21-18	46.2	140	85	NE	345	79	1
PL21-19	49.6	105	50	NE	15	50	2
PL21-20	51.9	127	70	NE			
PL21-21	56.5	120	65	NE	30	65	1
PL21-22	56.8	115	85	NE	340	83	1
PL21-23	62.5	124	64	NE	105	34	2
PL21-24	63.3	120	73	NE	306	19	2
PL21-25	73.3	95	70	NE			
PL21-26	73.5	110	60	NE			
PL21-27	91.8	125	90	NE	125	80	1
PL21-28	92.0	122	73	NE			
PL21-29	109.4	127	42	NE			
PL21-30	110.1	137	40	NE			
PL21-31	175.9	132	40	NE			
PL21-32	176.3	122	52	NE	116	8	1

APPENDIX B – Pulo do Lobo AMS Measurement Data

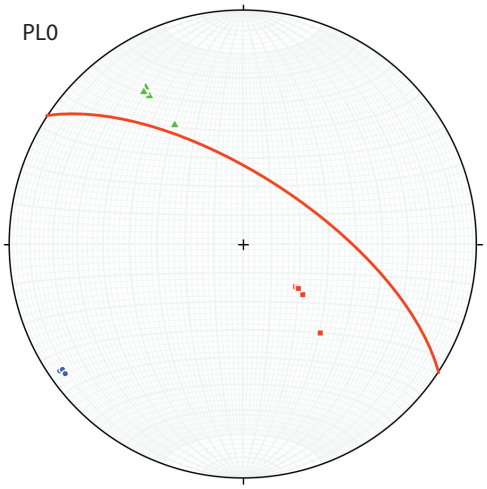

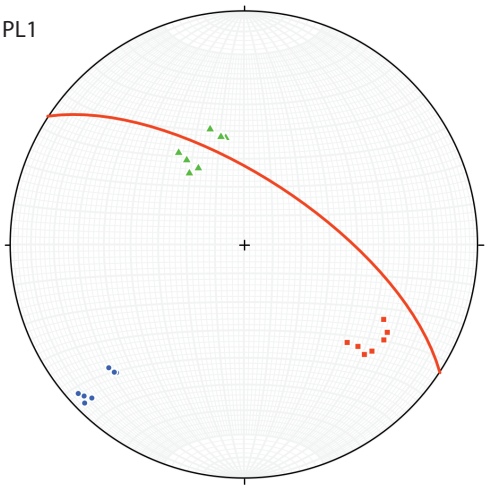

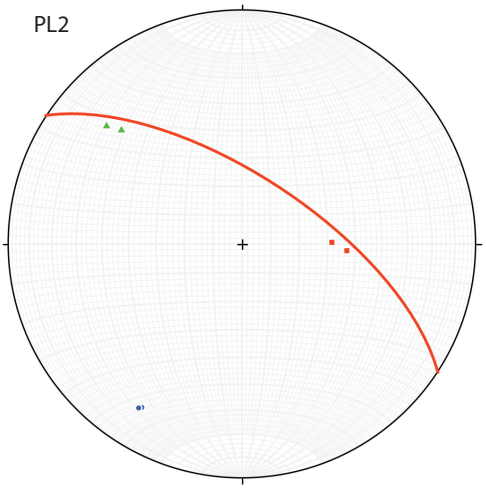

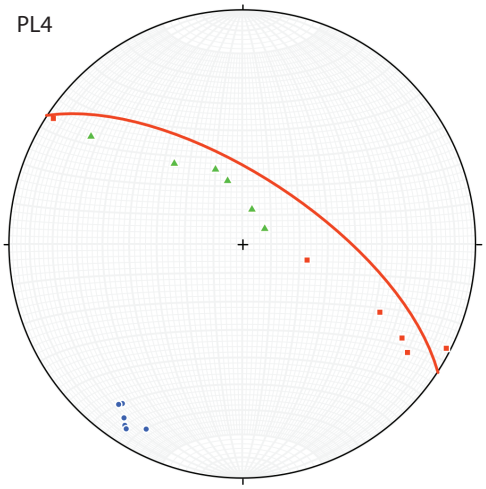

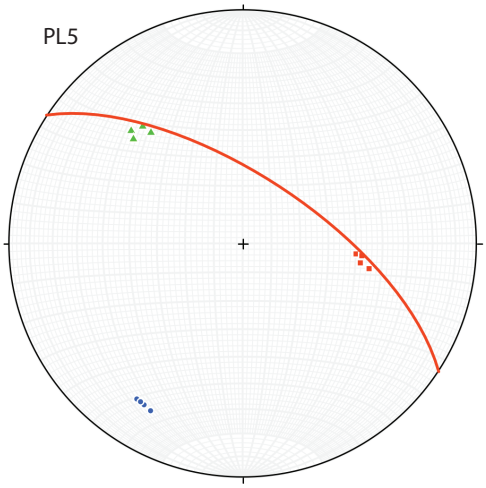

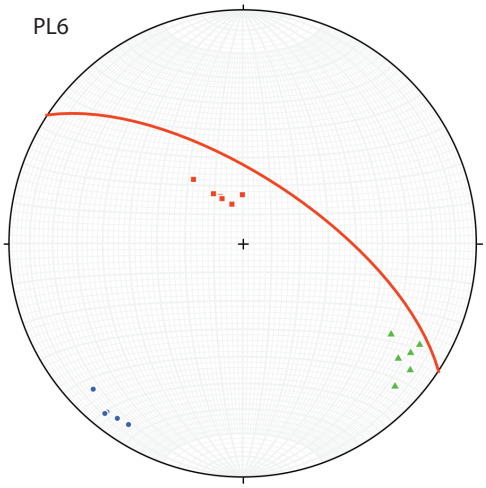

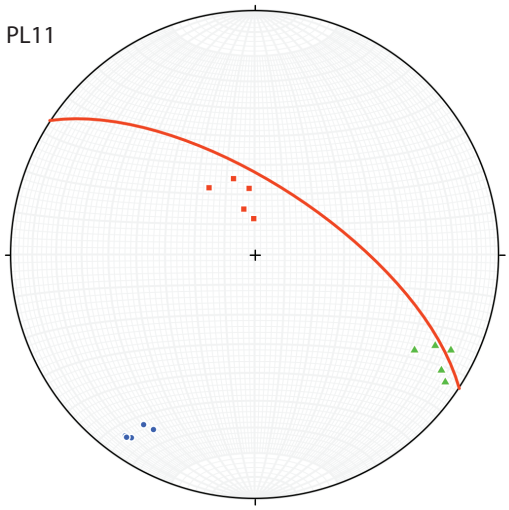
PL11

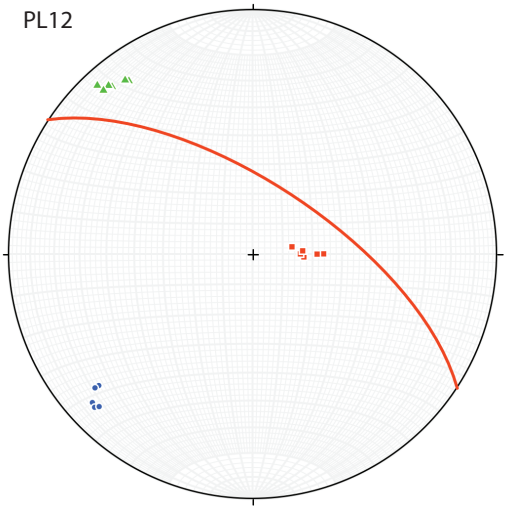
PL12

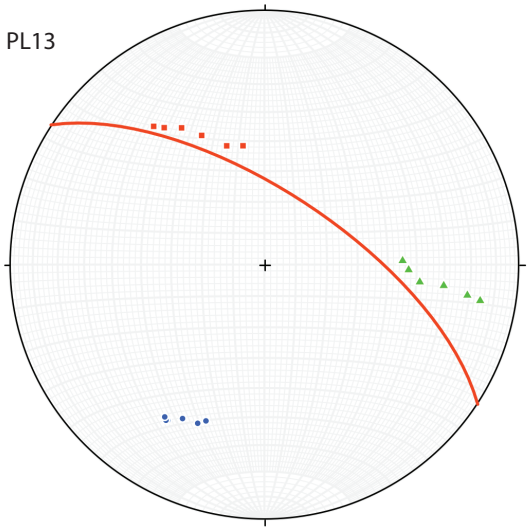
PL13

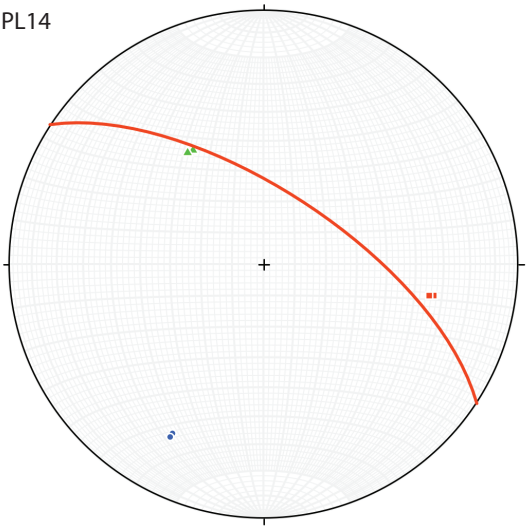
PL14

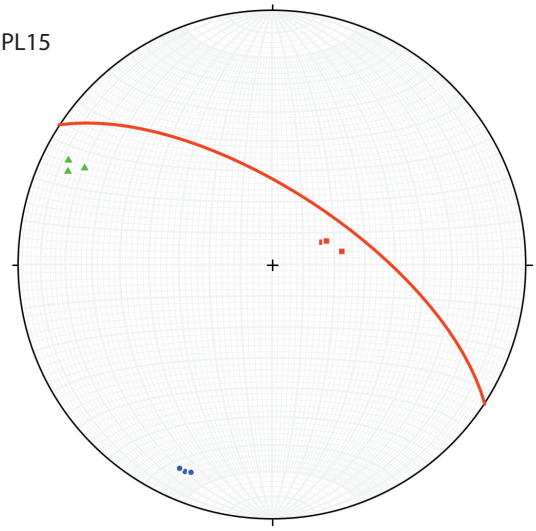
PL15

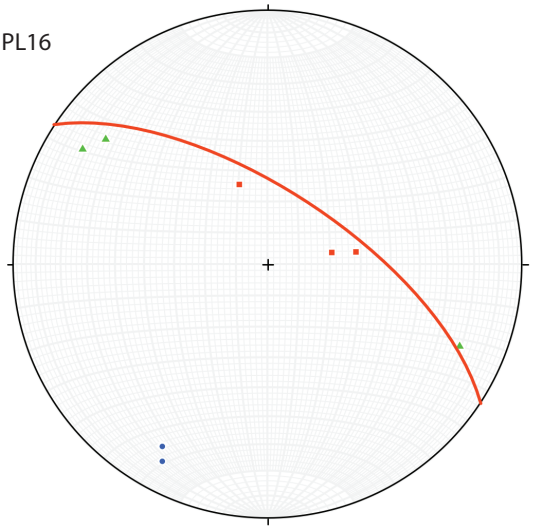
PL16

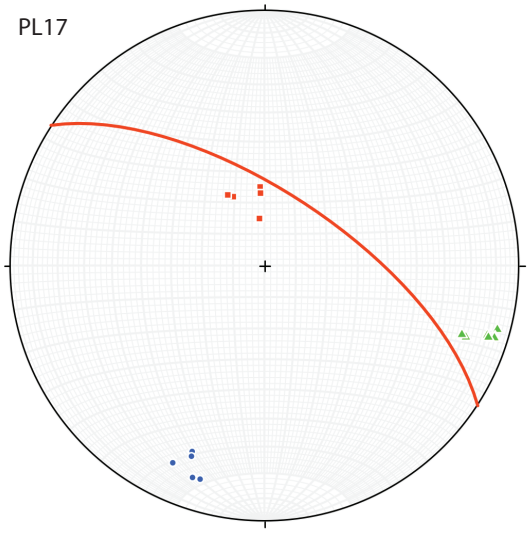
PL17

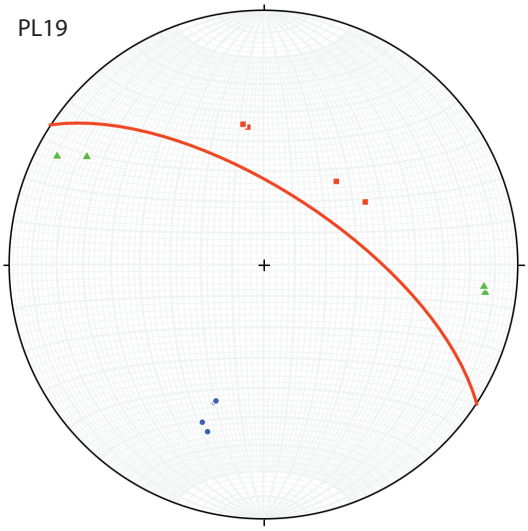
PL19

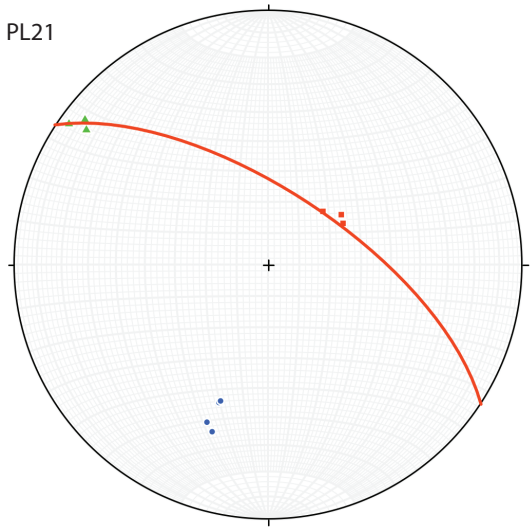
PL21

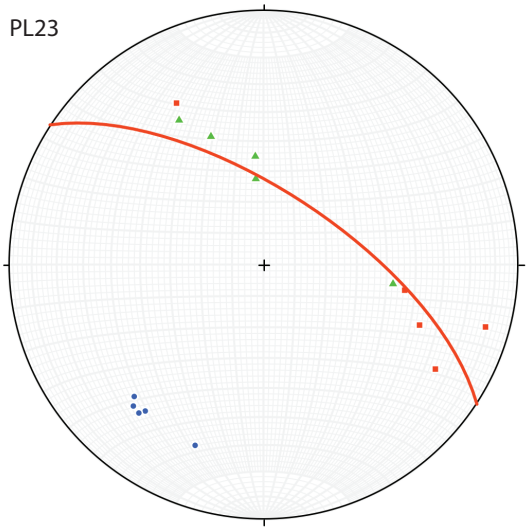
PL23

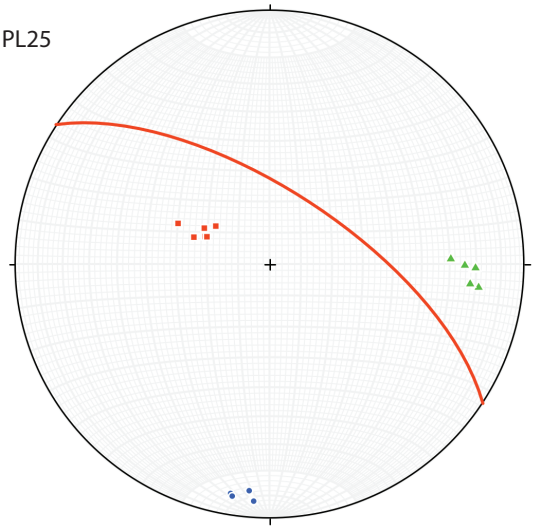
PL25

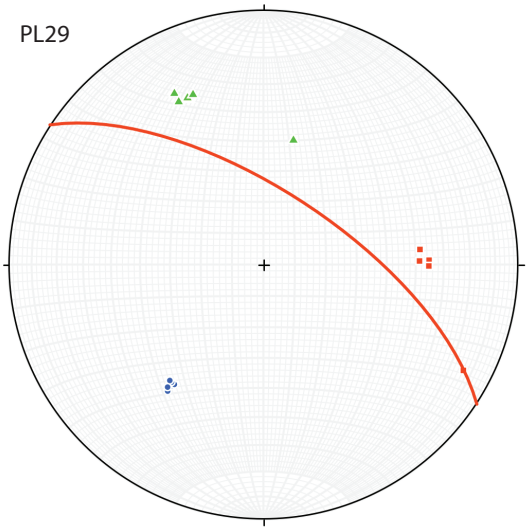
PL29

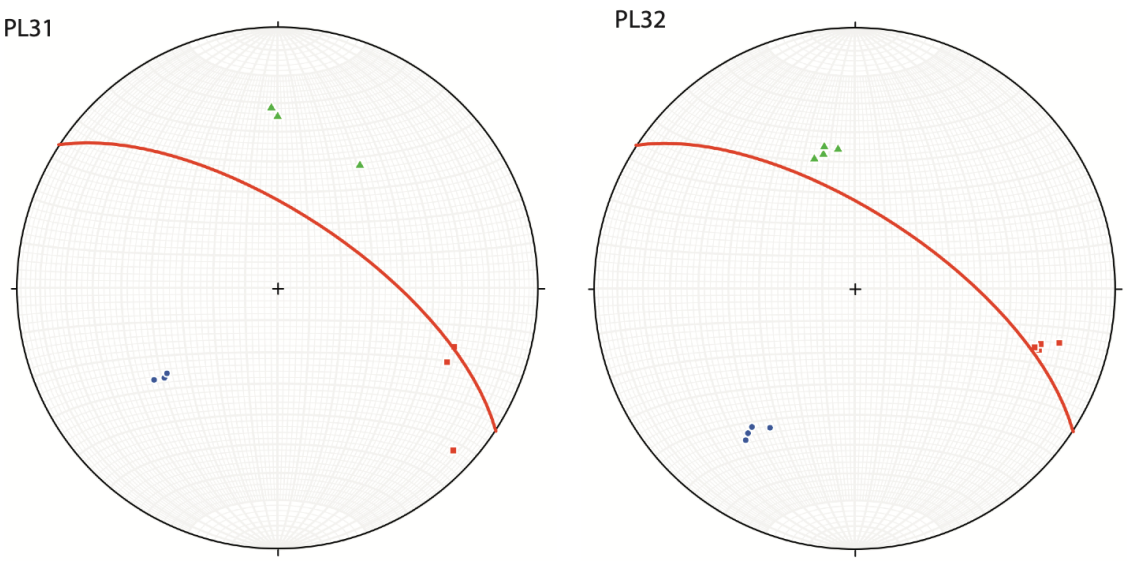

Specimen	Kmean	P	Pj	T	Kmax_Dec	Kmax_Inc	Kint_Dec	Kint_Inc	Kmin_Dec	Kmin_Inc	Distance	Type
PL0A	0.0002737	1.0633	1.071	0.8657	130.1	62.6	327.7	26.3	234.1	7.2	0	Schist/Phyllite
PL0B	0.0002705	1.0581	1.065	0.8513	138.9	48.3	330.2	41.2	235.3	5.6	0	Schist/Phyllite
PL0C	0.0002766	1.0616	1.0688	0.8472	128.9	66.3	328.2	22.5	235.2	7	0	Schist/Phyllite
PL0D	0.0002722	1.0638	1.0709	0.8263	128.6	65.2	326.9	23.7	233.9	6.9	0	Schist/Phyllite
PL1A	0.0002617	1.0981	1.1085	0.7957	118.2	32.8	343.7	47.5	224.8	23.9	2	Schist/Phyllite
PL1B	0.0002373	1.1017	1.1117	0.7654	132.4	31	322.6	58.6	225.1	4.6	2	Schist/Phyllite
PL1C	0.0002526	1.1026	1.1127	0.7664	131.8	35	325.9	54.2	226.5	6.7	2	Schist/Phyllite
PL1D	0.000242	1.0907	1.0996	0.7671	124.3	28.5	350.4	51.9	227.6	23	2	Schist/Phyllite
PL1E	0.0001969	1.0947	1.1012	0.6391	129.8	29.6	329.2	58.9	224.7	8.6	2	Schist/Phyllite
PL1F	0.0002458	1.1021	1.1107	0.7046	133.5	39.1	324.6	50.3	228	5.5	2	Schist/Phyllite
PL1G	0.0002477	1.0949	1.1047	0.7875	121.5	29	348	51.2	225.4	23.4	2	Schist/Phyllite
PL2A	0.0002389	1.0596	1.0675	0.909	93.7	53	313.3	30.1	211.5	19.4	2.5	Schist/Phyllite
PL2B	0.0002388	1.0601	1.0684	0.9261	89	58.5	311	24.5	212.2	18.5	2.5	Schist/Phyllite
PL4A	0.0002617	1.0484	1.0515	0.628	120.4	21.9	340.2	62.4	217	16	5.4	Schist/Phyllite
PL4B	0.0002683	1.0459	1.0497	0.7159	123.2	16.7	346.9	67.5	217.7	14.7	5.4	Schist/Phyllite
PL4C	0.0002571	1.0383	1.0424	0.822	303.5	3.6	56.1	80.6	213	8.7	5.4	Schist/Phyllite
PL4D	0.000246	1.0342	1.039	0.9352	117	2.4	15.8	77.6	207.5	12.1	5.4	Schist/Phyllite
PL4E	0.0002343	1.0463	1.0491	0.6048	116.3	34.7	319.7	53	214.3	11.3	5.4	Schist/Phyllite
PL4F	0.0002343	1.0342	1.0383	0.8702	103.9	66.7	305.3	21.9	212.2	7.7	5.4	Schist/Phyllite
PL5A	0.0002748	1.1383	1.1386	0.116	95.3	49.8	315.3	32.9	211.4	20.4	15.8	Schist/Phyllite
PL5B	0.0003652	1.1176	1.1191	0.2726	99.4	47.8	319.5	34.7	214.2	20.8	15.8	Schist/Phyllite
PL5C	0.0005954	1.0537	1.0562	0.5322	101.3	44.2	320.4	38.6	212.8	20.7	15.8	Schist/Phyllite
PL5D	0.000265	1.1088	1.1097	0.2197	95.9	47.6	313.7	35.8	208.8	19.6	15.8	Schist/Phyllite
PL6A	0.00005447	1.0998	1.1101	0.7859	322.5	61.8	121.5	26.6	215.9	8.7	30.1	Quartzite
PL6B	0.00005431	1.1032	1.1123	0.7243	359.7	73.1	133.2	11.8	225.7	11.9	30.1	Quartzite
PL6C	0.0000588	1.1008	1.1103	0.7462	344.7	75.9	127.1	11.3	218.8	8.4	30.1	Quartzite
PL6D	0.00005865	1.1077	1.1147	0.6171	329.6	70	126.5	18.5	219	7.3	30.1	Quartzite
PL6E	0.00005182	1.1026	1.108	0.5556	334.7	72	123.1	15.5	215.6	9	30.1	Quartzite
PL6F	0.00005483	1.097	1.1036	0.6338	335.3	72.9	119.8	14	212.2	9.5	30.1	Quartzite
PL11A	8.013E-06	1.5402	1.5948	0.7091	346.7	74.5	121.8	11.1	213.9	10.7	38.5	Quartzite
PL11B	0.00000528	1.8854	2.0062	0.785	355.3	67.9	116	11.7	210	18.5	38.5	Quartzite
PL11D	8.014E-06	1.5509	1.5984	0.653	325.7	63	120.9	24.8	215.5	9.9	38.5	Quartzite
PL11E	0.00000533	1.8045	1.8995	0.7379	344.5	63.7	116.8	18.4	213.1	18.1	38.5	Quartzite
PL11F	8.293E-06	1.4612	1.49	0.5633	358.7	78.1	123.8	6.9	215	9.7	38.5	Quartzite

Specimen	Kmean	P	Pj	T	Kmax_Dec	Kmax_Inc	Kint_Dec	Kint_Inc	Kmin_Dec	Kmin_Inc	Distance	Type
PL12A	0.0001216	1.0964	1.1052	0.738	89.9	66.3	324.4	14.3	229.5	18.5	40.2	Impure Quartzite
PL12B	0.0001499	1.1119	1.1185	0.5838	93.3	72.9	319.9	11.9	227.3	12.1	40.2	Impure Quartzite
PL12C	0.0001499	1.1107	1.1172	0.5888	89.9	74.1	319.4	10.5	227.2	11.8	40.2	Impure Quartzite
PL12D	0.0001543	1.1037	1.1098	0.5842	90.1	68.5	323.7	13.1	229.7	16.7	40.2	Impure Quartzite
PL12E	0.00008657	1.1678	1.1826	0.7107	79.7	76.7	317.3	7.2	225.9	11.1	40.2	Impure Quartzite
PL12F	0.00009496	1.162	1.1782	0.7606	86.4	73.3	317.6	10.6	225.2	12.7	40.2	Impure Quartzite
PL13A	0.00006483	1.2062	1.2261	0.7388	342.4	49.6	98.6	20.6	202.8	33	40.8	Qtz-rich Phyllite
PL13B	0.00005461	1.233	1.2569	0.7599	349.8	50.9	99.5	15.3	200.5	34.9	40.8	Qtz-rich Phyllite
PL13C	0.0002135	1.1717	1.1925	0.8386	321.3	31.2	88.4	44.9	211.8	28.9	40.8	Qtz-rich Phyllite
PL13D	0.0002039	1.1817	1.2075	0.91	323.8	33.9	92.1	42.8	212.3	28.6	40.8	Qtz-rich Phyllite
PL13E	0.0001477	1.1818	1.1955	0.6545	334.1	43.1	96.7	29.9	208	32.2	40.8	Qtz-rich Phyllite
PL13F	0.0002	1.1866	1.2082	0.8166	328.8	37.4	96.4	38.6	213.2	29.4	40.8	Qtz-rich Phyllite
PL14A	0.00001059	1.5218	1.6074	0.9126	100.5	32.6	328.3	46.4	208.2	25.5	41.2	Impure Quartzite
PL14B	0.00001043	1.655	1.7786	0.9587	100.8	34.2	325.8	46.1	208.3	23.9	41.2	Impure Quartzite
PL15A	0.0001944	1.2226	1.2502	0.8391	79.4	67.2	297.2	18.4	202.8	13	42	Phyllite
PL15B	0.000265	1.2023	1.2172	0.6436	66	72.5	297.1	11.2	204.4	13.3	42	Phyllite
PL15C	0.0002659	1.1658	1.1774	0.6311	66.7	71	294.5	13	201.3	13.6	42	Phyllite
PL16A	8.782E-06	1.733	1.8348	0.8094	79.8	69.1	301.9	15.8	208	13.3	44.5	Quartzite
PL16B	0.0000086	1.6101	1.713	0.9113	82.2	61.3	307.7	21	210.2	18.7	44.5	Quartzite
PL16C	0.00000871	1.6141	1.714	0.8942	340.6	62.9	113.2	19.1	209.9	18.5	44.5	Quartzite
PL17A	0.00006382	1.2759	1.3076	0.7965	335.6	65.9	109.5	17.3	204.7	16.3	45.3	Impure Quartzite
PL17B	0.00006926	1.2512	1.2786	0.7795	353.1	74.9	105.3	5.9	196.8	13.9	45.3	Impure Quartzite
PL17C	0.0000637	1.2785	1.3104	0.7956	332.5	64.6	109.2	19.1	205	16.1	45.3	Impure Quartzite
PL17D	0.00008024	1.2366	1.2619	0.7736	356.9	64.9	107.3	9.3	201.3	23.1	45.3	Impure Quartzite
PL17E	0.00006285	1.251	1.2782	0.7781	355.1	74.8	107.2	5.8	198.7	14	45.3	Impure Quartzite
PL17F	0.00006278	1.2522	1.2792	0.7716	354	75	107.4	6.1	198.8	13.6	45.3	Impure Quartzite
PL17G	0.00007879	1.2291	1.2535	0.7736	356.9	66.9	107.7	8.6	201	21.3	45.3	Impure Quartzite
PL19A	0.00001303	1.1366	1.1481	0.7002	58.4	51.3	301.4	20	198.5	31.5	49.6	Quartzite
PL19B	0.00001166	1.2654	1.2876	0.6787	353.5	44.9	97.2	13.4	199.6	42.1	49.6	Quartzite
PL19C	0.00001159	1.2743	1.2981	0.689	351.7	43.7	95.7	14.2	199.2	42.8	49.6	Quartzite
PL19D	0.000013	1.1491	1.1592	0.6228	41.2	54.3	297.7	9.5	201.2	34.1	49.6	Quartzite
PL21A	0.00001594	1.4011	1.447	0.7748	46	65.5	305.2	4.9	213.1	24	56.5	Quartzite
PL21B	0.00001551	1.5886	1.6708	0.8299	61.3	62.5	306.5	12.3	210.9	24.2	56.5	Quartzite
PL21C	0.00001139	1.6833	1.77	0.7787	116.4	13.4	355.4	65.1	211.5	20.6	56.5	Quartzite
PL21E	0.00002439	1.2845	1.3076	0.6651	55.8	61.5	308.3	9.3	213.6	26.7	56.5	Quartzite
PL23A	0.00002302	1.0601	1.0658	0.759	105.7	10.5	354.9	62.4	200.7	25.2	62.5	Phyllite
PL23B	0.00003269	1.0668	1.0737	0.7954	100.3	43.1	329.7	34.8	218.9	27.1	62.5	Phyllite
PL23C	0.0000382	1.0969	1.1101	0.907	121.3	22.2	355.7	55	222.6	25.6	62.5	Phyllite
PL23D	0.00003803	1.09	1.1001	0.82	111.2	34.7	337.7	44.9	220	25	62.5	Phyllite
PL23E	0.00002439	1.0442	1.0473	0.6414	331.7	28.9	98.5	47.4	224.4	28.4	62.5	Phyllite
PL25A	0.00003378	1.3245	1.3663	0.8363	305.3	69	96.4	18.6	189.6	9.5	73.3	Quartzite
PL25B	0.00001725	1.4581	1.5212	0.8431	293.2	67.6	91.4	20.9	184.3	7.6	73.3	Quartzite
PL25C	0.00003373	1.3283	1.3691	0.8203	298.9	66.2	95.7	22	189.1	8.5	73.3	Quartzite
PL25D	0.0000178	1.789	1.9144	0.8599	293.6	68.2	91.1	20.3	184	7.7	73.3	Quartzite
PL25E	0.000017	1.4378	1.502	0.8745	294	57.8	88.4	29.6	185.1	11.6	73.3	Quartzite
PL25F	0.00003393	1.3453	1.3837	0.7722	289.6	64.3	90.4	24.4	183.8	7.4	73.3	Quartzite
PL29A	0.0001111	1.2585	1.2837	0.7344	90.1	35.7	335.9	29.7	217.3	40	109.4	Quartzite
PL29B	0.00008875	1.2594	1.2851	0.7413	88.5	35.3	335.5	29	216.6	41.1	109.4	Quartzite
PL29C	0.00009352	1.2638	1.2928	0.7817	84.5	38.3	332.5	25.4	218	41.1	109.4	Quartzite
PL29D	0.0001185	1.2383	1.2616	0.7389	88.7	38.7	332.5	28.9	217.1	37.8	109.4	Quartzite
PL29E	0.00009452	1.2481	1.2707	0.7107	90.5	35.4	337.5	28.7	218.9	41.2	109.4	Quartzite
PL29F	0.0001101	1.2537	1.2853	0.8351	117.9	12.3	13.6	48.5	218	38.9	109.4	Quartzite
PL31A	0.0001174	1.0773	1.0878	0.9138	108.4	29.4	358.1	31.7	231.5	44	175.9	Qtz-rich Phyllite
PL31B	0.0001169	1.0687	1.0746	0.7179	132.7	9.2	34	42.9	232.3	45.6	175.9	Qtz-rich Phyllite
PL31D	0.0001123	1.0697	1.0788	0.895	113.6	29.8	0.1	34.8	233.3	40.8	175.9	Qtz-rich Phyllite
PL32D	0.00002678	1.1484	1.1515	0.3428	108.4	26.5	346.9	46.3	216.4	31.8	176.3	Impure Quartzite
PL32E	0.00002568	1.34	1.3743	0.7352	106.6	26.5	347.9	43.9	216.6	34.4	176.3	Impure Quartzite
PL32F	0.00004321	1.1867	1.1956	0.5157	108.1	28.3	342.7	47	215.7	29.3	176.3	Impure Quartzite
PL32G	0.00004997	1.1995	1.2046	0.3768	104.9	20	353.2	45.5	211.3	37.7	176.3	Impure Quartzite

APPENDIX C: Pulo do Lobo Magnetic Characterization Data

Sample #	Lithology	m from SZ	VSM	MPMS	Hi-Temp
PL1	schist	17.3	yes	yes+	yes
PL2	schist	21.2	yes	yes	yes
PL3	schist	22.7	yes		
PL4	phyllite	26.6	yes	yes	
PL5	phyllite	40.6	yes	yes+	yes
PL6	phyllite	51.5	yes	yes	yes
PL7	phyllite	53.4	yes		
PL8	phyllite	55.2	yes	yes+	yes
PL9	phyllite	55.7	yes		
SI13A	phyllite w/qtzite	56	yes	yes	yes
PL10	phyllite	57.7	yes	yes	yes
PL11	phyllite	62.2	yes	yes	yes
PL12	phyllite	65.5	yes		
PL13	phyllite	68.1	yes	yes+	yes
PL14	phyllite	76.4	yes	yes	yes
PL15	phyllite	82.9	yes		
PL16	phyllite	92.4	yes		
PL17	phyllite	98	yes		yes
PL18	phyllite	122.8	yes	yes	yes
PL19	phyllite	171.1	yes		
PL20	slate	192.6	yes	yes	yes

specimen	Ms [Am/kg]	Mr [Am/kg]	Bc [mT]	Bcr [mT]	Xhf [m3/kg]	T [K]
PL1a	-1.32E-07	-8.61E-09	-16.3056	0	2.06E-11	294

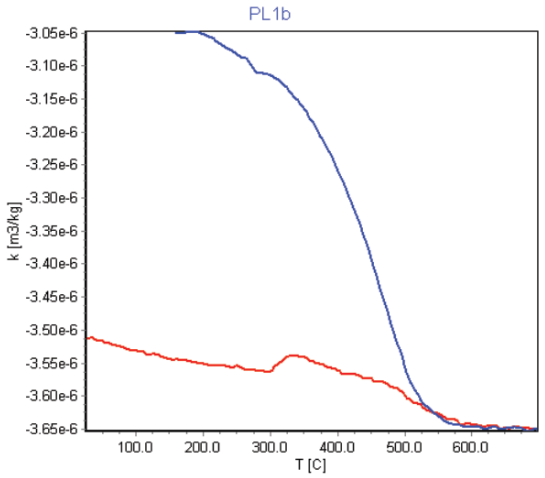

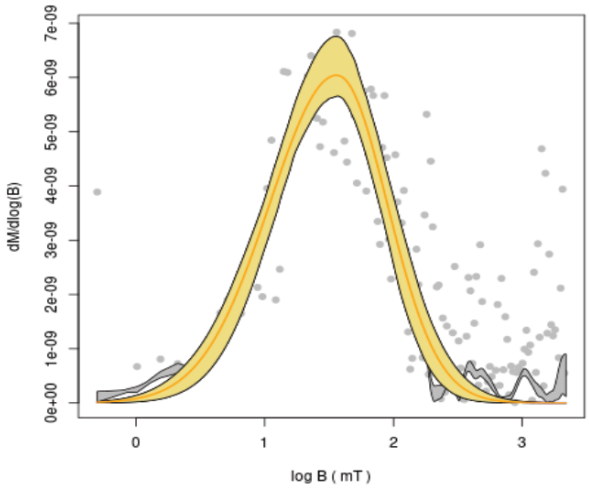

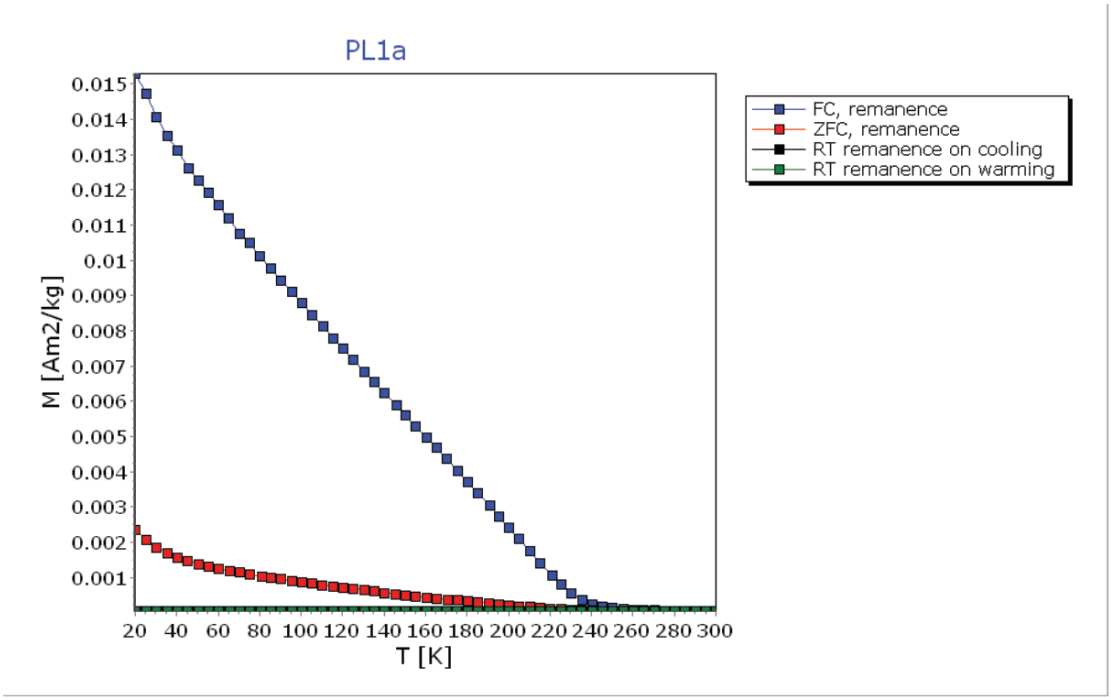

specimen	Ms [Am/kg]	Mr [Am/kg]	Bc [mT]	Bcr [mT]	Xhf [m3/kg]	T [K]
PL2a	-7.70E-08	1.50E-08	23.0413	0	1.70E-11	294

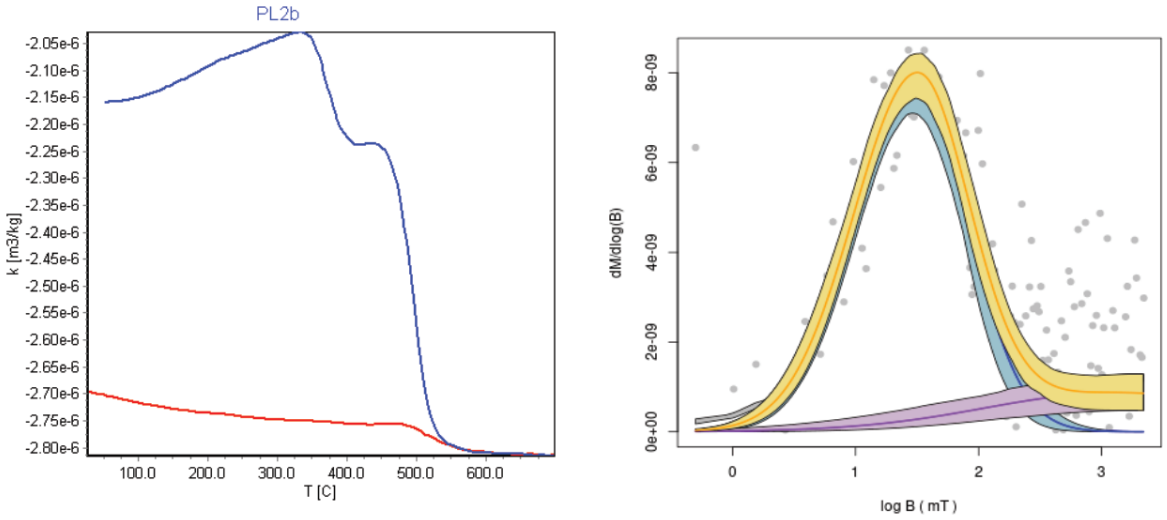

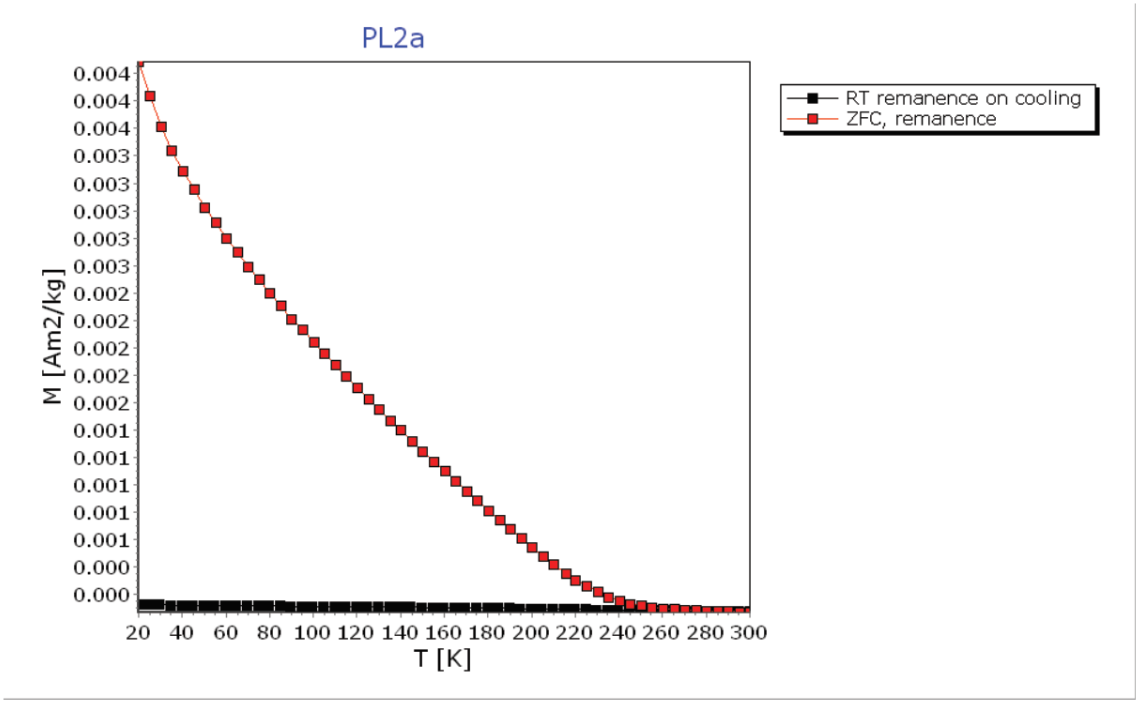

specimen	Ms [Am/kg]	Mr [Am/kg]	Bc [mT]	Bcr [mT]	Xhf [m3/kg]	T [K]
PL3a	-8.90E-08	1.28E-08	16.9745	0	2.03E-11	294

specimen	Ms [Am/kg]	Mr [Am/kg]	Bc [mT]	Bcr [mT]	Xhf [m3/kg]	T [K]
PL4a	-1.08E-07	-1.99E-09	-1.2879	0	1.88E-11	294

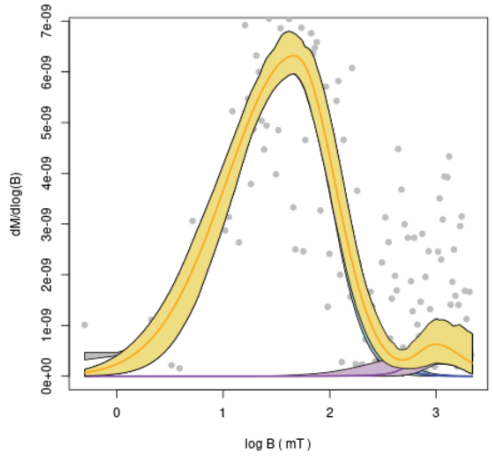

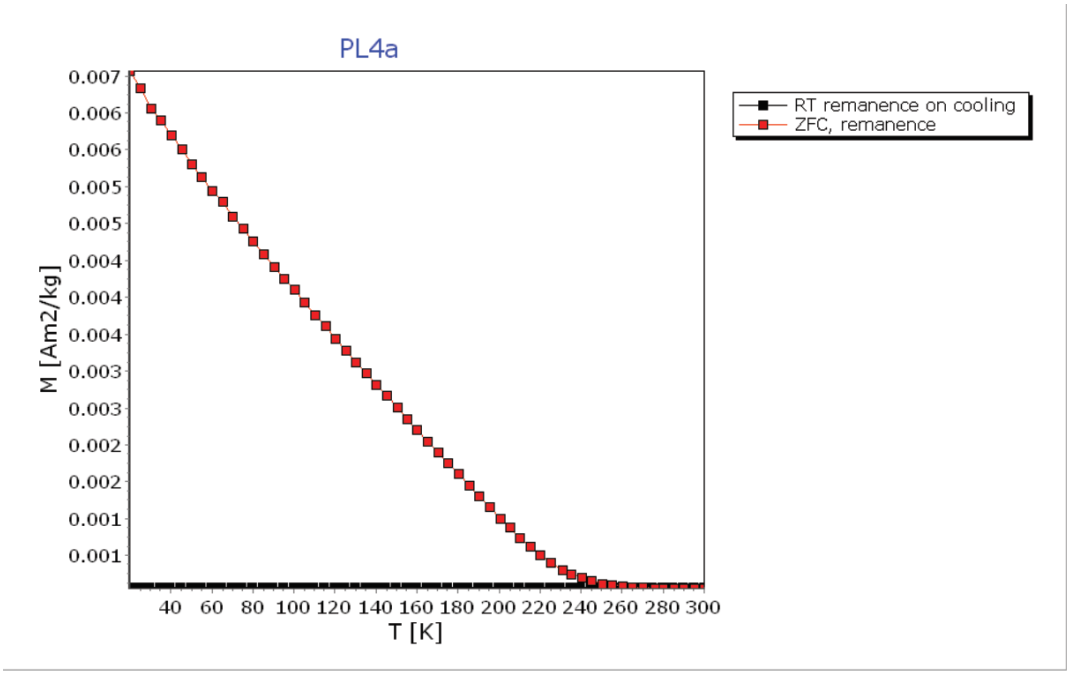

specimen	Ms [Am/kg]	Mr [Am/kg]	Bc [mT]	Bcr [mT]	Xhf [m3/kg]	T [K]
PL5a	-1.05E-07	3.17E-08	43.2794	0	2.49E-11	294

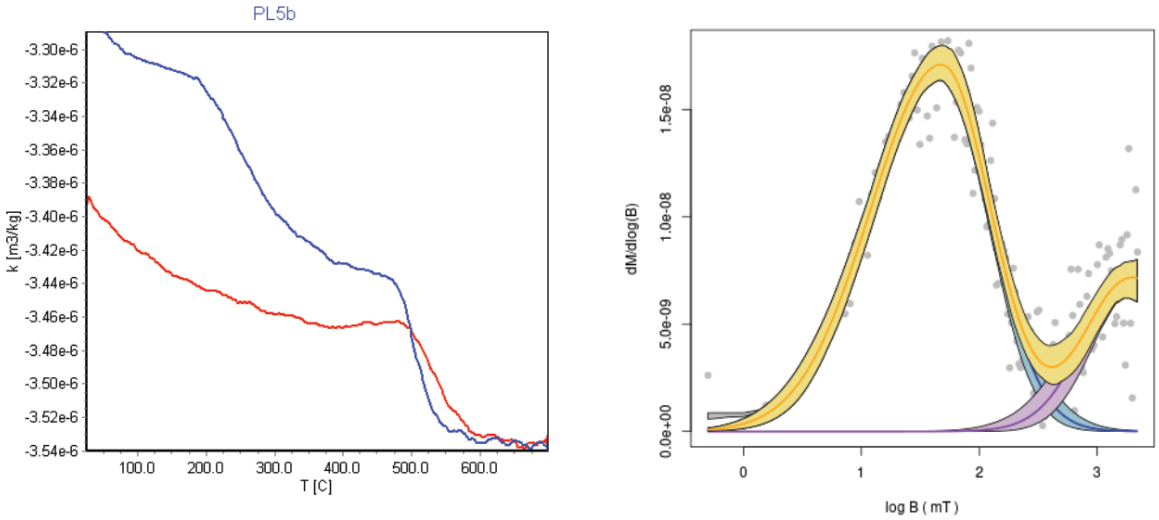

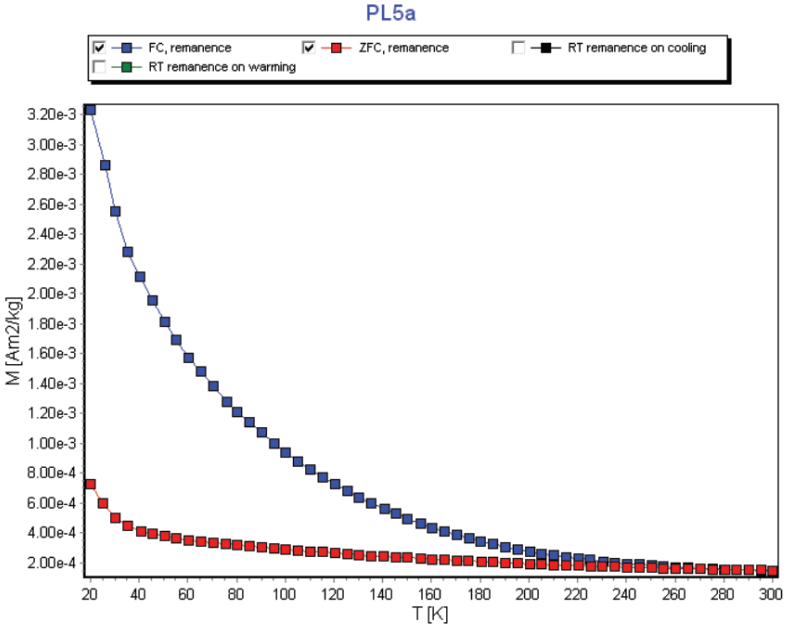

specimen	Ms [Am/kg]	Mr [Am/kg]	Bc [mT]	Bcr [mT]	Xhf [m3/kg]	T [K]
PL6a	-3.02E-07	-1.56E-08	-18.8582	0	4.27E-11	294

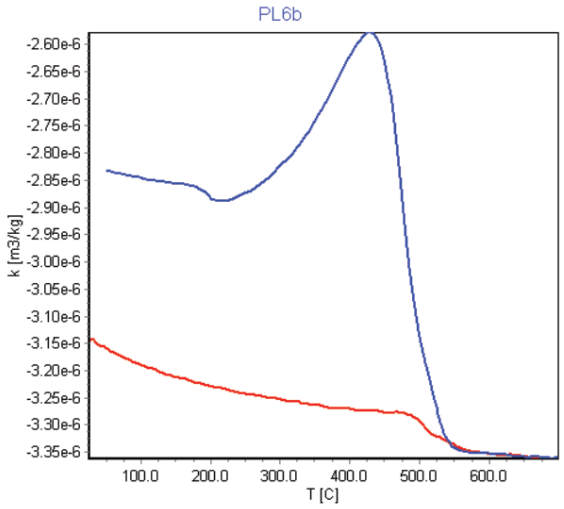

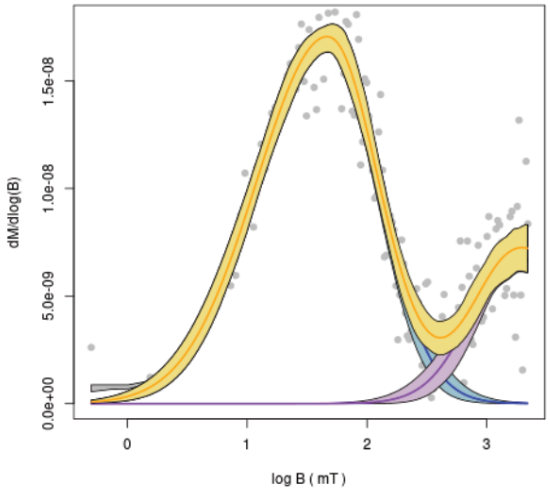

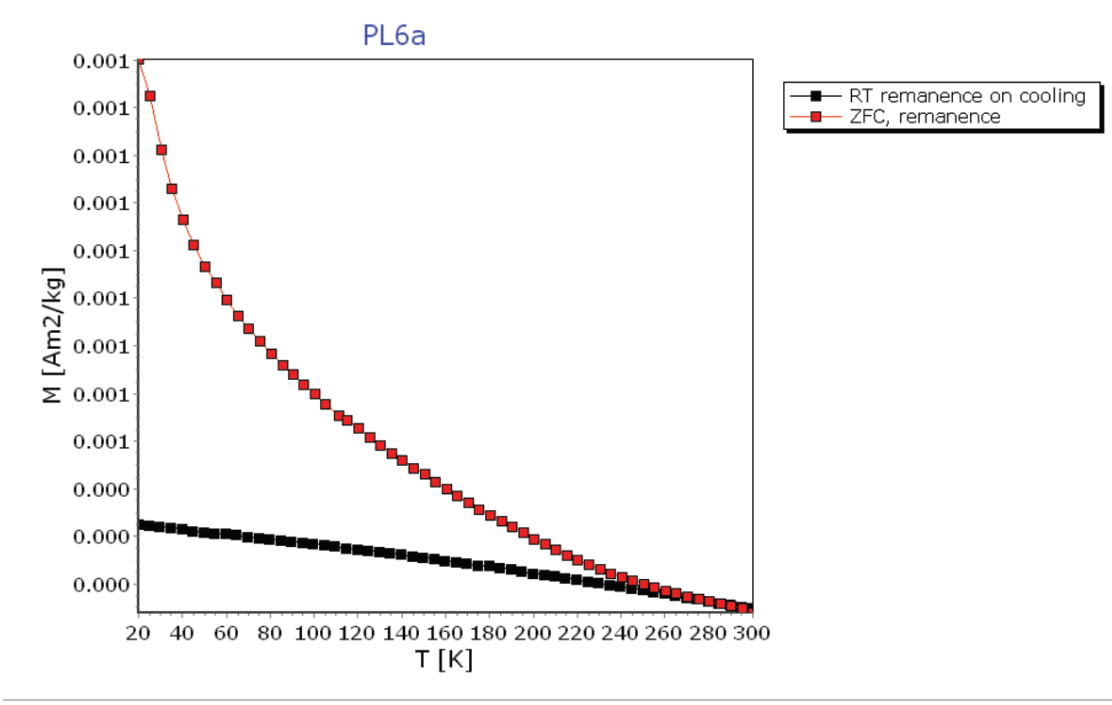

specimen	Ms [Am/kg]	Mr [Am/kg]	Bc [mT]	Bcr [mT]	Xhf [m3/kg]	T [K]
PL7a	1.39E-08	1.25E-08	6.08814	0	1.18E-11	294

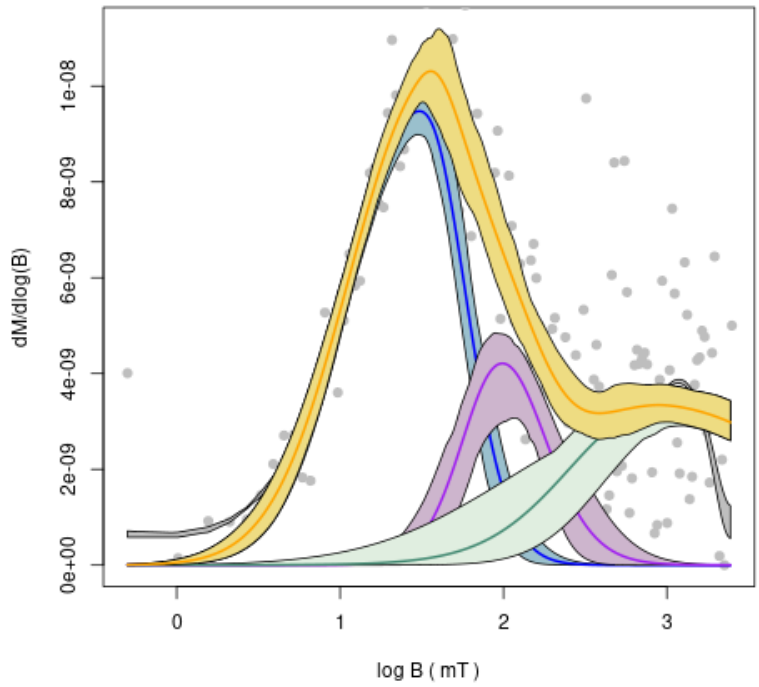

specimen	Ms [Am/kg]	Mr [Am/kg]	Bc [mT]	Bcr [mT]	Xhf [m3/kg]	T [K]
PL8a	0.000739	0.00032	18.3753	724.703	8.20E-08	294

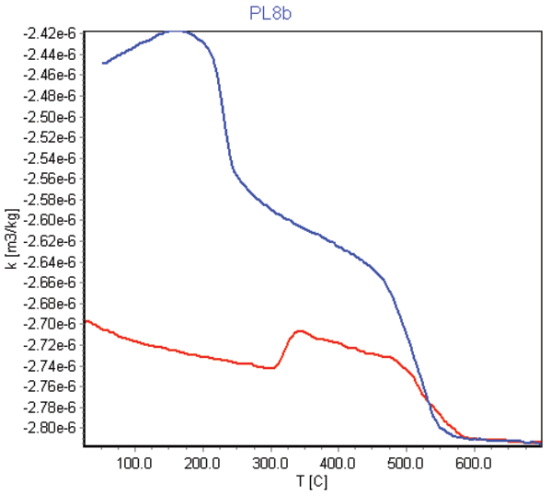

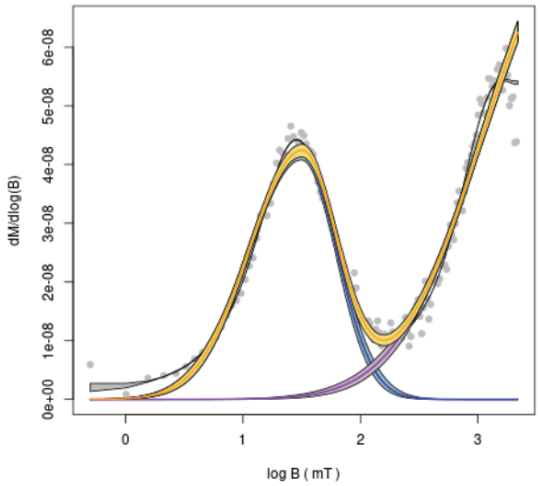

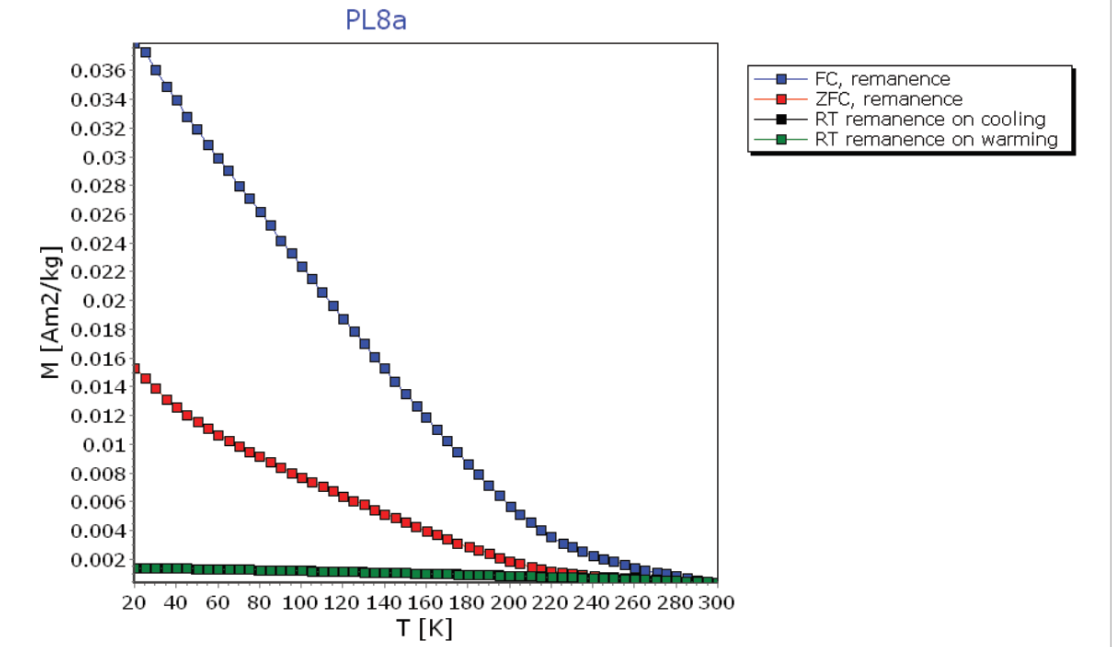

specimen	Ms [Am/kg]	Mr [Am/kg]	Bc [mT]	Bcr [mT]	Xhf [m3/kg]	T [K]
PL9a	-0.00054	8.78E-05	18.9935	439.424	1.11E-07	294

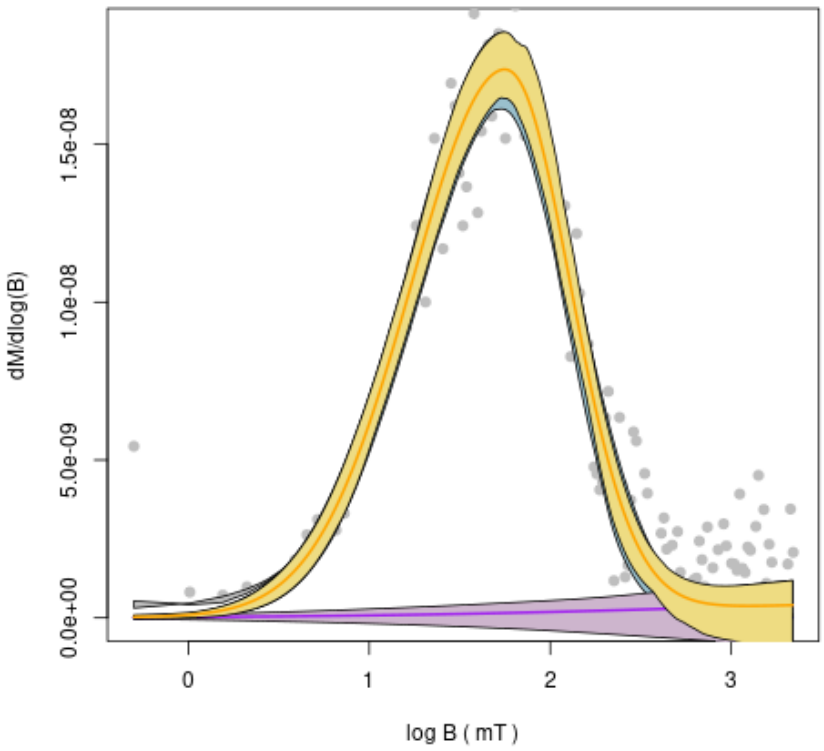

specimen	Ms [Am/kg]	Mr [Am/kg]	Bc [mT]	Bcr [mT]	Xhf [m3/kg]	T [K]
PL10a	-0.00037	1.98E-05	5.67666	0	7.02E-08	294

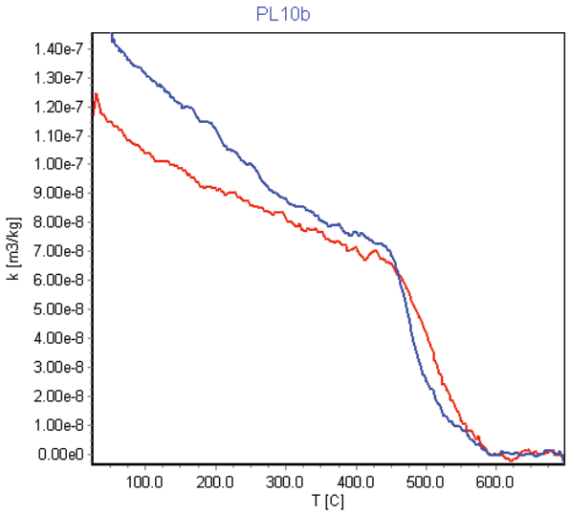

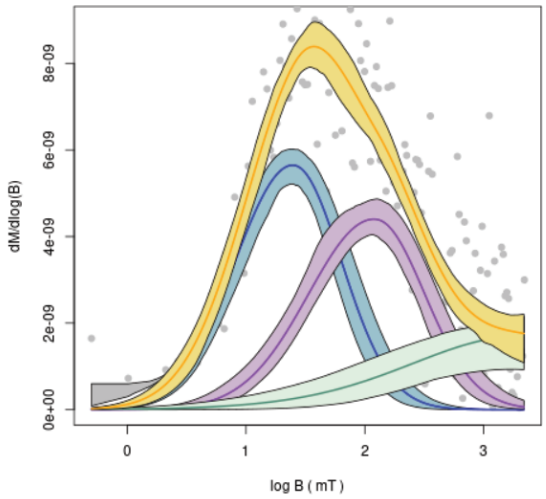

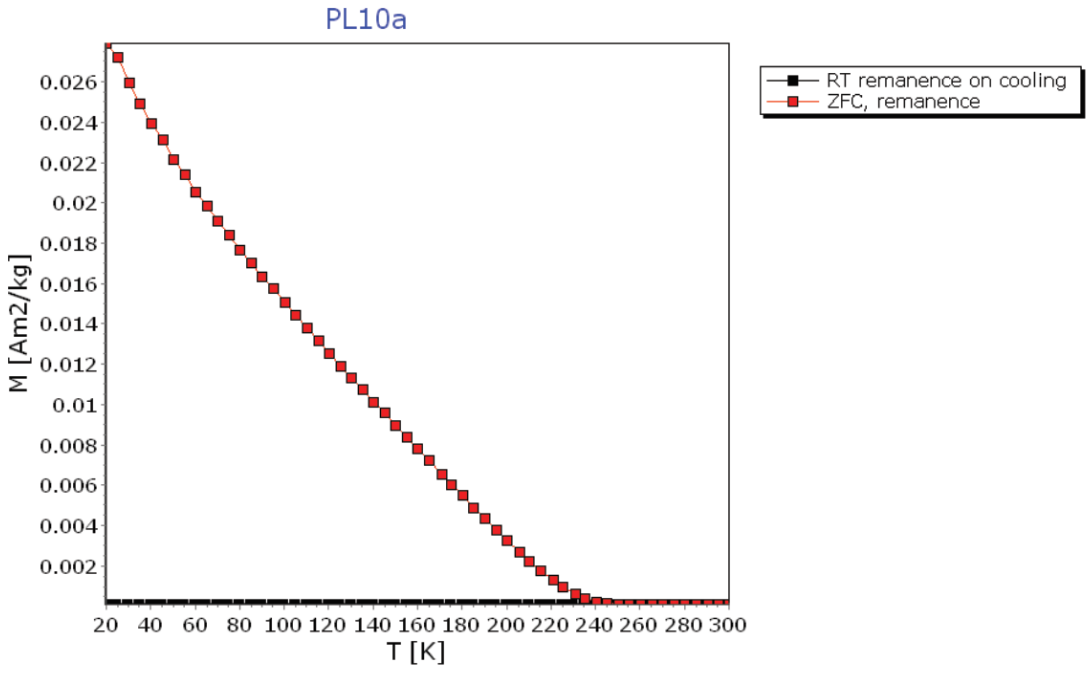

specimen	Ms [Am/kg]	Mr [Am/kg]	Bc [mT]	Bcr [mT]	Xhf [m3/kg]	T [K]
PL11a	0.001189	0.000714	222.302	362.832	8.48E-08	294

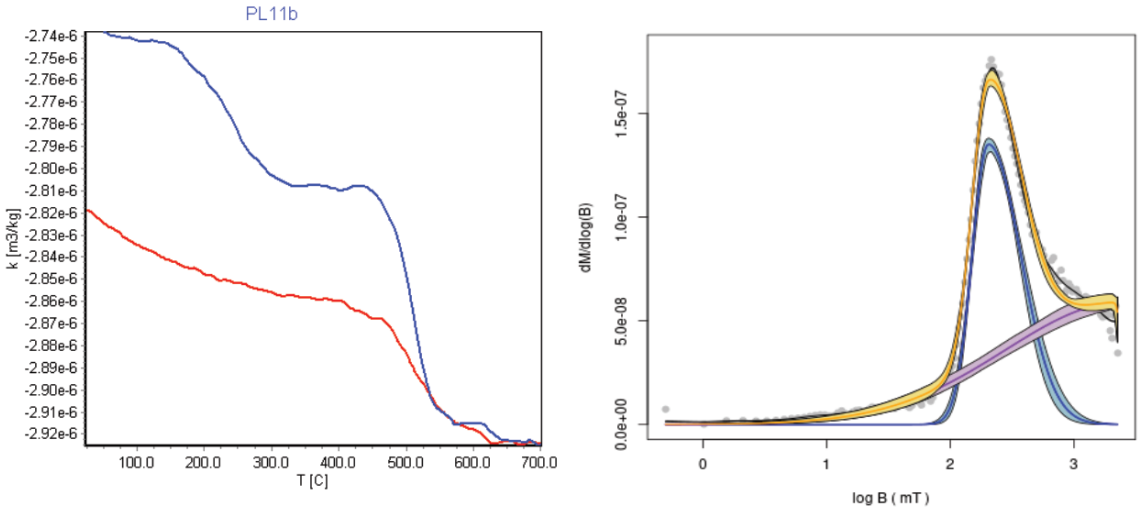

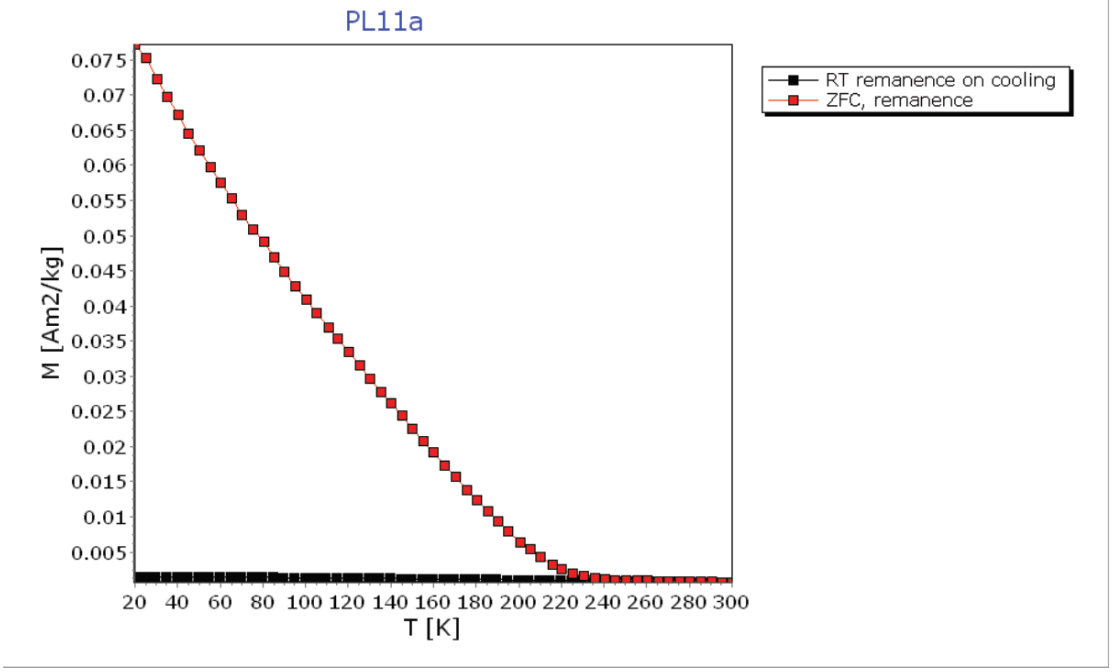

specimen	Ms [Am/kg]	Mr [Am/kg]	Bc [mT]	Bcr [mT]	Xhf [m3/kg]	T [K]
PL12a	-3.94E-08	3.50E-08	29.843	390.673	1.84E-11	294

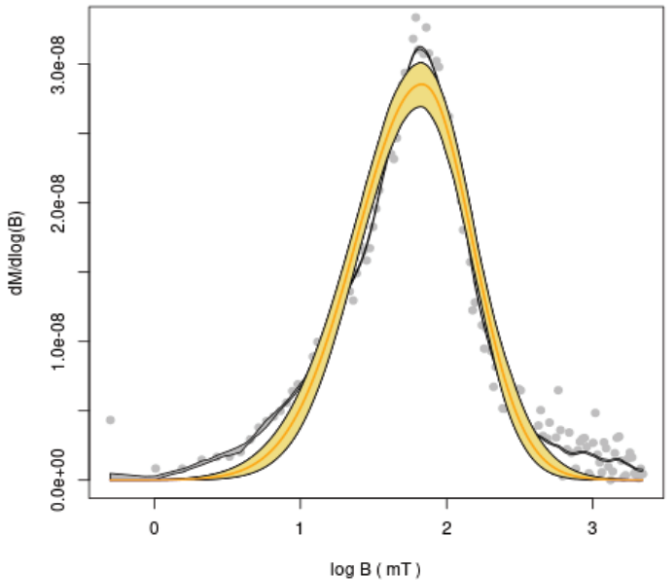

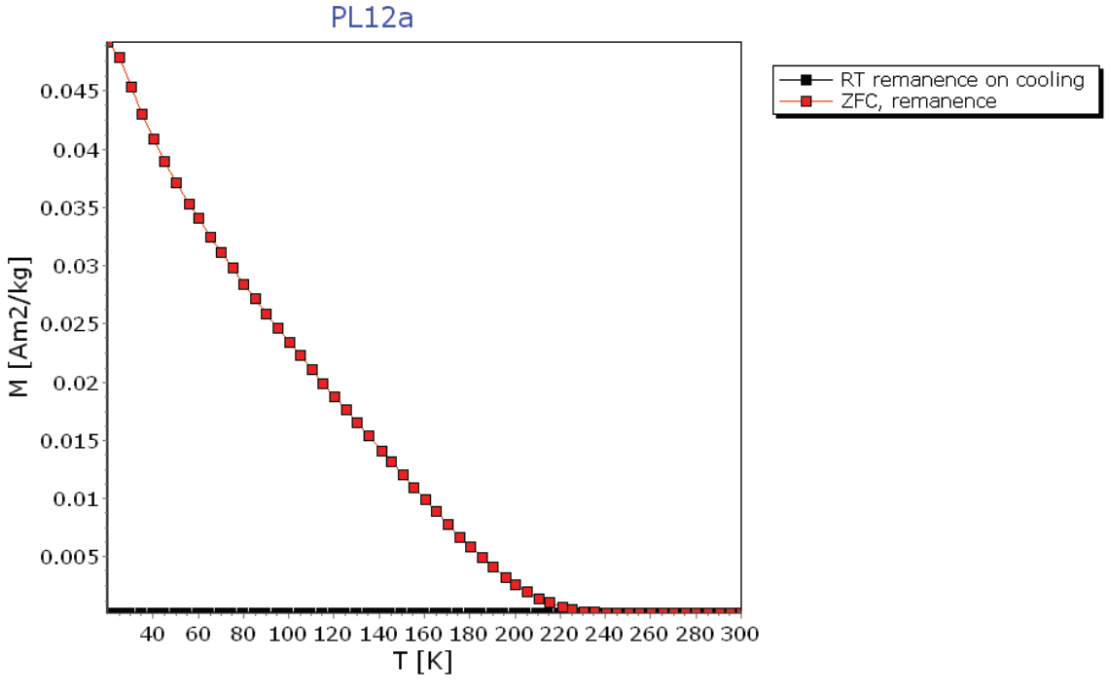

specimen	Ms [Am/kg]	Mr [Am/kg]	Bc [mT]	Bcr [mT]	Xhf [m3/kg]	T [K]
PL13a	0.001661	0.00102	108.304	202.122	4.66E-08	294

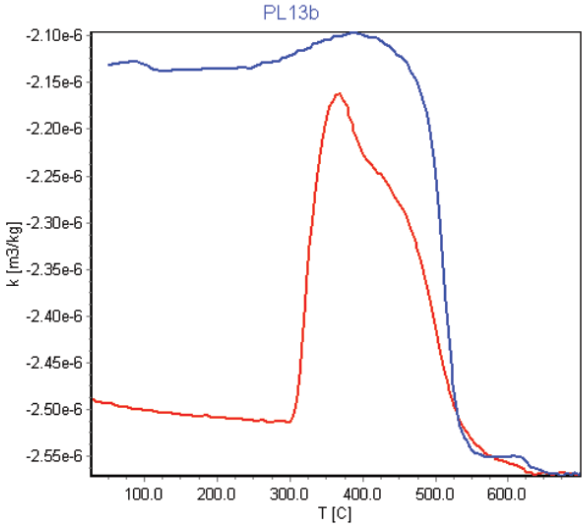

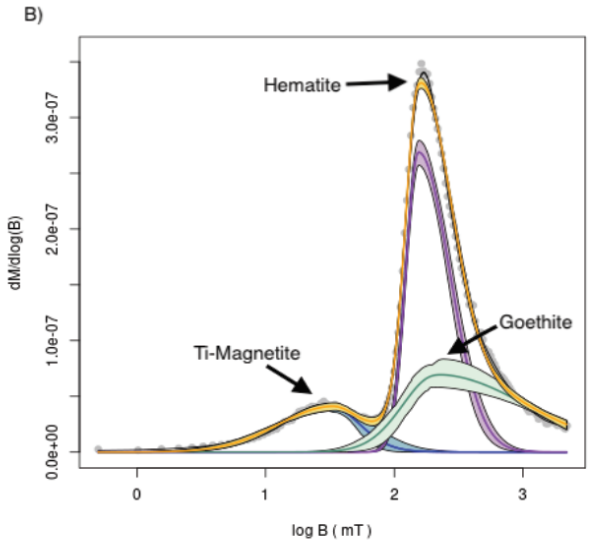

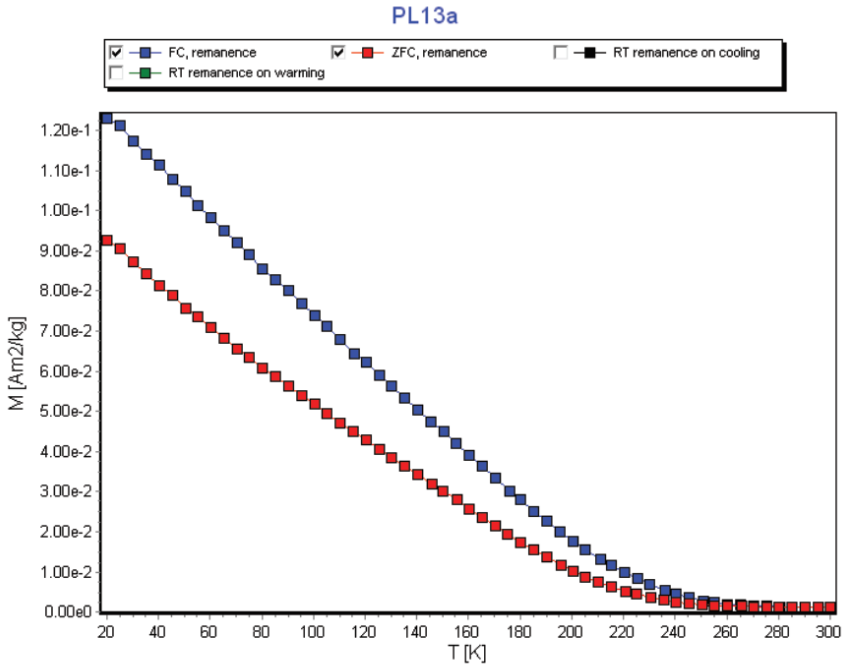

specimen	Ms [Am/kg]	Mr [Am/kg]	Bc [mT]	Bcr [mT]	Xhf [m3/kg]	T [K]
PL14a	0.001987	0.001188	139.527	278.697	3.62E-08	294

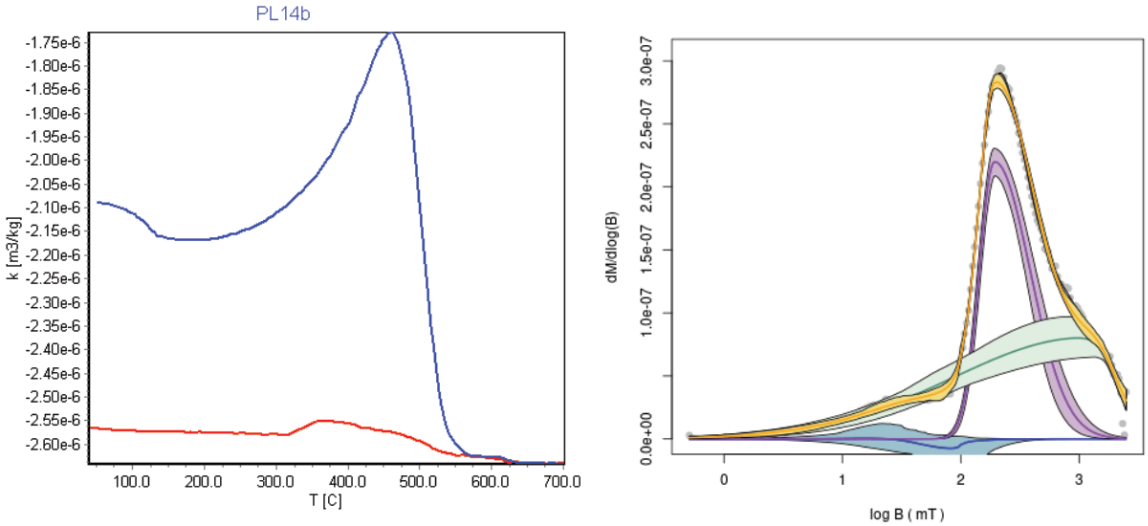

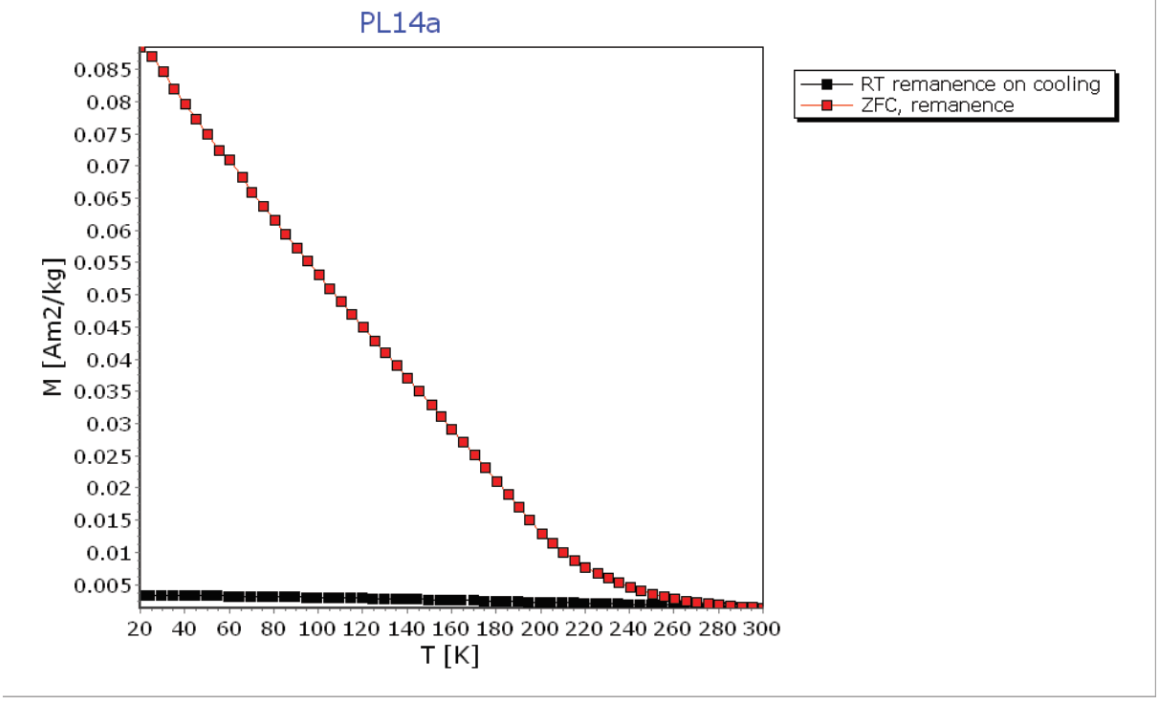

specimen	Ms [Am/kg]	Mr [Am/kg]	Bc [mT]	Bcr [mT]	Xhf [m3/kg]	T [K]
PL15a	0.000157	0.000181	18.6553	1628.67	9.29E-08	294

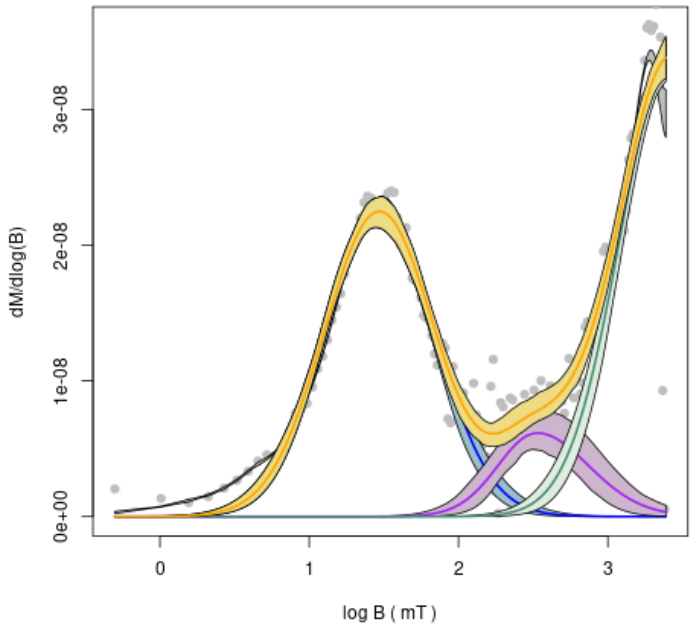

specimen	Ms [Am/kg]	Mr [Am/kg]	Bc [mT]	Bcr [mT]	Xhf [m3/kg]	T [K]
PL16a	-0.0009	5.19E-05	36.0352	0	1.22E-07	294

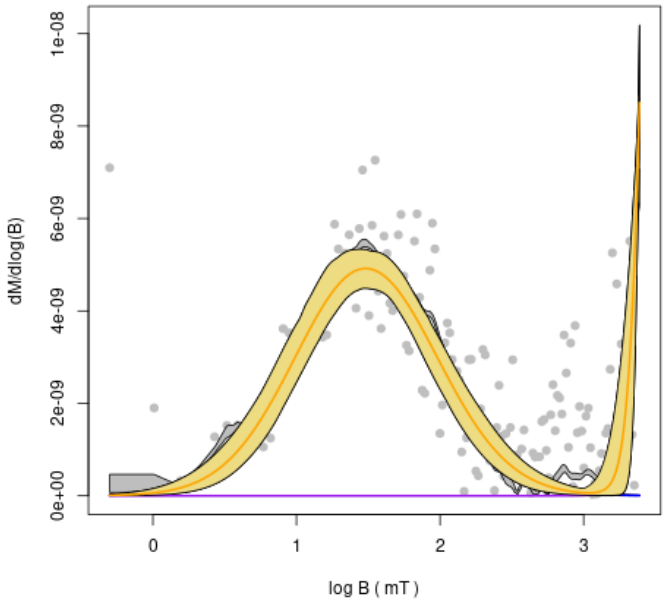

specimen	Ms [Am/kg]	Mr [Am/kg]	Bc [mT]	Bcr [mT]	Xhf [m3/kg]	T [K]
PL17a	0.000628	0.000343	19.0151	233.076	6.40E-08	294

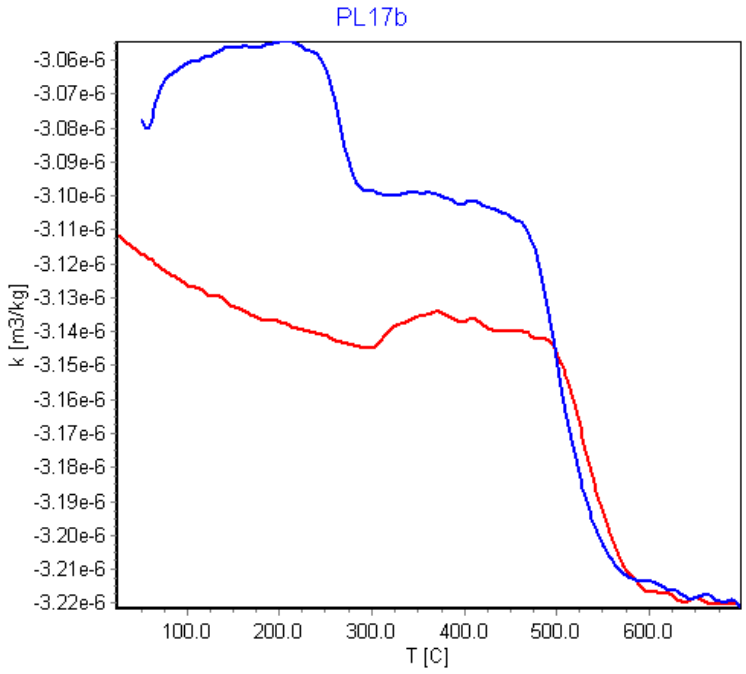

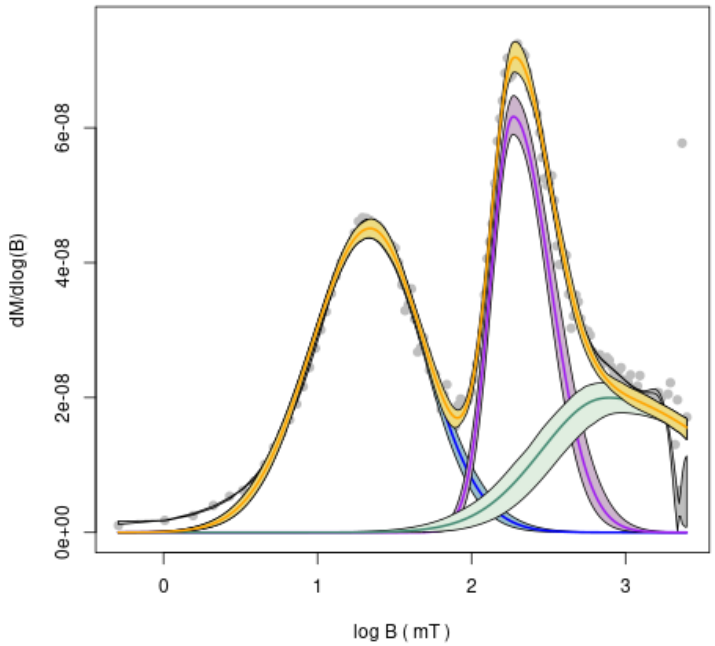

specimen	Ms [Am/kg]	Mr [Am/kg]	Bc [mT]	Bcr [mT]	Xhf [m3/kg]	T [K]
PL18a	-0.00015	7.56E-05	13.6561	0	1.01E-07	294

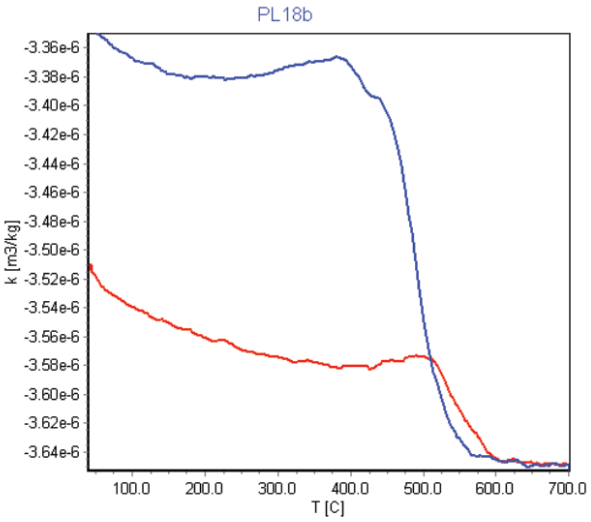

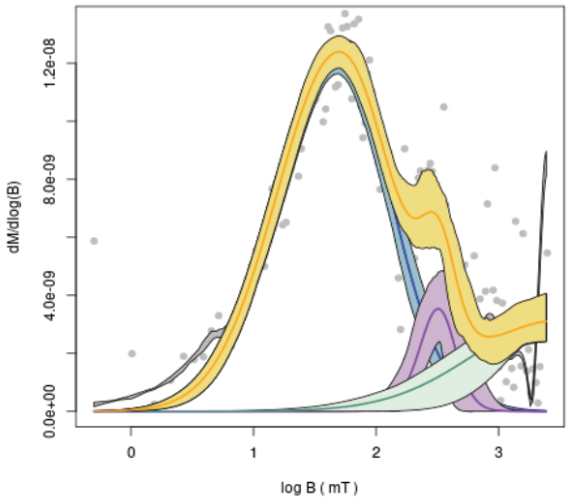

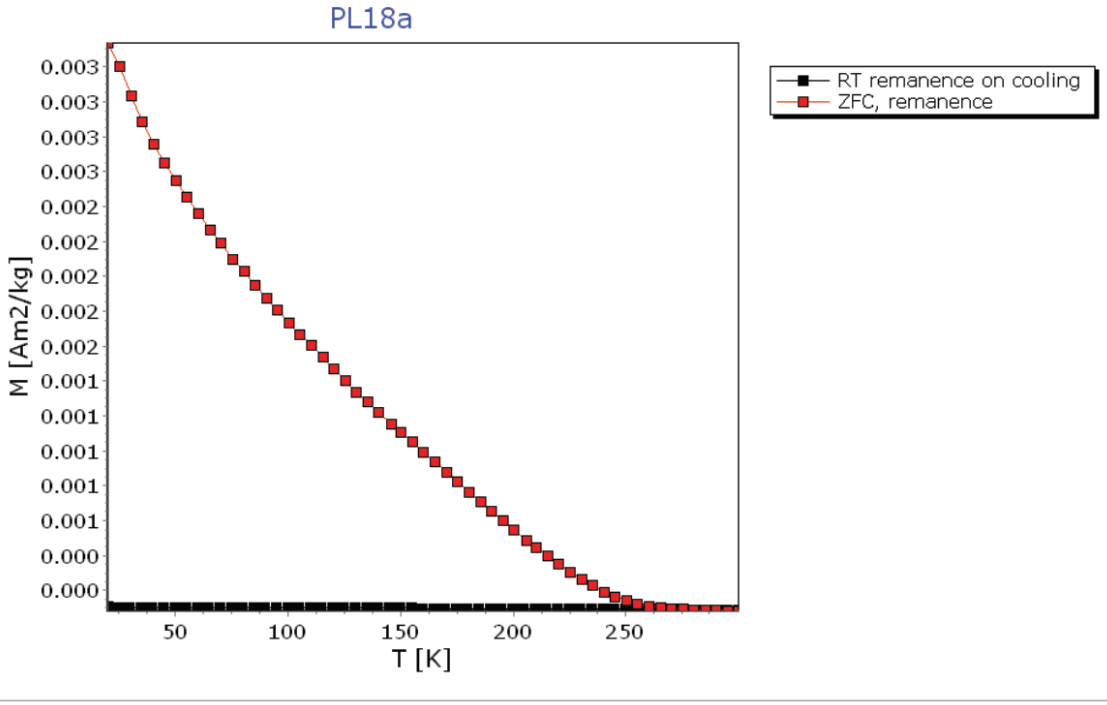

specimen	Ms [Am/kg]	Mr [Am/kg]	Bc [mT]	Bcr [mT]	Xhf [m3/kg]	T [K]
PL19a	-0.00053	-3.13E-05	-4.63067	0	1.02E-07	294

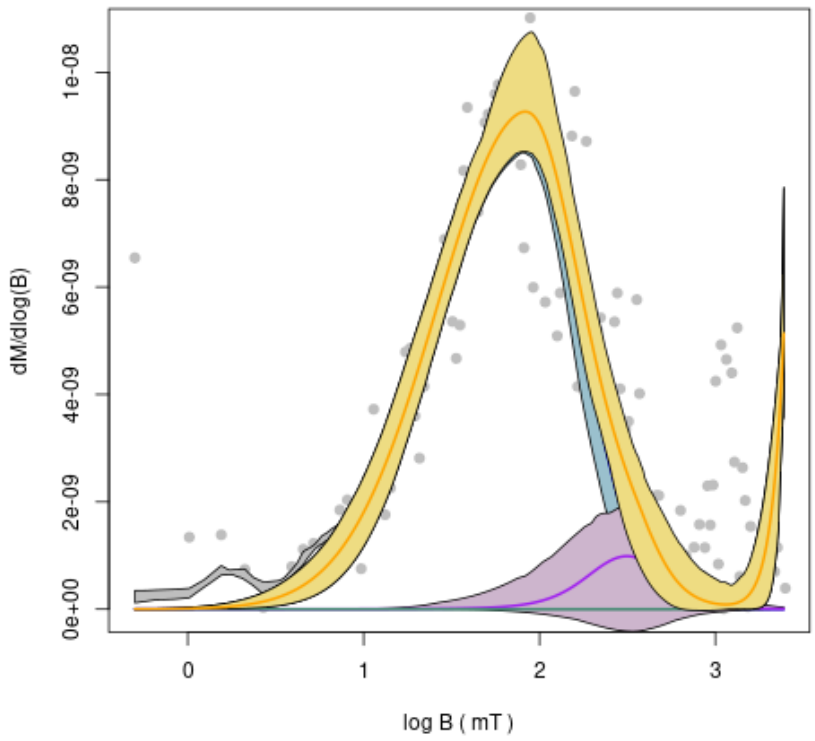

specimen	Ms [Am/kg]	Mr [Am/kg]	Bc [mT]	Bcr [mT]	Xhf [m3/kg]	T [K]
PL20a	-0.00061	2.17E-06	-0.46617	0	8.85E-08	294

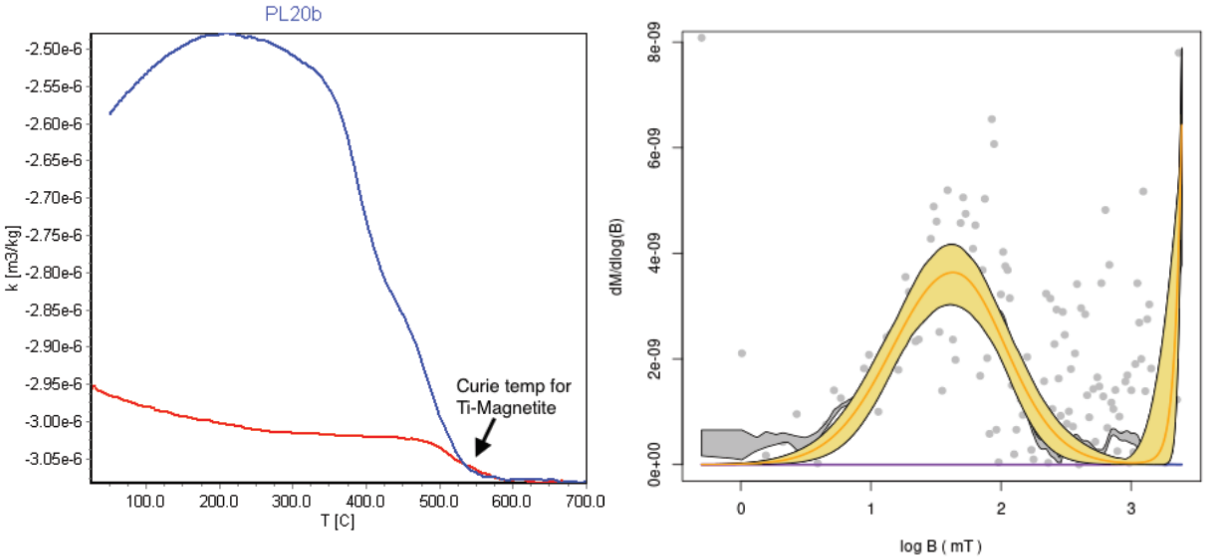

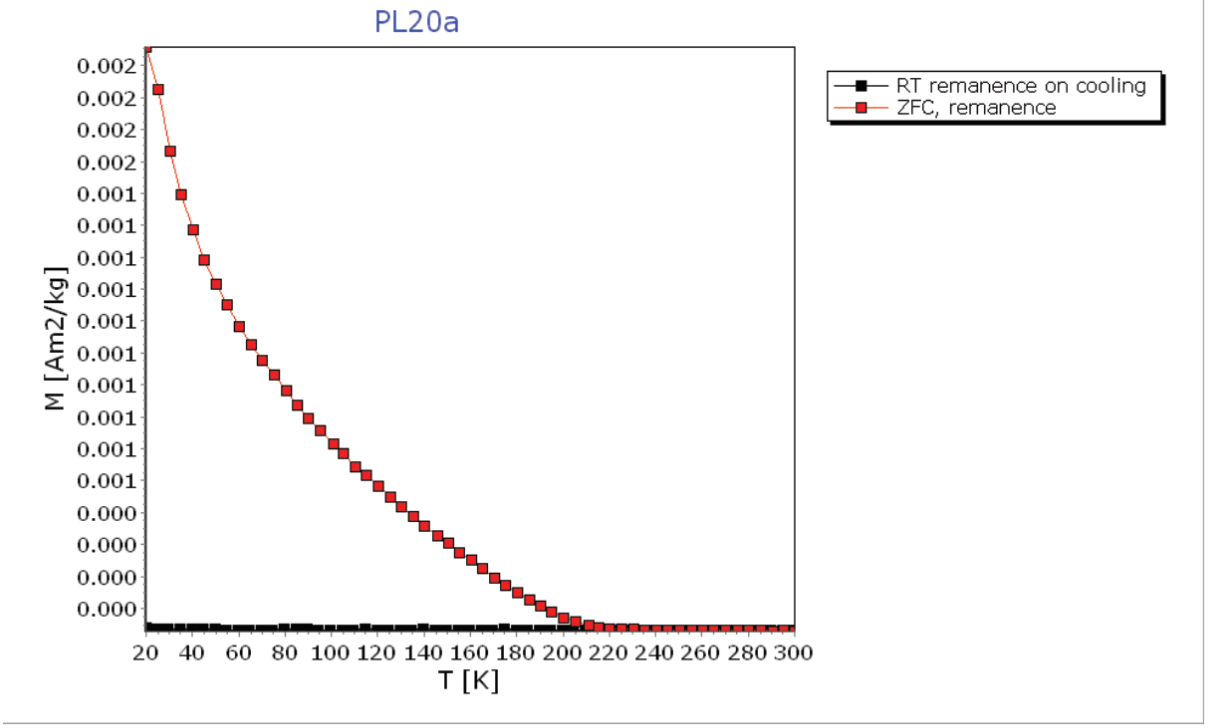

specimen	Ms [Am/kg]	Mr [Am/kg]	Bc [mT]	Bcr [mT]	Xhf [m3/kg]	T [K]
SI13Aa	0.000898	7.04E-05	9.02964	79.9436	9.08E-09	294